AD-A071 502 WEIDLINGER ASSOCIATES MENLO PARK CALIF F/G 19/4
PRETEST SIMULATION OF EVENT S4 HAVE HOST SERIES.(U)
JUL 78 F S WONG, J ISENBERG DNA001-77-C-0104
UNCLASSIFIED R-7841 DNA-4669T NL

1 OF 2
AD
A071502

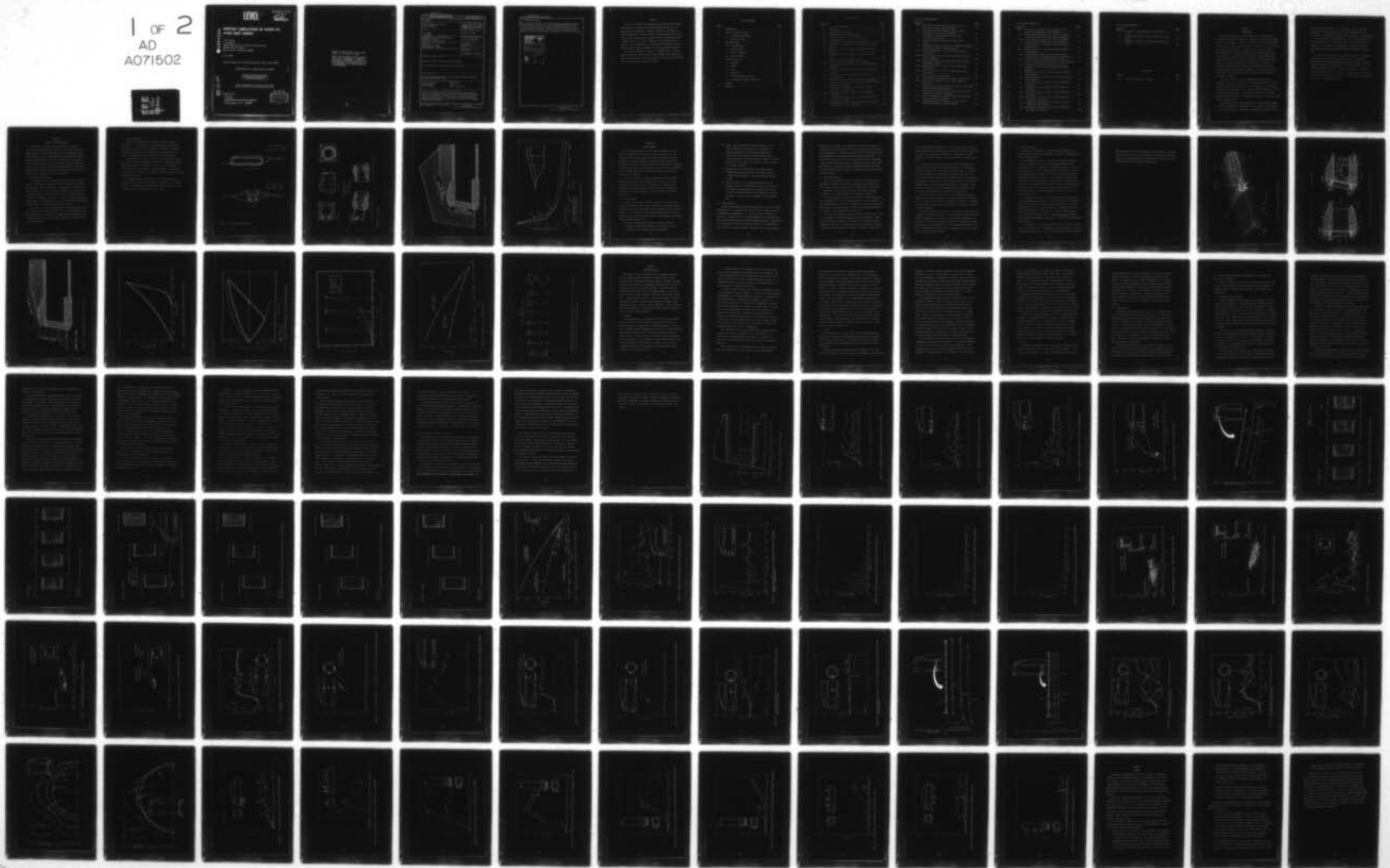

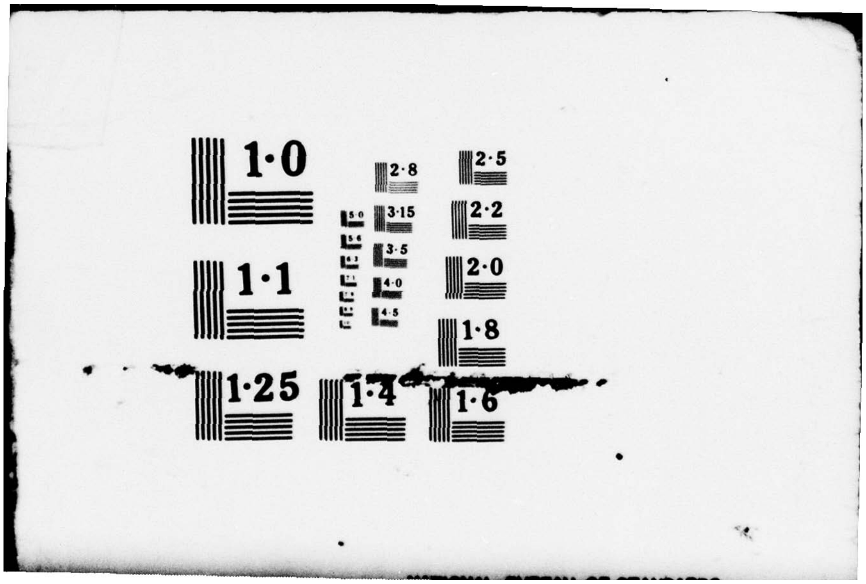
1·0
2·8
2·5
3·15
2·2
3·5
2·0
4·0
1·1
4·5
1·8
1·25
1·4
1·6

LEVEL III

AD-E300 546

12

DNA 4669T

AD A071502

PRETEST SIMULATION OF EVENT S4 HAVE HOST SERIES

F.S. Wong
J. Isenberg
Weidlinger Assoc., Consulting Engineers
3000 Sand Hill Road
Menlo Park, California 94025

July 1978

Topical Report for Period December 1977—July 1978

CONTRACT No. DNA 001-77-C-0104

APPROVED FOR PUBLIC RELEASE;
DISTRIBUTION UNLIMITED.

THIS WORK SPONSORED BY THE DEFENSE NUCLEAR AGENCY
UNDER RDT&E RMSS CODE B344077464 Y99QAXSG65510 H2590D.

Prepared for
Director
DEFENSE NUCLEAR AGENCY
Washington, D. C. 20305

DNA PRINTING PLANT

UNCLASSIFIED

SECURITY CLASSIFICATION OF THIS PAGE (*When Data Entered*)

REPORT DOCUMENTATION PAGE

READ INSTRUCTIONS
BEFORE COMPLETING FORM

1. REPORT NUMBER
DNA 4669T

2. GOVT ACCESSION NO.

3. RECIPIENT'S CATALOG NUMBER

4. TITLE (*and Subtitle*)
PRETEST SIMULATION OF EVENT S4
HAVE HOST SERIES

5. TYPE OF REPORT & PERIOD COVERED
Topical Report for Period
December 1977– July 1978

6. PERFORMING ORG. REPORT NUMBER
R 7841

7. AUTHOR(*s*)
F. S. Wong
J. Isenberg

8. CONTRACT OR GRANT NUMBER(*s*)
DNA 001-77-C-0104

9. PERFORMING ORGANIZATION NAME AND ADDRESS
Weidlinger Assoc., Consulting Engineers
3000 Sand Hill Road
Menlo Park, California 94025

10. PROGRAM ELEMENT, PROJECT, TASK AREA & WORK UNIT NUMBERS
Subtask Y99QAXSG655-10

11. CONTROLLING OFFICE NAME AND ADDRESS
Director
Defense Nuclear Agency
Washington, D.C. 20305

12. REPORT DATE
July 1978

13. NUMBER OF PAGES
98

14. MONITORING AGENCY NAME & ADDRESS(*if different from Controlling Office*)

15. SECURITY CLASS (*of this report*)
UNCLASSIFIED

15a. DECLASSIFICATION DOWNGRADING SCHEDULE

16. DISTRIBUTION STATEMENT (*of this Report*)

Approved for public release; distribution unlimited.

17. DISTRIBUTION STATEMENT (*of the abstract entered in Block 20, if different from Report*)

18. SUPPLEMENTARY NOTES

This work sponsored by the Defense Nuclear Agency under RDT&E RMSS Code B344077464 Y99QAXSG65510 H2590D.

19. KEY WORDS (*Continue on reverse side if necessary and identify by block number*)

Structural Response	HAVE HOST S4
Finite Element	HEST
Airblast Loading	Pretest Simulation

20. ABSTRACT (*Continue on reverse side if necessary and identify by block number*)

This is the third phase of an effort which examines the application of dynamic finite element methods to the analysis of shelter-like structures in a nuclear environment. In Phases 1 and 2, the elastic deformation modes of the shelter structure, their sensitivity to variations in the applied airblast wave forms, and the effects of inelasticity and computer modeling were investigated. (over)

DD FORM 1 JAN 73 1473 EDITION OF 1 NOV 65 IS OBSOLETE

UNCLASSIFIED

SECURITY CLASSIFICATION OF THIS PAGE (*When Data Entered*)

20. ABSTRACT (Continued)

The reported phase (three) consists of applying the methodology developed to a particular case study, i.e., Event S4 of the HAVE HOST test series. Event S4 was the test of a half-scale prototype shelter using the HEST simulated attack environment. The objective of this effort was to provide pre-test analysis and prediction data for Event S4. Detailed pre-test analytical results are provided for the headworks and the shelter main body.

PREFACE

The work reported herein is sponsored by the Defense Nuclear Agency under Contract No. DNA 001-77-C-0104 with Weidlinger Associates. It constitutes the third phase of a study to define the requirements for applying dynamic finite element methods to analyses of MAP shelter structures. In the current phase, the shelter analysis methodology developed in Phases 1 and 2 of the study is applied to a pretest simulation of Event S4 of the HAVE HOST series. The simulation calculation is made to support the test program and SAMSO's closure design validation effort.

The authors would like to thank Mr. T. Kennedy and Dr. C. Ullrich, project monitors for DNA, for their helpful comments and to SAMSO, TRW, AFWL and, in particular, the S4 Test Working Group (S4 TWG) for providing much of the information needed for the study.

TABLE OF CONTENTS

LIST OF FIGURES

LIST OF FIGURES (CONTINUED)

LIST OF FIGURES (CONTINUED)

LIST OF FIGURES (CONTINUED)

LIST OF TABLES

SECTION I

INTRODUCTION

This is the third phase of a study which examines the application of dynamic finite element methods to the analysis of shelter-like structures in a nuclear environment. In Phases 1 and 2, the elastic deformation modes of the shelter structure, their sensitivity to variations in the applied air-blast waveforms and the effect of inelasticity and computer modeling were investigated. An analysis methodology for performing dynamic analysis of the shelter was developed. The procedure involves modeling the shelter-like structure and its medium according to the guidelines established in the study, including those characteristics of the air overpressure which have been found significant and separating the analysis into two distinct but complementary components: the short-term and long-term analyses. These and other results from Phases 1 and 2 have been documented in Reference 1.

The present phase of the study continues the work described in Reference 1, and consists of applying the methodology developed to a particular case study, namely, Event S4 of the HAVE HOST series. In Event S4 a half-scale prototype shelter of the S4 design will be subjected to a HEST simulated attack environment. This simulation calculation is completed prior to the test event, which is scheduled in mid-July 1978 at the time this report is being prepared.

The main objective of the present work is to provide analysis support to the test program and to provide data for the evaluation and validation of the S4 closure design. In addition, by comparing the simulation results and test data, when available, it is possible to obtain a preliminary assessment of the applicability of the analysis methodology proposed in Reference 1. Although the methodology is general in that it is applicable to a class of shelter-like structures under various loading conditions, its evaluation based on a single case study such as the S4 will be restricted. Of all aspects of the methodology, the short-term analysis and headworks modeling considerations can best be measured in this manner.

The remainder of this report is organized as follows: A brief description of the S4 test setup is given in Section II, followed by a description of the simulation model in Section III. Because of the vast amount of simulation results obtained, only selected results pertaining to the response phenomenology are included as Section IV. Additional simulation results which can be used to correlate with test data are documented in a separate report (Reference 11). Major findings and conclusions of the study are summarized in Section V.

SECTION II

EVENT S4, HAVE HOST SERIES

The S4 Event of the HAVE HOST Test Program was conducted at the Air Force Weapons Laboratory (AFWL) test site on the Luke Air Force Range, Arizona. A half-size MAP shelter of the S4 design was tested. Unlike previous tests in the HAVE HOST series which utilized a Dynamic Airblast Simulator (DABS) to provide a simulation of the airblast and reflected effects on the door and berm over the shelter, the S4 Event utilizes the high explosive simulation technique (HEST) to simulate the local airblast acting at the front face, headwalls, and part of the berm. Airblast induced ground motions were not simulated.

2.1. S4 Shelter Configuration

An illustration of the S4 prototype is shown in Figure 2-1 (Reference 3). The shelter is buried with the tube horizontal and the front-face slanting at 10° to the vertical. The details of the headworks are shown in Figure 2-2; it has a basically rectangular cross section, with a rectangular cavity. Only the front-face and a very small portion of the top of the headworks are exposed. The top is covered by overburden and the sides by two wingwalls and fill. The centerline of the rectangular headwork cavity is offset from the centerline of the tube.

The closure is a thick composite slab with concrete encased by steel side and back plates with beveled edges. One of the main purposes of the HAVE HOST S4 Event is to provide test results for the validation of the shelter concept and, in particular, the validation and evaluation of the closure/frame design.

2.2. HEST Configuration

The HEST configuration for Test Event S4 is shown in Figure 2-3 (Reference 4). The two cavities, called the vertical and horizontal HEST cavities, are separated by approximately 18 inches of overburden. The explosive racks will be preassembled in 19 modules, each 2 feet wide. The modules will be oriented vertically on the front-face.

Through these two cavities, pressure will be applied to the entire width of the front-face, wingwalls, and soil berm covering the headworks. Peak face-on pressure is designed to be 4,500 psi, with propagation velocity up the face at 37,000 fps. Peak top pressure is designed to be 1,400 psi, with a velocity of 7,500 fps to simulate the actual airblast wavespeed across the top.

The HEST modules are constructed to yield pressure waveforms to match the design waveforms given in Figure 2-4 (Reference 4). The peak pressure is reached almost instantaneously upon arrival and half of the total load impulse is delivered in the first 8 msec.

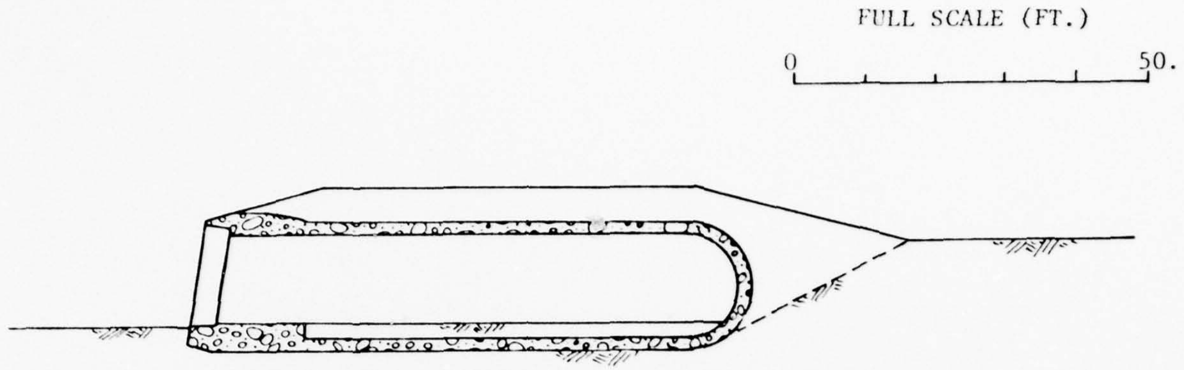

a. Elevation View

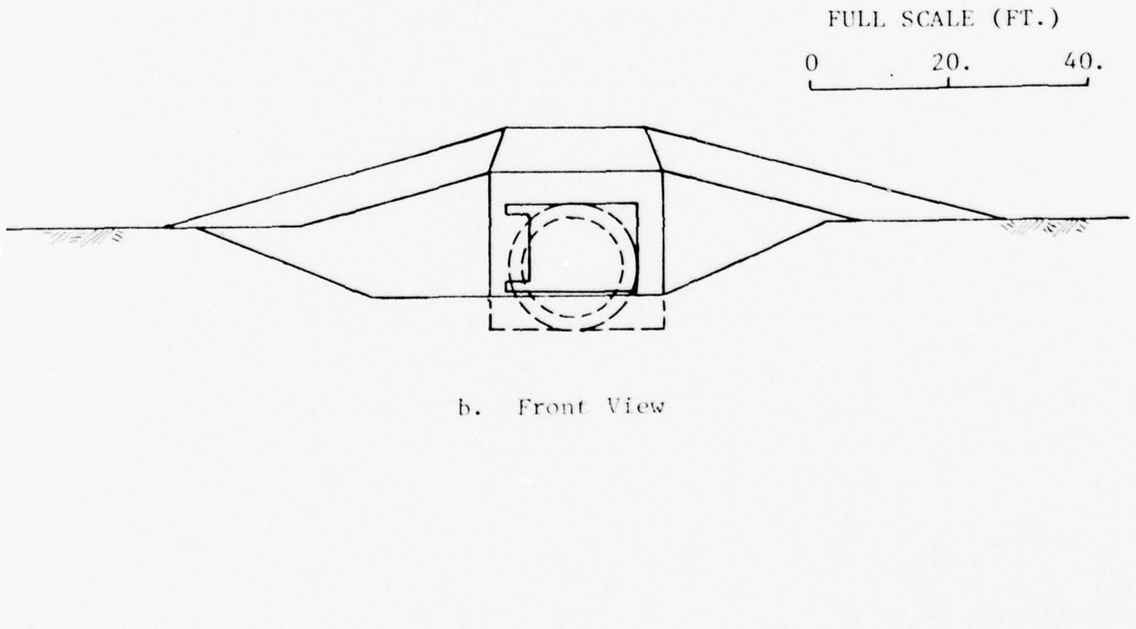

b. Front View

Figure 2-1. S4 Shelter configuration.

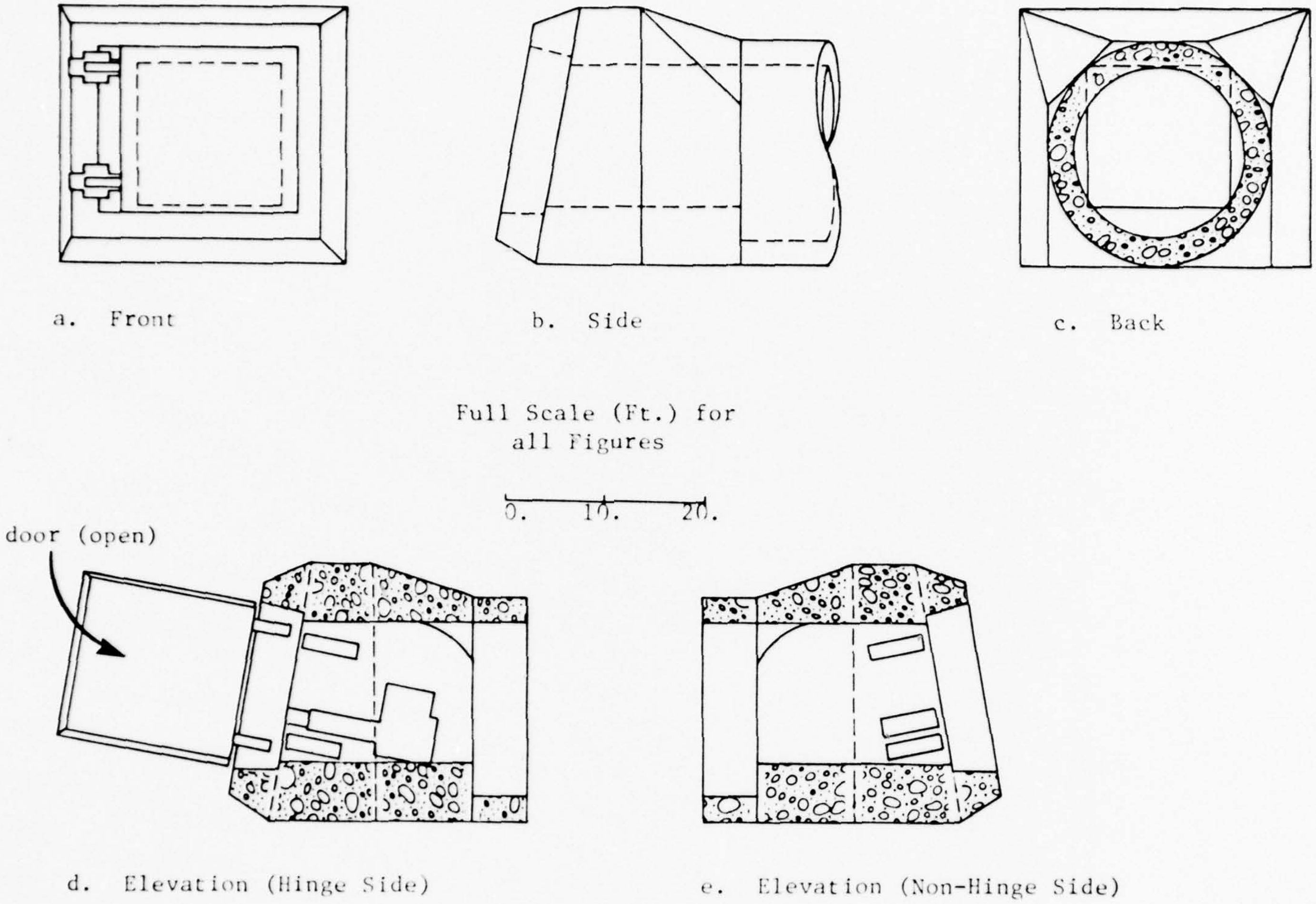
a. Front

b. Side

c. Back

d. Elevation (Hinge Side)

e. Elevation (Non-Hinge Side)

Figure 2-2. S4 Headworks.

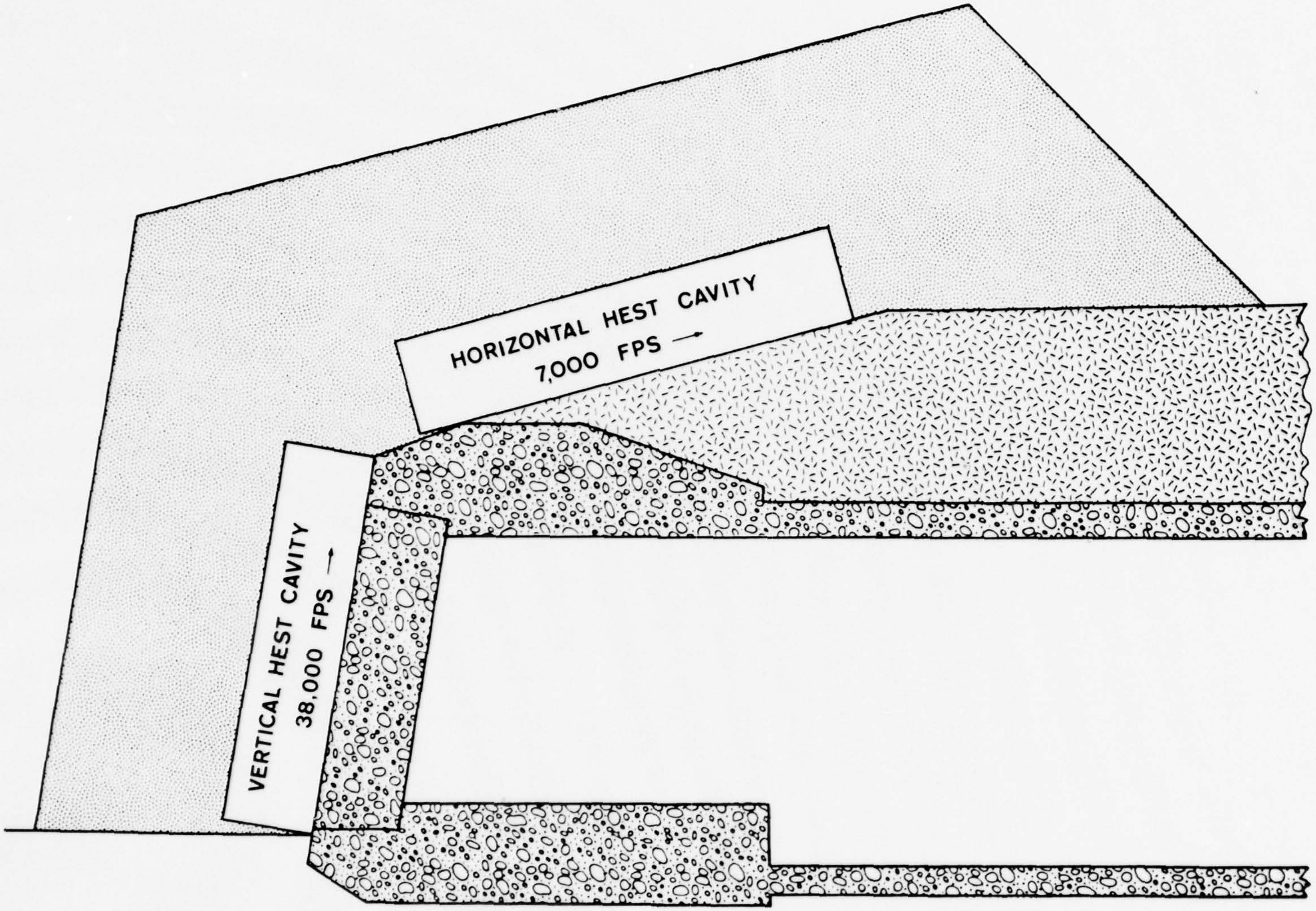

Figure 2-3. HEST Configuration, S4 Test.

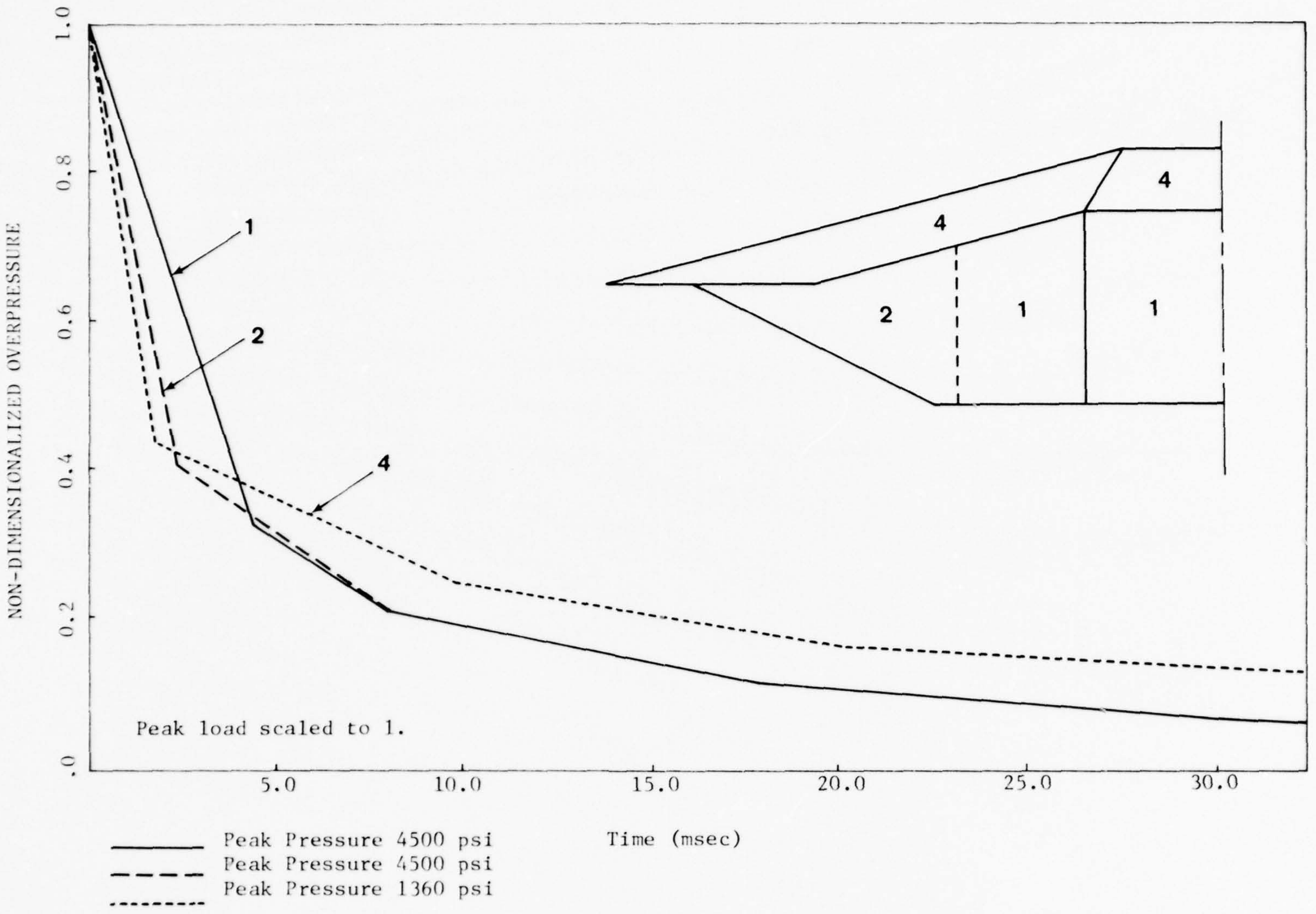

Figure 2-4. HEST Test Design Load Time Histories.

SECTION III

SIMULATION MODEL

The finite element model of the structure and medium used in the simulation analysis of the S4 test is basically the same as that used in the main shelter study (Reference 1); minor modifications have been incorporated to reflect differences between the prototype and the test configuration (absence of the floor slab and fill in the tube, for example). For completeness' sake, a brief description of this model will be repeated herein. An approximate model for the HEST configuration will also be discussed in this section.

One of the key material parameters identified in the main study to have significant effects on the response of the closure is the shear strength of the closure concrete. Consequently, in preparing the S4 simulation model, efforts have been spent in reviewing available data on the closure concrete properties; the resultant model is described in Section 3.3.

3.1. S4 Shelter Model

The model assumes symmetry about the center vertical plane of the tube and includes only the left half or hinge side of the shelter berm configuration. The finite element model of the structure and medium is shown in Figure 3-1. It consists of about 18,000 hexahedrons and, as can be seen from Figure 3-2 which shows the details of the headworks model, special attention has been given to the:

(a) closure - the back and side plates are modeled using two elements across the plate-thickness. The concrete portion is modeled by three elements across the thickness.

(b) frame - the steel lining on the inner frame, as well as the gap between the frame and closure are modeled. To alleviate somewhat the constraint on integration time step imposed by the miniscule gap width, the model incorporates a gap with an artificial width of 5 inches (2.5 inches half scale). This change is not expected to have any effect on the shelter response.

(c) bearing ring - the steel bearing ring is modeled in the refined fashion of the back plate. The closure, however, is assumed rigidly bonded to the bearing ring where contact is made.

(d) transition section - the transition section and the fore portion of the tube are sufficiently refined so as accurately to reproduce stress gradients in this region and the transmission of the bending moment from the headworks to the tube. Two elements are used across the thickness of the cylindrical wall.

3.2. HEST Load Model

The HEST configuration (the vertical and horizontal cavities, the HEST overburden, etc.) is replaced by the main effect it is designed to have on the shelter/berm configuration, i.e., the design loads as described in Section 2.2. Inertial effects of the HEST overburden are not simulated and wave propagation effects within the HEST overburden material are approximated by the application of artificial load-time histories on the shelter/berm surface which is covered by the HEST overburden in the test configuration.

Peak pressure is assumed to vary linearly in the region between the two cavities and in the regions between the cavities and the overburden limits. This approximation is illustrated in Figure 3-3 which shows the peak pressure distribution of the assumed loads on the shelter/berm surface. The times shown are arrival times after first detonation; those corresponding to the two HEST cavities are based on the design detonation speed (37,500 and 7,000 fps, respectively) and those corresponding to HEST overburden and shelter/berm interface are based on a wavespeed of 800 fps in the HEST overburden material.

3.3. Material Properties

The in situ soil material model is identical to that designated as DRY SAND-1 in Weidlinger Associates' ground motion study (Reference 5), with a density of 110 pcf and an uniaxial loading modulus corresponding to a wavespeed of 1,500 fps and an unloading dililational wavespeed of 3,600 fps. Its uniaxial behavior is illustrated in Figure 3-4.

The backfill model is based on data obtained from AFWL (Reference 6) and corresponds to the so-called medium backfill of the data received. The uniaxial behavior of the model is compared in Figure 3-5 with the AFWL data, showing a loading wavespeed of 800 fps and an unloading wavespeed of 3,000 fps. The dry weight density is 120 pcf.

The concrete is modeled as an elastic perfectly plastic material, with an exponential yield surface depending on the mean compression. Except for the closure, the concrete is characterized by unconfined compressive strength of 6,000 psi. The concrete in the closure, however, is assumed to have an unconfined compressive strength of 10,000 psi at 180 days, including dynamic effects (References 7, 8). The yield surfaces for concrete in the closure and in other parts of the shelter are compared in Figure 3-6. Note that at a mean stress of 10,000 psi (J_1 = 30,000 psi), the shear strength of the closure concrete is almost twice that of the shelter concrete.

In the main shelter study (Reference 1), the shear strength of the closure concrete is found to have significant effect on the response of the closure and this effect has been discussed thoroughly. To summarize, the closure behaves like a thick plate in flexure in the elastic range (concrete material with infinite shear strength) and like a slab in punching deformation in the inelastic range (closure concrete with limited shear strength, based on 6,000 psi unconfined strength). Increasing the shear strength by a factor of two in the working range of mean pressures will tend to push the closure behavior towards the elastic extreme.

The structural steel in the closure side and backplates, and in the frame and bearing plate is modeled as an elastic perfectly plastic material with a von Mises yield surface corresponding to A36 steel. No allowance is made for extra strength above the minimum due to statistical variation or dynamic enhancement.

The model parameters for the in situ soil, backfill, concrete and steel are listed in Table 3-1. The format is consistent with the "CAP" model description, although only the in situ soil and backfill are modeled as true CAP materials. In the concrete model for parts of the shelter other than the closure, the tension cutoff point is varied based approximately on the amount of reinforcing steel that exists in different parts of the structure (i.e., headworks, frame, and tube).

3.4. Analysis Program

The simulation calculation is performed using the TRANAL code, a dynamic inelastic 3D finite element program developed by Weidlinger Associates for DNA (Reference 9).

Since TRANAL uses an explicit algorithm to integrate the equations in time, the integration time step used is constrained by the minimum transit time across an element for stability considerations. The subcycling capability of the code enables different time steps to be used for different groups of elements called zones, as long as the stability criterion is observed in each zone. In the simulation calculation, the time step for the zone containing the closure details is necessarily the smallest due to the small size (2.5 inch full scale) of the elements used to model the steel side and backplates and the high wavespeed of steel. The computation time is about 50 CDC7600 CPU seconds for 0.1 msec of real time (full scale).

The simulation calculation is performed using the full scale model for the shelter/berm configuration. This is done mainly for convenience, since a full scale model of S4 was employed in the shelter study. The HEST design loads are scaled appropriately to be compatible with the full scale physical structure. The time axis or impulse is multiplied by 2 to go from half scale to full scale. All simulation results, however, are reported in the half-size or test scale so they can be compared readily with test data.

The computation is performed in installments of 70 cycles or 3.5 msec (test scale time) each. Four installments have been completed so far, and simulation results with up to 14 msec of response time have been obtained.

Some selected results will be presented in the next section. Additional results, mainly in the form of stress/strain invariant and time history plots, are included in Appendix A; they constitute the bulk of the data provided for use in the closure validation effort.

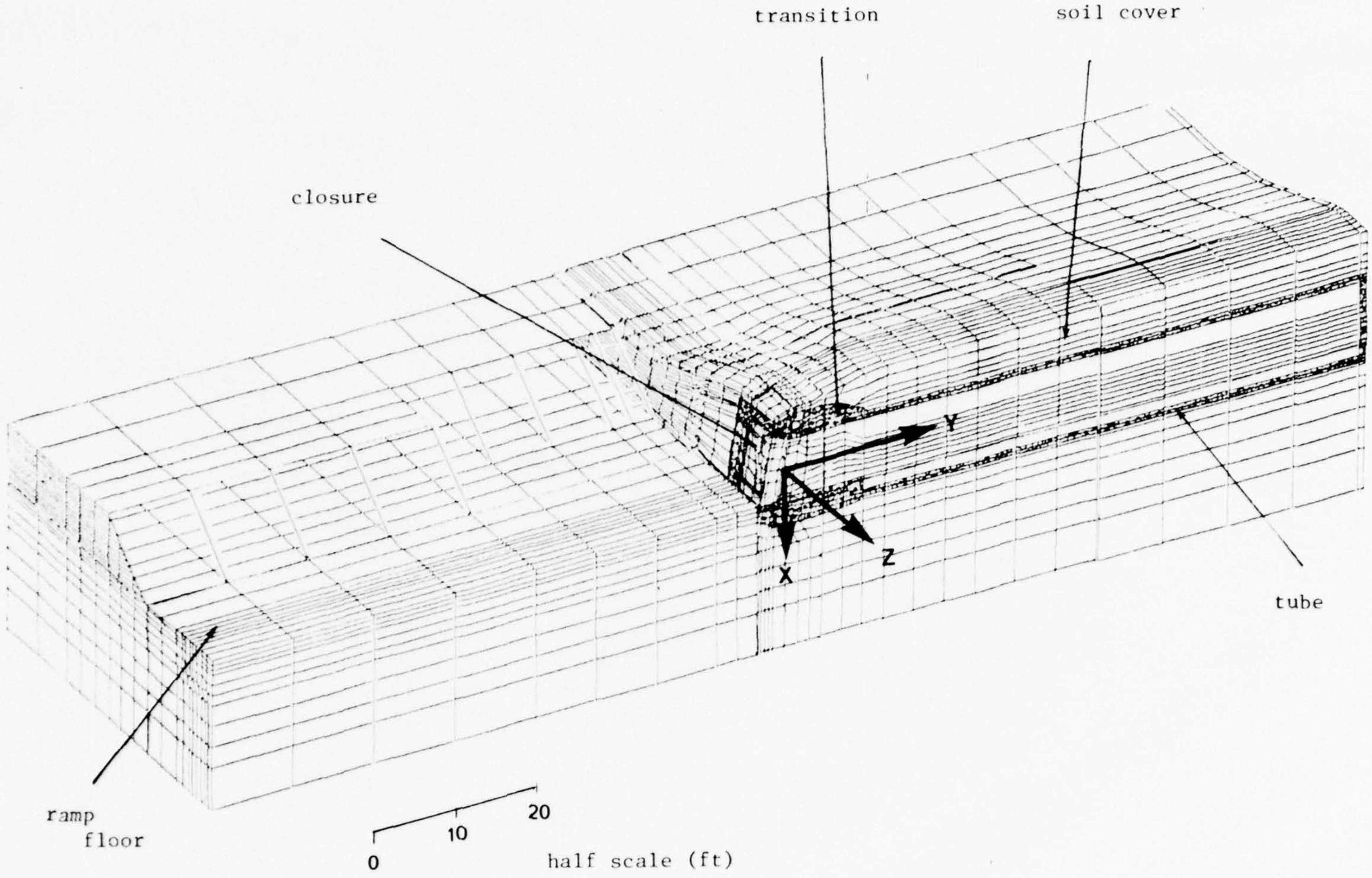

Figure 3-1. FE Model of S4 Test, Coordinate System.

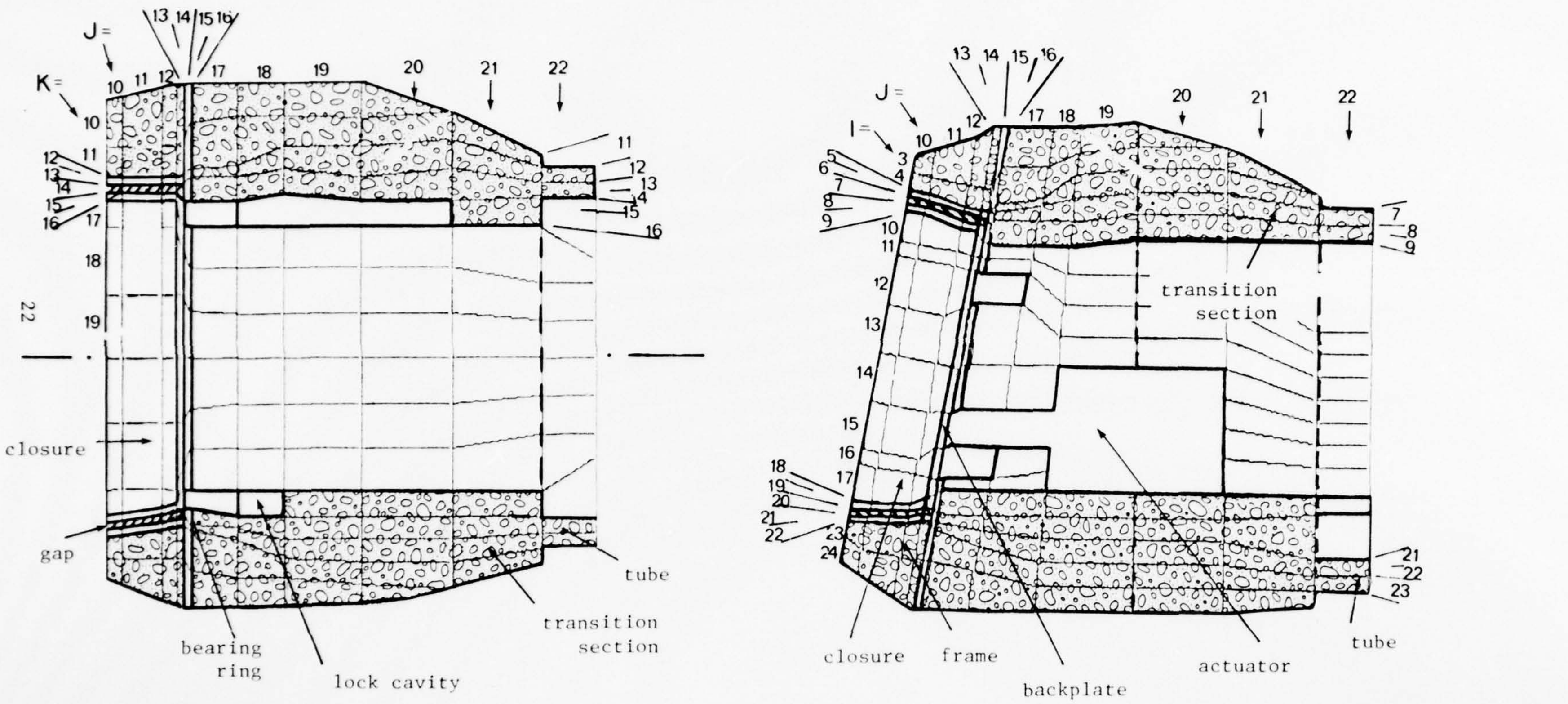
(a) Plan View

(b) Elevation View

Figure 3-2. S4 Headworks Model (IJK are for element/node accounting).

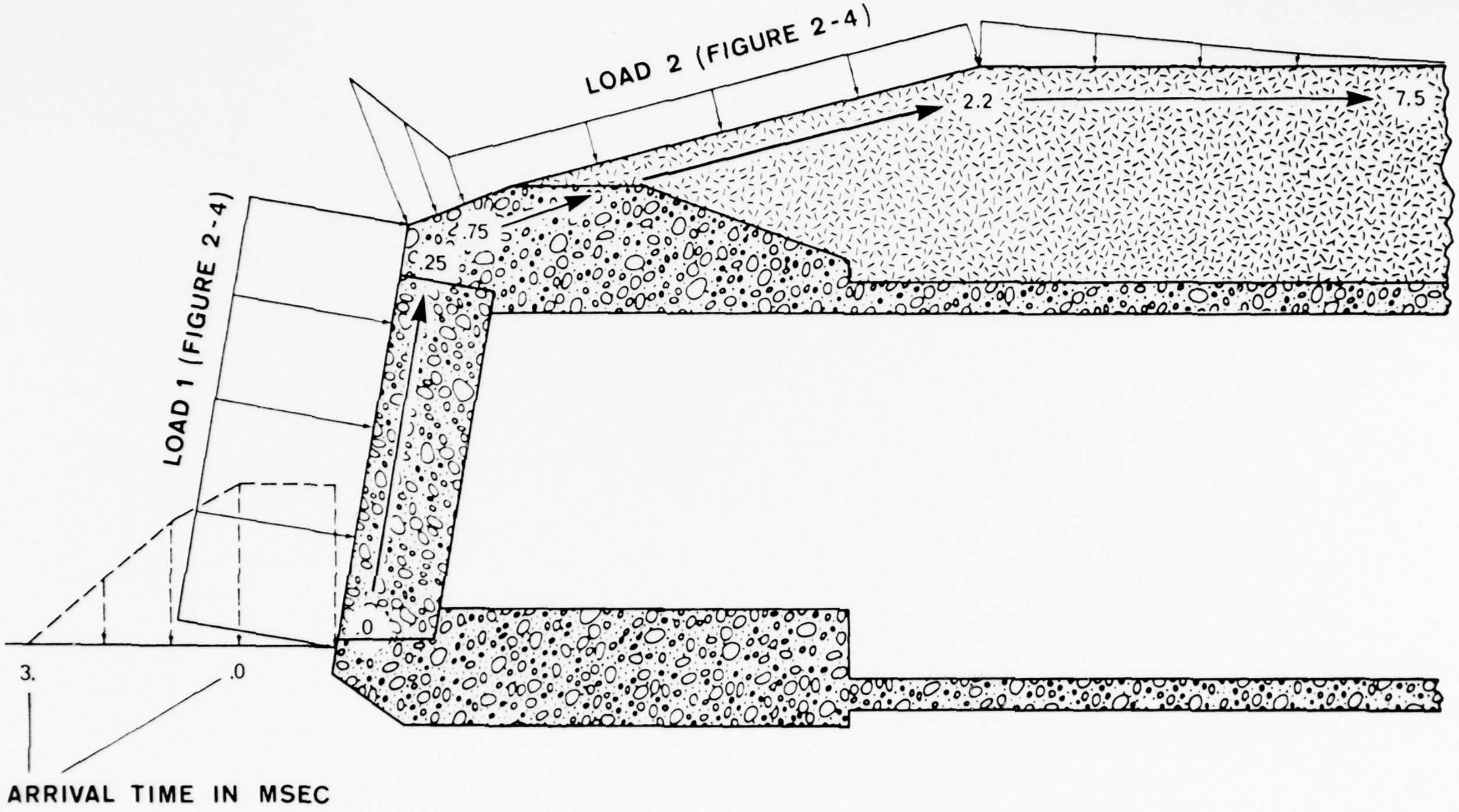

Figure 3-3. Simulated HEST Environment, S4 Test Simulation.

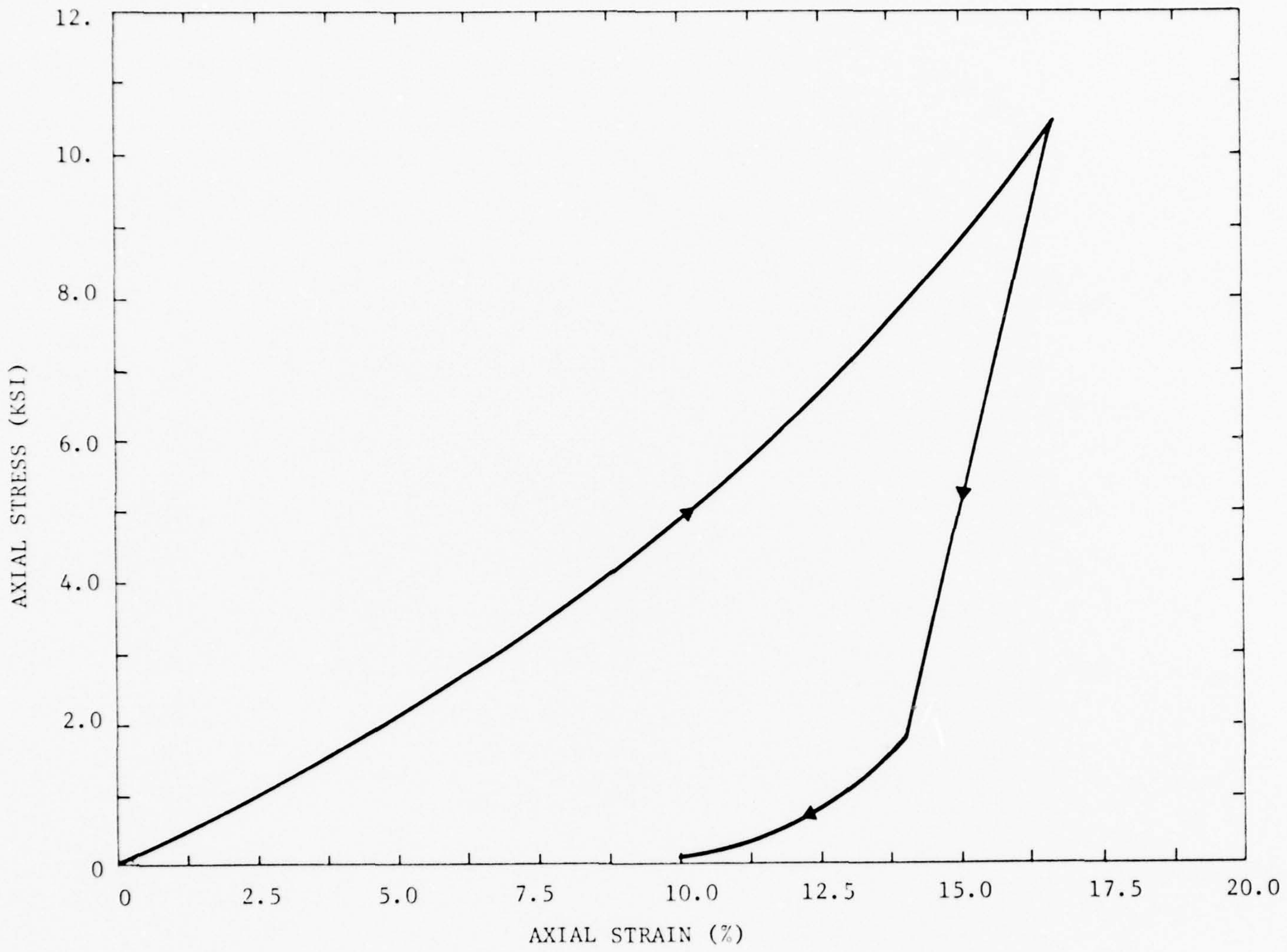

Figure 3-4a. Soil Model in Uniaxial Strain. Axial Stress Versus Axial Strain.

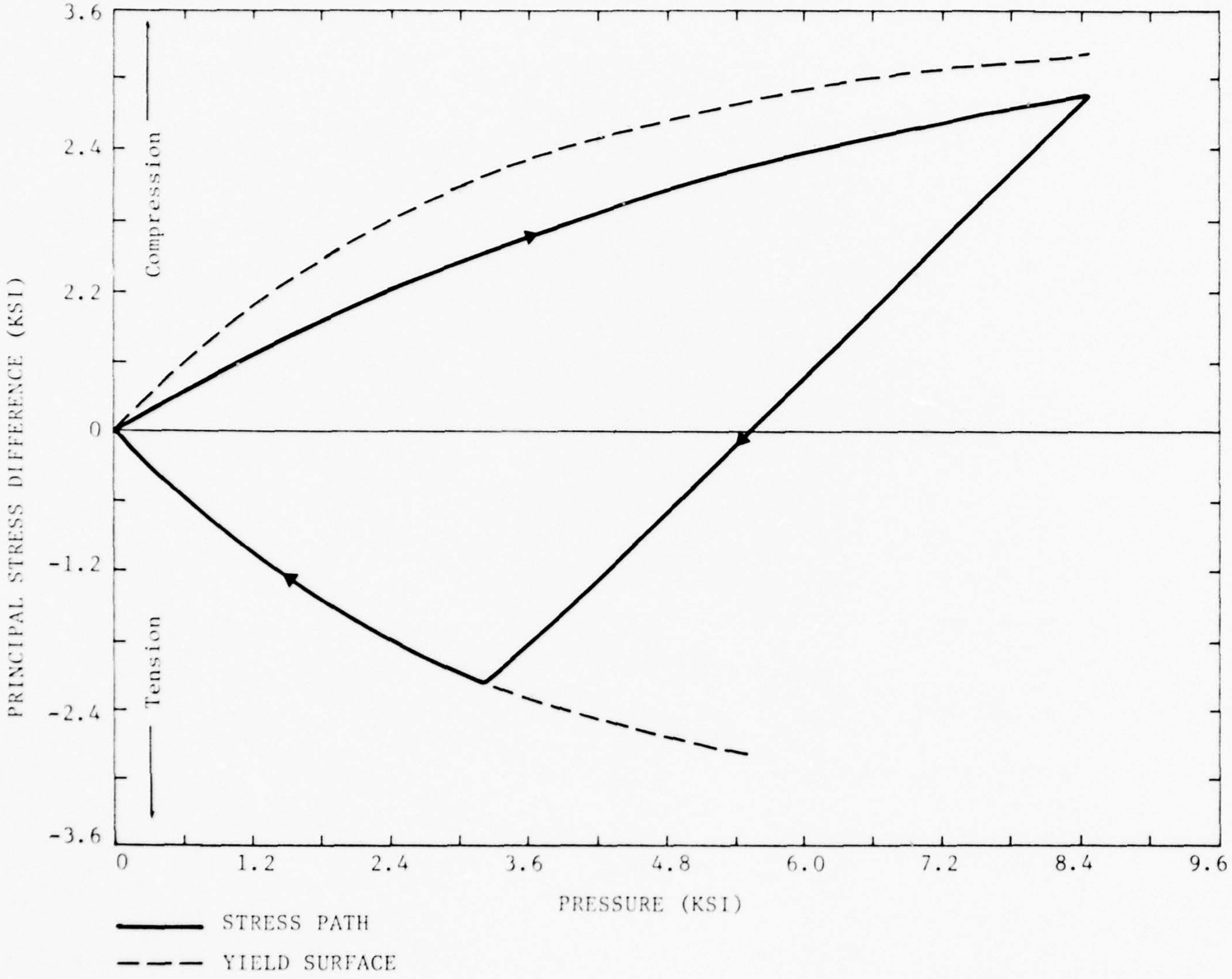

Figure 3-4b. Soil Model in Uniaxial Strain, Stress Difference Versus Pressure.

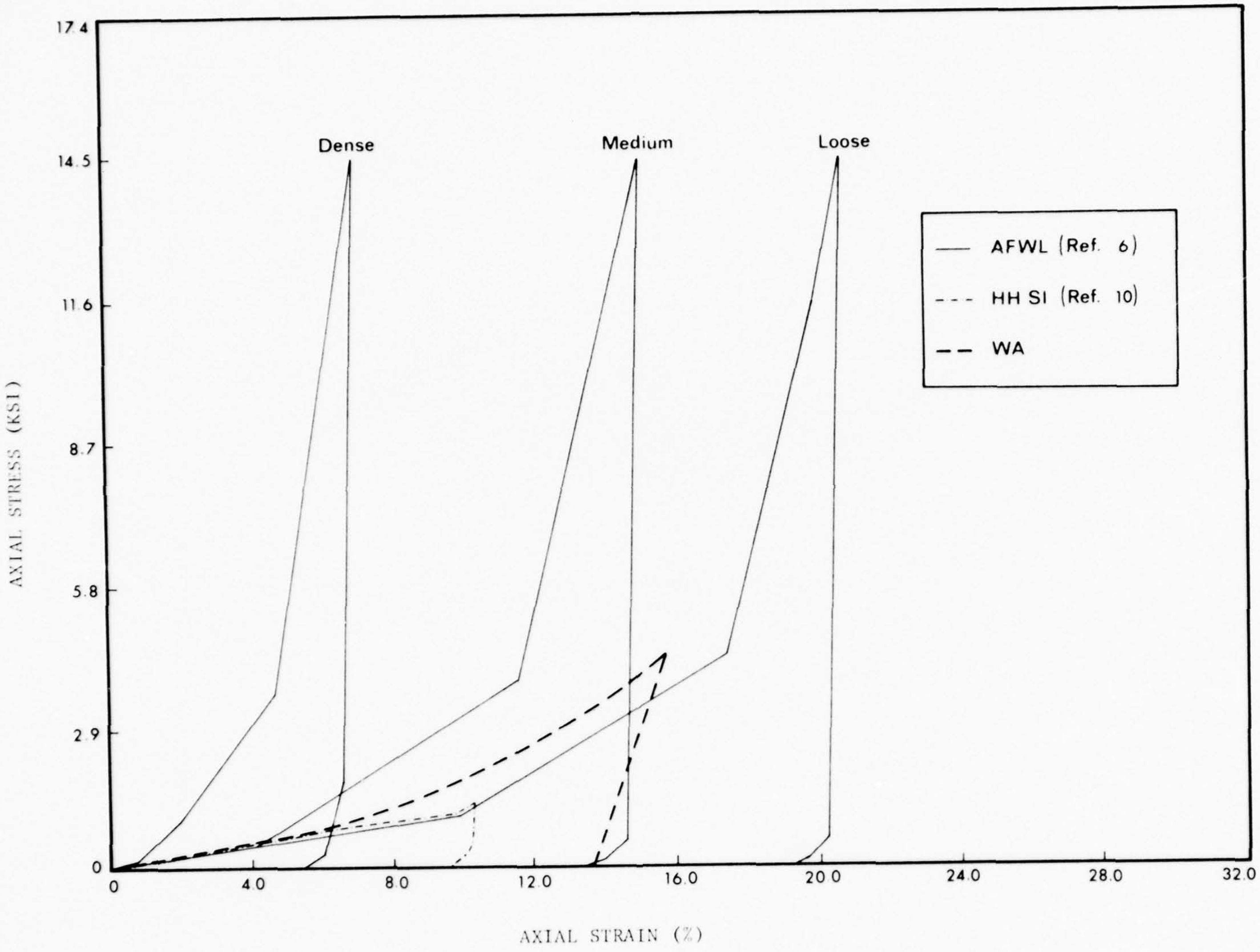

Figure 3-5. Comparison of Backfill Models, Uniaxial Stress/Strain Curves.

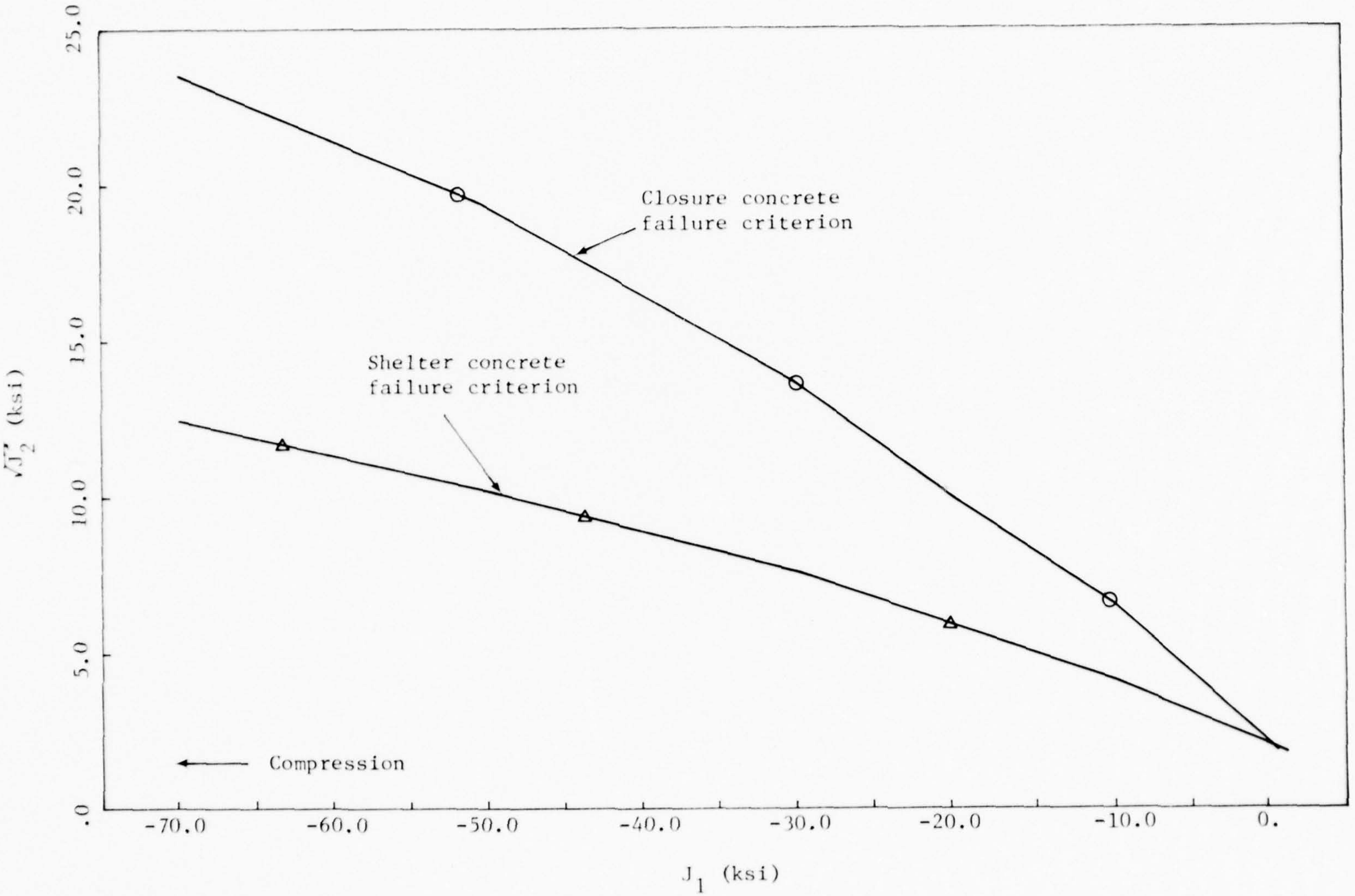

Figure 3-6. Comparison of Concrete Failure Criteria.

TABLE 3-1

MATERIAL PARAMETERS FOR S4 MODEL

				Yield Surface Parameters			CAP Parameters		
Material	Density (pcf)	Bulk Modulus (ksi)	Shear Modulus (ksi)	A (ksi)	B (ksi^{-1})	C (ksi)	D (ksi)	R	W
Concrete*	150.	2333.	1750.	20.	.012	17.8	NO CAP		
Steel**	490.	26850.	11000.	20.8	0.	0.	NO CAP		
Soil	110.	190.	90.	2.1	.1	2.	.06	3.	.15
Backfill	120.	220.	100.	2.1	.13	2.	.18	3.	.15
Closure Concrete	150.	2333.	1750.	40.	.012	37.8	NO CAP		

*Used in conjunction with different tension cutoffs (7.2 ksi to 0.5 ksi) to model various reenforced concrete in the structure, headwall, slab floor and grout.

**For back and side plates in the closure and frame, bearing ring.

SECTION IV

SIMULATION RESULTS

The response of the S4 test structure is, in general, consistent with the results reported in Reference 1 (Calculation 2A) for MAP shelters under front-on nuclear airblast loading. The dominant deformation mode of the structure is longitudinal compression as a result of the loading on the front face (the vertical HEST). In addition, the top loading (horizontal HEST) pushes the headworks downward. Detailed response of the test structure, however, differs from the results of Reference 1. Some differences, such as in the closure response, are due to differences in (closure concrete) material properties assumed. Other differences, such as in the peak response parameters, are due to the different loadings involved. These and other major findings are discussed briefly in the following paragraphs.

4.1. Headworks

The deformed shapes of the headworks cross-section in the assumed plane of symmetry at several response times are shown in Figure 4-1. The displacements are exaggerated for illustration purpose. The headworks is pushed backward and downward by the action of the vertical (front) and horizontal (top) HEST loads. At early times (before 4 msec for example), the top load is not felt by the structure and the deformation mode is mainly that of axial compression. Slight downward motion is due to the 10^{o} incline of the front face. The effect of the top load is established 8 msec into the simulation and the downward motion of the headworks can be clearly identified.

The deformed shapes of the headworks at later times (12 msec and after) strongly suggest that the headworks moves as a rigid-body. This is not surprising since (as will be shown later in this section and in Section 4.2) much of the closure and headworks remains elastic. The displacement profile at 12 msec is typical of the deformed shape of an elastic shelter, as described in Reference 1.

The load acting on the front face induces high longitudinal stresses in the headworks, as shown in Figure 4-2. In spite of these high stresses, the headworks concrete remains essentially elastic due to the effects of confinement exerted by the medium on the headworks. Figure 4-3 is a typical stress invariant plot for points in the headworks and it shows that the headworks response is mostly in the elastic regime. Two exceptions are the region behind the bearing ring and the junction of the transition section and tube. The high load on the bearing area is a reaction to the front load acting on the closure, whereas the high axial stresses in the transition/tube junction is caused by an abrupt change in load bearing, cross-sectional area of the structure. They will be discussed in Sections 4.4 and 4.5, respectively.

The longitudinal stress in the headworks has a main pulse duration of about 6 msec, which is comparable to that of the HEST load. At points near the transition/tube junction (point D in Figure 4-2), the pulse width is much longer and the reason for this will be discussed in Section 4.5.

Since the HEST loads are concentrated in the vicinity of the headworks, the downward motion of the structure is most prominent there.

The tube portion of the structure experiences very little downward motion and only as a reaction to the downward motion of the headworks. This is in contrast to the response of the shelter structure in a nuclear attack environment. The airblast loading acting on the berm induces downward ground (and hence structure) motions along the length of the tube. There is, of course, a time delay involved in this action due to the necessary transmission time through the berm material. Hence, at early times, the response of the structure in a nuclear environment can be reproduced by that of the test structure. The simulated and nuclear responses at later times of the structure as a whole and the tube section in particular may be different due to the absence of ground shock load on top of the tube in the HEST test configuration; the extent of the difference depends on the backfill stiffness (wavespeed) and, of course, the intensity of the load involved. For the S4 test, the ground shock will reach the crown of the fore portion of the tube at about 8 msec and the invert at 18 msec. The HEST simulation response is, therefore, valid for at least the first 8 msec, or 16 msec full-scale time.

4.2. Closure

The closure deforms as a thick elastic slab, with maximum midspan deflection of the order of an inch when measured relative to the support. This is evident from Figure 4-4. The support motion, in turn, follows the rigid body pattern of the headworks motion as indicated in Figure 4-1 of Section 4.1.

Although the overall deformation mode of the closure is that of an elastic slab, portions of the closure, notably the backplate and the concrete adjacent to it, undergo inelastic deformation. This can be illustrated in Figures 4-5 and 4-6. The development of inelastic zones in the closure (steel) backplate is illustrated in Figure 4-5. Note that the backplate material yields first at midspan, due to the high tensile stresses developed in bending, followed by yielding at the edges. Note also that the inelastic activity starts at 1.8 msec or 0.8 msec after the HEST load has attained its peak value (an artificial rise time of 1 msec is assumed in the analysis) and is over 2 msec thereafter.

The development of inelastic zones in the closure concrete is illustrated in Figure 4-6. Since the concrete portion of the closure is modeled by three elements across its thickness, three profiles are shown for each response time of interest corresponding, respectively, to the front, mid and rear layers of elements in the model. The rear layer is adjacent to the backplate. Note that inelastic deformation in the closure concrete is initiated at about 1.5 msec or 0.5 msec after the load has attained its peak magnitude, and that the initiation of inelastic deformation in the concrete precedes that in the backplate. Concrete at midspan fails in tension as a result of flexure; concrete near the support fails in shear, due to the high shear stresses in the slab and the equally high reaction forces at the bearing plate.

Note that inelastic deformation occurs only in concrete adjacent to the backplate (the rear layer in the model). This finding is confirmed in Figure 4-7, which shows the concrete failure criterion in stress invariant spaces ($\sqrt{J_2'}$, J_1). Each data point plotted in the figure corresponds to the maximum response of an element in the closure concrete model. From this figure, it is apparent that inelastic deformation is limited to the rear concrete elements. When closure concrete with a lower shear strength is used, as represented by the dotted line in Figure 4-7, it is expected that inelastic deformation will spread to other regions of the closure concrete. This is indeed the case and, as reported in Calculation 2A, Reference 1, the closure deformation mode in that case is drastically different from that described herein.

The absolute velocity/time histories of the closure cg are given in Figure 4-8. The initial peaks of about 500 ips in the longitudinal direction and 180 ips in the vertical direction are mainly the response of the closure to the HEST load, because at this early time the headworks is effectively stationary. The portion of the time histories after 3 msec contains contribution from the motion of the headworks (closure support).

The closure cg velocity measured relative to the support motion and resolved into a component normal to the backplate is given in Figure 4-9. A Fourier decomposition of this motion (Figure 4-10) shows a dominant period at 140 Hz. The support or headworks motion,on the other hand, has a dominant period of 80 Hz in both the longitudinal and vertical directions, as Figure 4-11 shows. Dominant components at yet lower frequencies may exist, but because of the short duration of the calculated response (14 msec) they cannot be accurately identified.

4.3. Frame

Minor inelastic deformation occurs in the frame, notably in the top, bottom and side center gussets, and at the inside frame corners. Yielding occurs at the corners of the steel "ring" lining the inner surface of the frame (adjacent to the gap opening) due to the action of the gap pressure which tends to push the frame outward and "round" the frame corners. Two elements are used to model the lining across its thickness. The inner steel element (adjacent to gap) sustains high tension, whereas the outer element (adjacent to frame concrete) sustains high compression (see Figure 4-12). Concrete in the vicinity of the corners is similarly affected, although to a lesser extent. Inelastic deformation in the frame, however, is local in that it has no significant effect on other parts of the shelter so long as the integrity of the frame is not compromised.

4.4. Bearing Ring

The bearing ring supports the closure and is also an integral part of the steel plate which forms the base of the frame. The bearing load time histories at selected points in the bearing ring are given in Figure 4-13. The bearing load is higher at the bottom edge than at the top or side, a finding which is consistent with the previous analysis, Reference 1. Note that the effective load duration is about 3 or 4 msec, during which time the closure is pressed against the bearing ring due to the action of the HEST load. The headworks is relatively stationary during this time. Thereafter, the closure and headworks move practically in unison and the bearing load is diminished.

The average peak bearing stress of 25,000 psi is about half of the static value of 54,000 psi calculated based on the load/support area ratio. Furthermore, the peak bearing load decreases rapidly with increasing distance away from the closure/bearing ring interface. The bearing load in the concrete immediately behind the bearing ring, for instance, has a peak of only 14,000 psi.

Inelastic deformation occurs in the steel bearing ring (Figure 4-14) and the concrete immediately behind it (Figure 4-15); the extent of the yielding, however, is slight and will not impair the function of the bearing ring.

4.5. Transition Section and Tube

The high longitudinal stresses induced in the headworks by the front load become even higher in the transition and tube regions because the load bearing cross-sectional area of the structure decreases. The ratio of the headworks cross-sectional area to that of the tube, for instance, is approximately 5. Hence, if the strength of the tube concrete is sufficiently high, a peak longitudinal stress of about 25,000 psi can be induced in the tube. With a limited shear strength, the maximum axial load which the tube can sustain depends on the confining pressure exerted by the soil on the tube.

From Figure 4-16, the average longitudinal compression in the tube section a half-tube diameter behind the headworks has a peak of 8,000 psi at the crown, and 10,000 psi at the invert. Alternately, the same response can be viewed in the stress invariant spaces (Figure 4-17) and it is noted that the peak longitudinal compression is indeed limited by the shear strength of the concrete model.

The fact that the longitudinal stress is higher at the invert than at the crown is significant in that it deviates from the general trend established in Reference 1 (Calculations 1B through 1D, Calculations 2A through 2C), although the maximum longitudinal stress differential is only about 2,000 psi. With the floor slab and fill removed from the tube, the change in load bearing cross-sectional area in the test structure is more abrupt at the invert of the transition/tube junction, (see Figure 2-2 of Section II) than at the crown. This may account for the higher longitudinal stress at the invert. The HEST configuration with the applied load restricted to the front face and top of the headworks may also contribute to the response described herein. This effect will be discussed in a subsequent paragraph of this section.

The duration of significant longitudinal stress in the tube appears to be longer than 14 msec, the duration of calculated response. The major cause of the long duration is due to yielding in the tube. The longitudinal load bearing strength of the tube is limited because of the limited shear strength of the concrete and the limited resistance provided by the tube is not large enough to arrest the momentum of the headworks in a short time. It can only slow down the motion of the headworks and has only moderate success in doing so. Referring to Figure 4-18, the mean headworks velocity in the longitudinal direction reaches its maximum at 5 msec and decelerates moderately thereafter. Meanwhile, the momentum of the headworks continues to carry it into the tube, which remains compressed even though the applied front load is effectively over in 7 msec.

From the stress invariant plot of Figure 4-17, it is also determined that at about the termination of the simulation calculation, the state of stress in the fore tube concrete is back into the elastic regime, signaling the end of inelastic deformation (but not longitudinal compression) at that location.

This interaction between the headworks and tube can be illustrated by the response of a lumped-parameter model of the structure, in which the headworks is approximated by a mass connected to an elasto-plastic spring which represents the tube. The external load is then applied to the mass directly and the system parameters can be adjusted so as to reproduce the overall headworks/tube interaction described herein.

The longitudinal compression in a tube section at about two-tube diameters behind the headworks is shown in Figure 4-19. Since the compression is practically uniform throughout the cross-section, only the results for points at the crown are shown. The magnitude is about 6,000 psi, which is attained upon wavefront arrival and is maintained thereafter. Figure 4-20 is typical of the stress invariant plots obtained for points in that section.

Comparing the stress invariant plots for the two tube cross-sections (Figures 4-17 and 4-20) brings out an interesting observation. Although concretes at both locations deform inelastically upon initial loading, their responses differ thereafter. For the tube section near the headworks (Figure 4-17), there is significant confinement pressure acting on the lateral surface of the tube so that higher mean pressures (and hence higher shear strengths) and higher axial loads can be sustained by the concrete. The lateral confinement may come from the engulfment by airblast-induced ground shock, the front load transmitted to the medium and to a lesser extent the restraint imposed by the massive headworks on the tube.

None of these effects is apparently present at the tube section, two-tube diameters behind the headworks, and consequently, the maximum average axial stress that can be sustained is only 6,000 psi, which is the unconfined strength of the tube concrete. It is not known to what extent this (lack of confinement) condition is present in a nuclear environment where air overpressure loads act along the length of the berm and tube. The resultant soil confinement arrising from the top load (about 400 psi for the baseline nuclear threat) depends on the properties of the medium and the height of the berm overburden.

The strain/time histories for a point at the springline the tube section half-tube diameter behind the headworks are shown in Figure 4-21, and are typical of the results obtained for concrete in the fore portion of the tube. The large longitudinal strain (of the order of 1.5%) is due to the longitudinal compression. The large circumferential and radial strains are a result of inelastic deformation and the dilatancy of the concrete model assumed; the flow rule associated with the concrete yield surface (see Figure 3-6 of Section 3.3) dictates volumetric expansion during inelastic deformation.

Shear strains are in general smaller than the normal strains and are larger at the springline (0.5%) than at either the crown or invert, where they are almost negligible.

Note that all strain/time histories are close to their maxima at the end of response time, and because of the predominant inelastic deformation involved, their values at 14 msec can be construed as the accumulated inelastic strains.

Strains for a tube section farther away from the headworks exhibit similar behavior. Their peak magnitude decreases with increasing distance from the headworks. For a section two-tube diameters behind the headworks, for instance, the peak normal strain is about 0.3% in/in and the shear strains are negligible.

In Figure 4-22, the displacements of a plane tube cross-section are illustrated. The section in question is about one-tube diameter behind the headworks, and initially, the side or elevation view of this section appears as a straight vertical line. When loaded, the higher longitudinal stress at the invert is manifested as a larger longitudinal displacement at that location than, say, at the crown. If straight lines are drawn through the data points to represent gross motion of the tube section had it remained plane, these lines will rotate in the clockwise direction signifying bending of the tube in that direction. In the actual deformed states, as shown in Figure 4-22, most of the non-plane deformation occurs in the invert region.

Note that at early times, the crown of the section is actually displaced upward, as a result of the longitudinal compression and dilatancy of concrete. In fact, the tube section expands radially outward as the tube is compressed in the longitudinal direction.

The deformed profiles of a tube section about two-tube diameters behind the headworks is given in Figure 4-23. The deformation is quite uniform throughout the section, consistent with the uniform distribution of longitudinal stress observed in Figure 4-19. The displacement is less than that for a section closer to the headworks (see Figure 4-22), also consistent with the lower longitudinal stress recorded at that location (see Figure 4-19). There is also less expansion of the section in the radial direction.

Circumferential/time histories for points in a tube section half-tube diameter behind the headworks are shown in Figure 4-24. The mean hoop compression is initially higher at the invert than at the crown or springline. This is a reaction to the longitudinal compression since, as noted in Figure 4-16, higher longitudinal stress is induced at the invert than at the crown or springline. Comparing the circumferential stresses at the inner and outer fibres at the crown of the tube section (Figure 4-24a) indicates that the ring segment at that location undergoes initially negative (convex) bending and later positive (concave) bending in the plane of the section. Applying the same reasoning to the invert and springline (Figures 4-24b,c), the ring segments at the invert and springline are found to sustain inplane convex bending only.

The inplane deformation can also be illustrated by Figure 4-25, in which are plotted the deformed shapes of the tube cross-section in question. At early times (before 10 msec), the inplane deformation is mainly radial as the tube expands outward when compressed longitudinally. The inplane bending patterns at the crown, invert and springline described in the preceding paragraph are also apparent. They consitute the n = 4 deformation mode of a ring, and this deformation mode of relatively high order is probably induced by the structural constraints imposed by the bulky headworks on the tube. After 10 msec, the downward motion of the headworks (and top HEST load) is established and its effect is to pull the tube downward also.

The inplane deformation mode is now dominated by the ovalling or n = 2 mode except near the invert where the stiff in situ soil in contact with the structure constrains it from following the ovalling pattern.

The inplane deformation pattern for a tube section farther down the tube (two-tube diameters behind the headworks) is illustrated in Figure 4-26. Because of the large distance away from the headworks, the effect of the structural constraint of the headworks on the early time deformation mode is not as prominent as that shown in Figure 4-25. The late time deformation pattern is similar, however, to that of a section near the headworks, although the magnitude of deformation is proportionally less. (Note that the displacement scale in Figure 4-25 is about twice that of Figure 4-26.)

4.6. Soil/Structure Interface Stresses

The distribution of soil pressure on the bottom side of the headworks is illustrated in Figure 4-27; the peak value ranges from 400 to 600 psi. The term pressure is used in this section to denote the stress component normal to the soil/structure interface. Note that the initial peak for the soil pressure at point A at 3.5 msec is due to the HEST induced ground shock, whereas the later peak at 10 msec is probably due to the downward movement of the headworks. Soil resistance to structural motion increases with distance from the front (from A to D).

Soil pressures acting on top of the headworks are given in Figure 4-28. Since they originate from the top HEST load, the magnitude and the characteristics of the soil pressure at a particular point on top of the headworks depend significantly on the thickness of the berm above that location. For a point under a shallow layer of backfill, such as point A of Figure 4-28, the induced soil pressure is high and the pulse characteristics are similar to the HEST load (spurious behavior after the initial peak is due partly to reflections at the soi/structure interface and the berm face surface, and partly to numerical integration). At point B of Figure 4-28, the effect on the pulse shape of traveling through five feet of soil is conspicuous; the peak soil stress decreases to 1100 psi and the pulse shape is significantly modified. These simulation results include some "numerical filtering" due to the finite dimension of the elements used. However, they provide a good measure of the load (impulse) responsible for the downward motion of the headworks, since that motion has a basic frequency (80 Hz from Figure 4-11) well within the capability of the model.

Soil pressures acting on the sides of the headworks are illustrated in Figures 4-29a through 4-29d, at various distances from the point and at two different depths. Peak pressure is about 2,000 psi, and is due mainly to stress waves induced in the medium by the front HEST load. The peak pressure decreases with distance from the front face and is only 800 psi at the transition/tube junction. The pulse shape, however, remains relatively unchanged with distance.

Soil pressures acting on the tube at early times (before 14 msec) are passive pressures, i.e., they are exclusively due to the actions of the front-loaded structure against the soil. Their distribution along the tube is illustrated in Figure 4-30 for points at the crown, in Figure 4-31 for points at the invert and in Figure 4-32 for points at the springline. The passive pressure is higher at the front portion of the tube and becomes negligible at about two-tube diameters behind the headworks and thereafter. This lack of confinement at mid-span confirmed, the explanation given in Section 4.5 for the low longitudinal load sustained by the tube at that location.

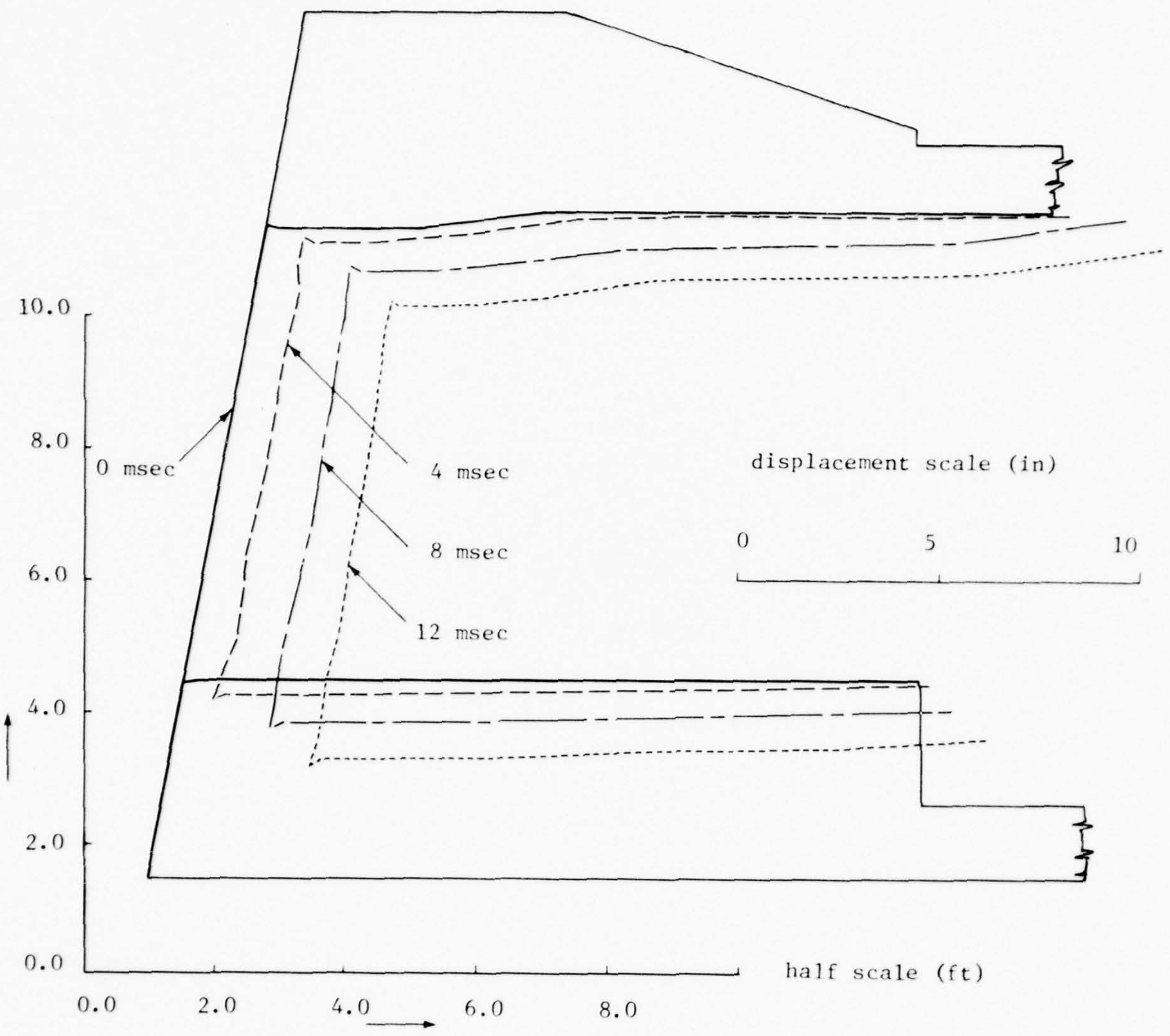

Figure 4-1. Deformation Mode of Headworks, Plane of Symmetry.

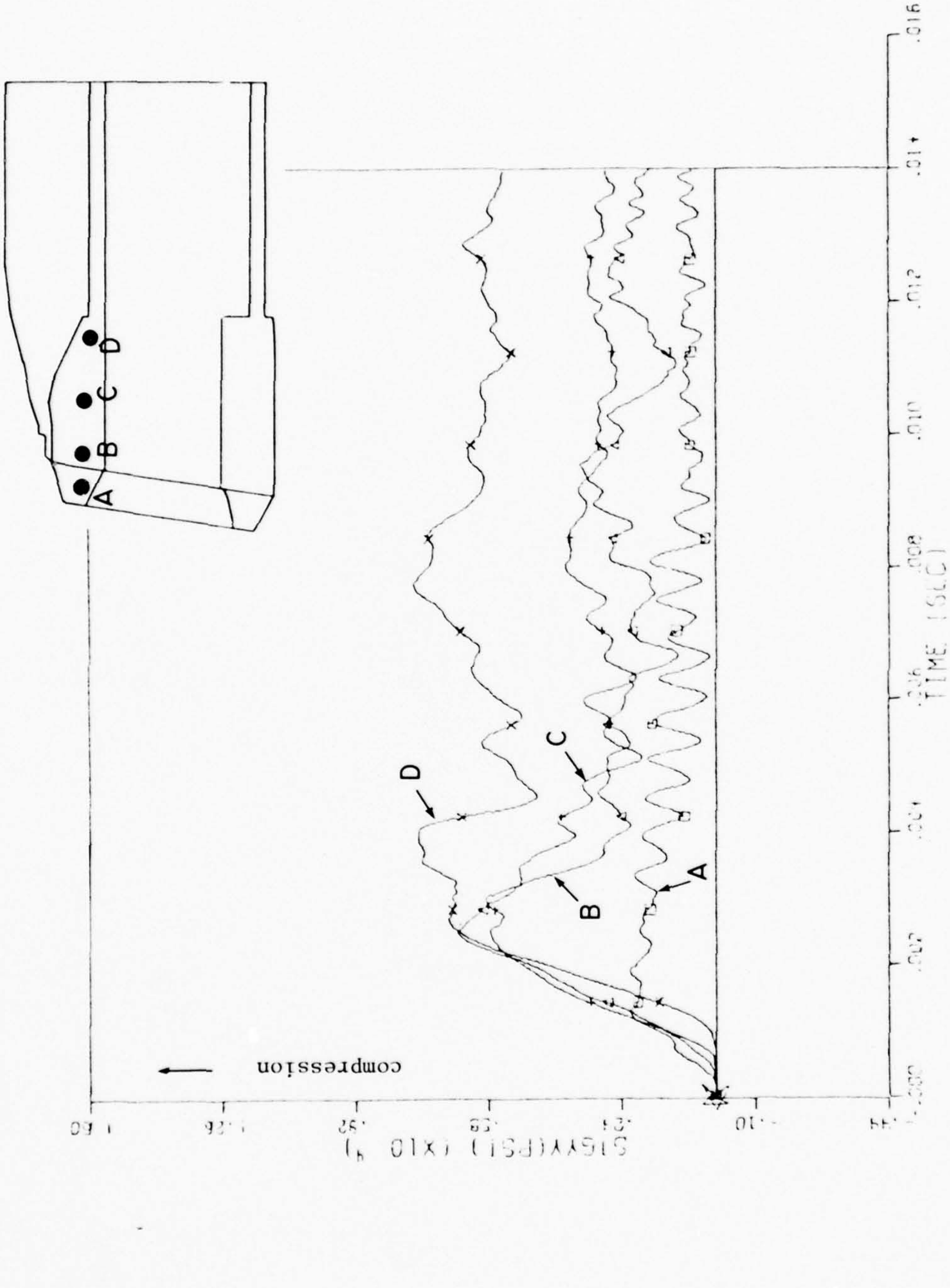

Figure 4-2a. Longitudinal Stress/Time Histories for Points Along Upper Headworks.

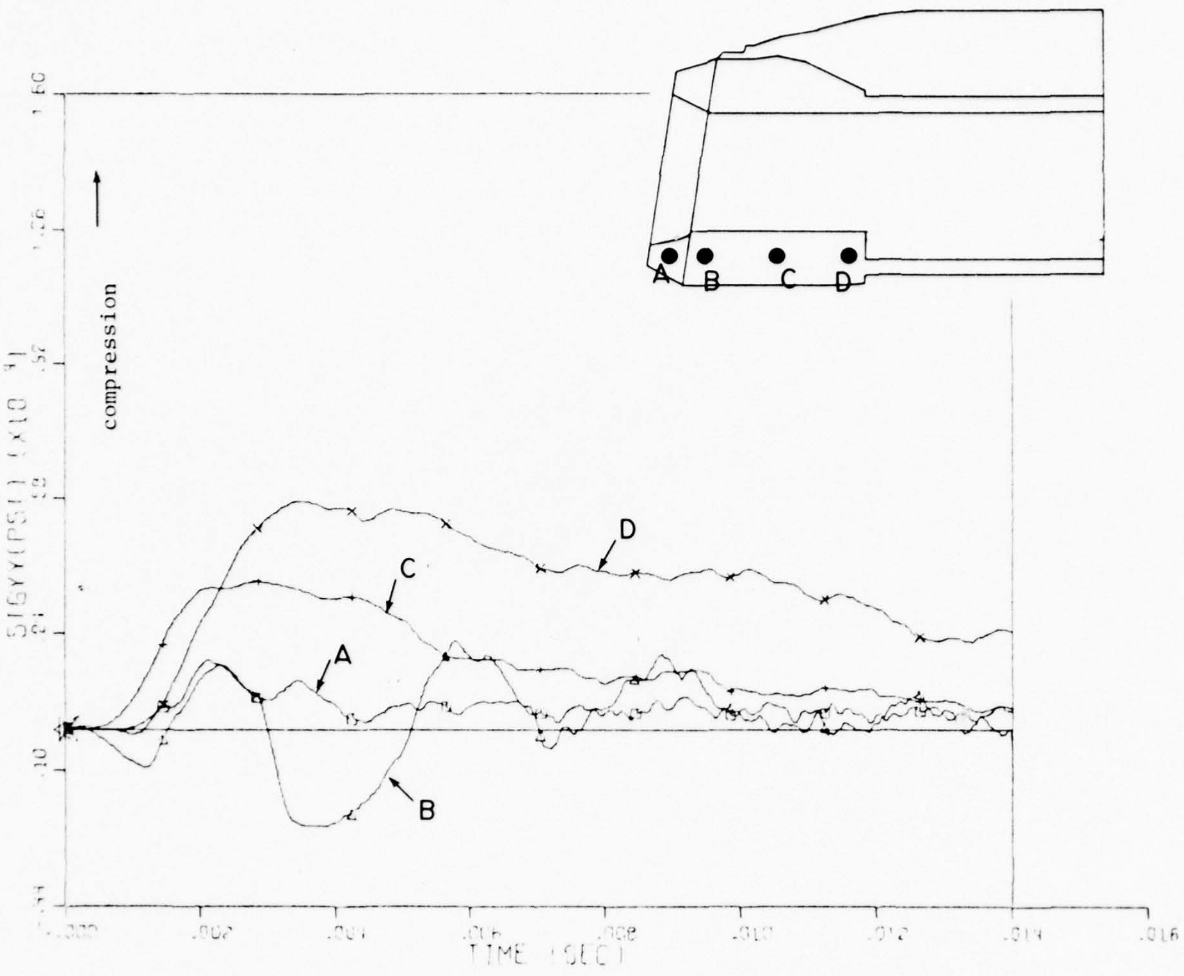

Figure 4-2b. Longitudinal Stress/Time Histories for Points Along Lower Headworks.

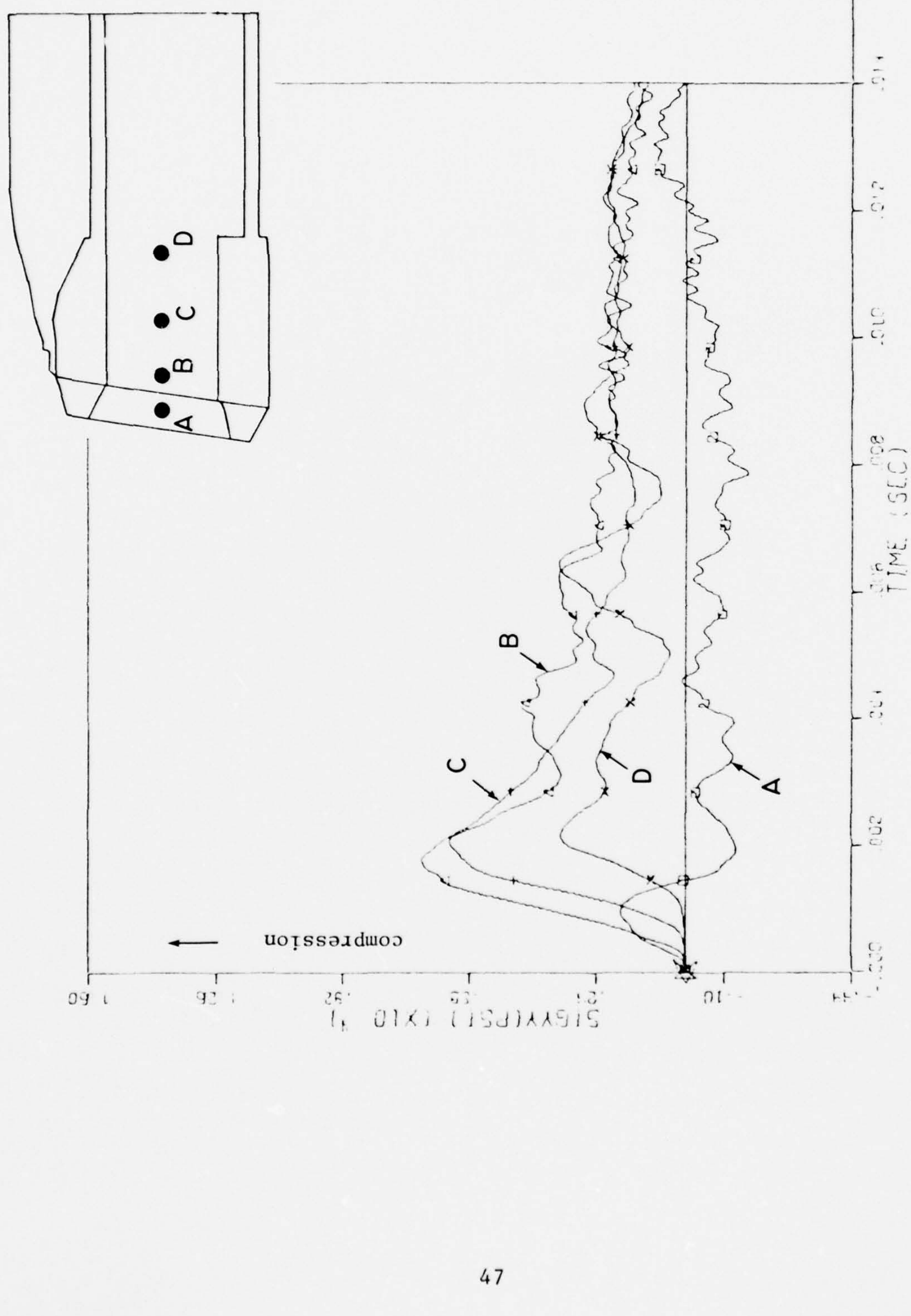

Figure 4-2c. Longitudinal Stress/Time Histories for Points Along Headworks Side.

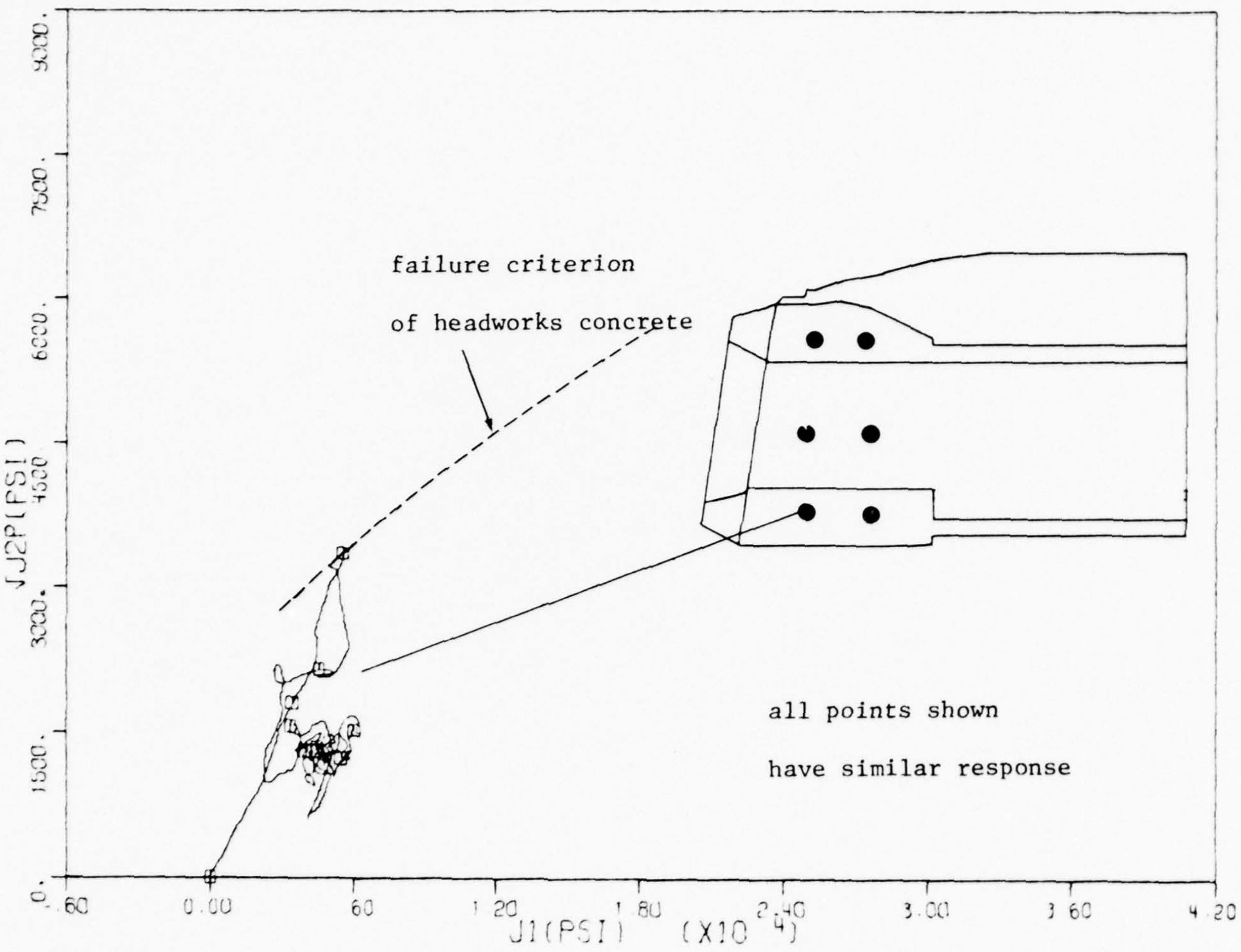

Figure 4-3. Typical Stress Invariant Plot for Concrete in Headworks.

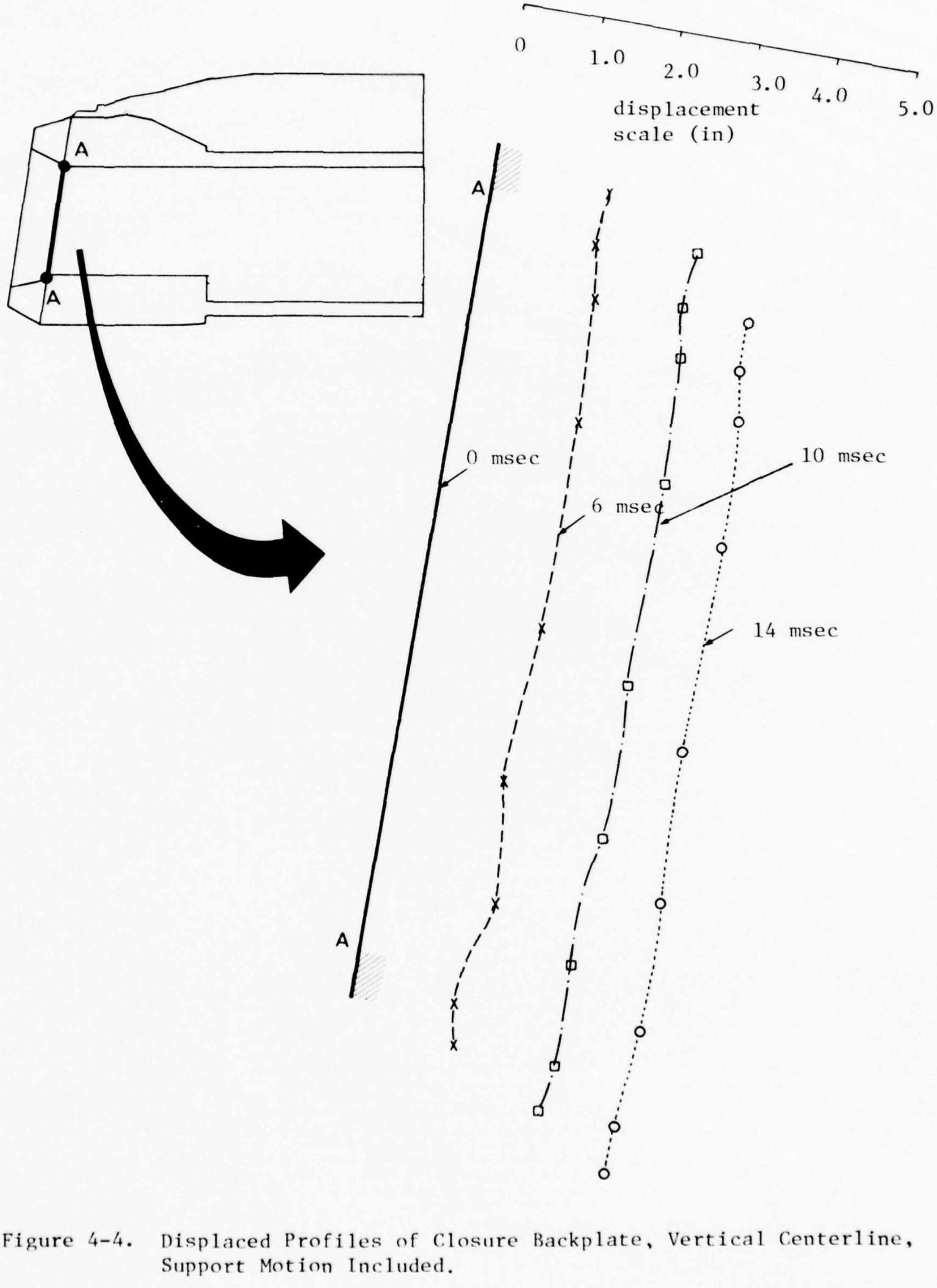

Figure 4-4. Displaced Profiles of Closure Backplate, Vertical Centerline, Support Motion Included.

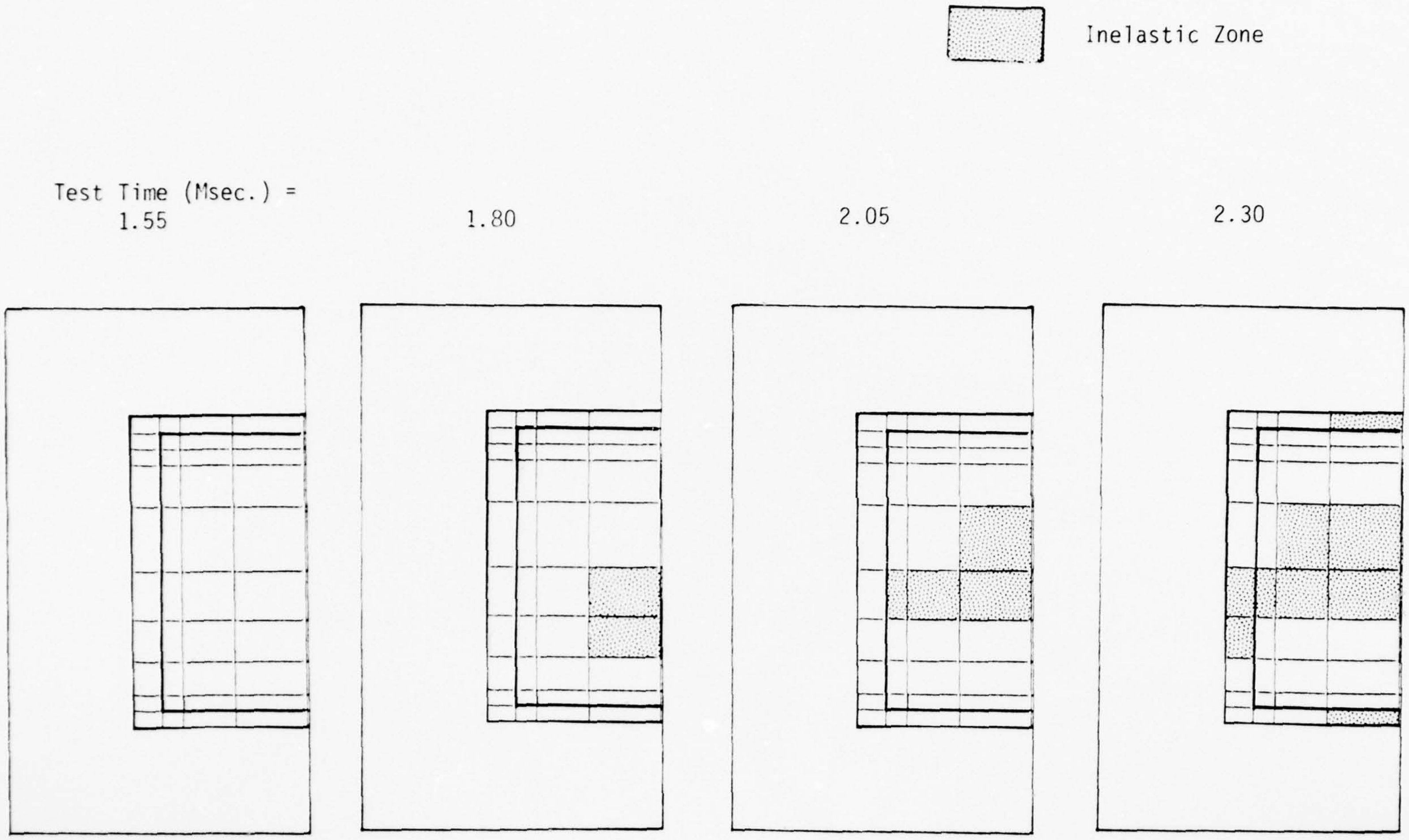

Figure 4-5a. Development of Inelastic Zones in Closure Backplate (Continued).

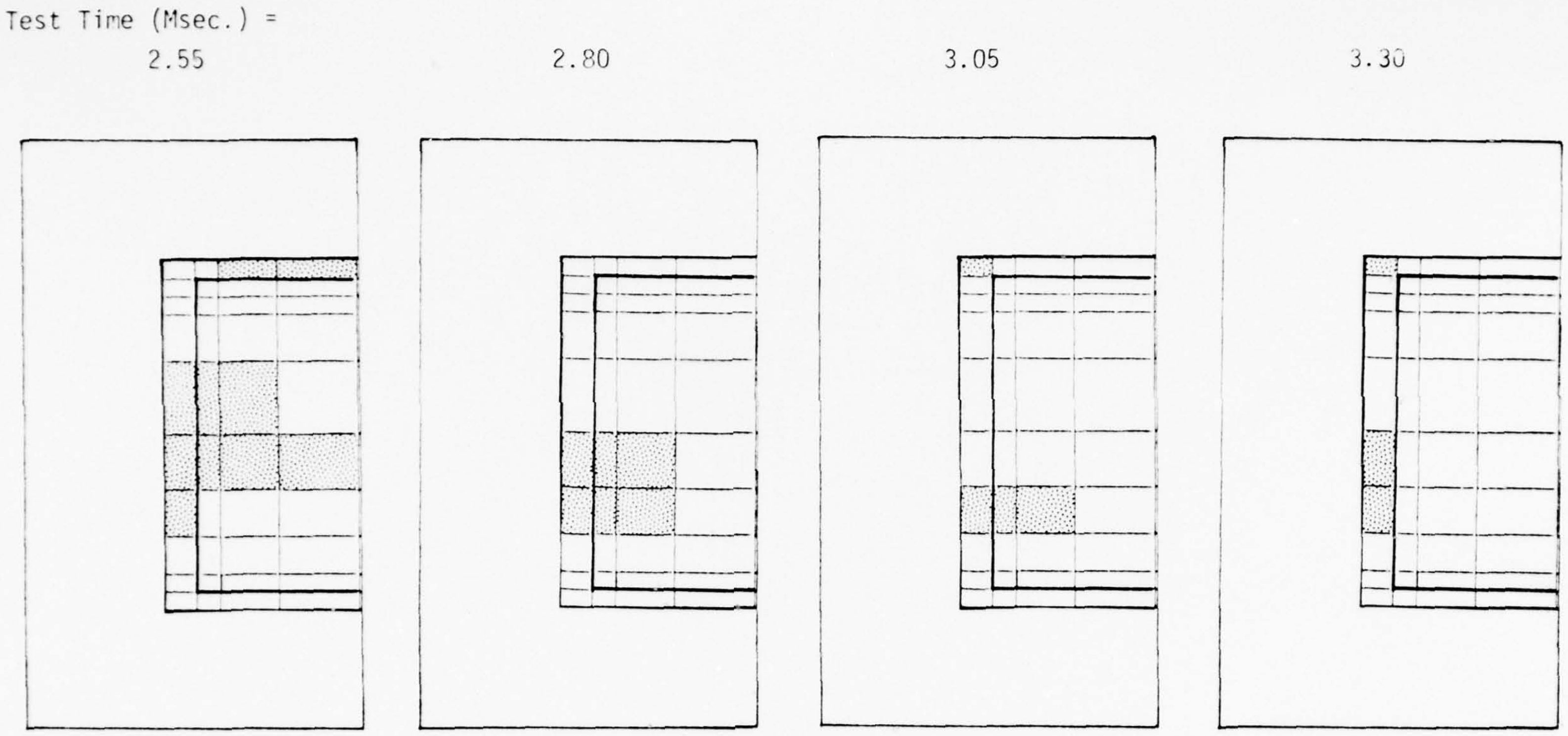

Figure 4-5b.

Development of Inelastic Zones in Closure Backplate (Continued).

Test Time = 1.55 Msec.

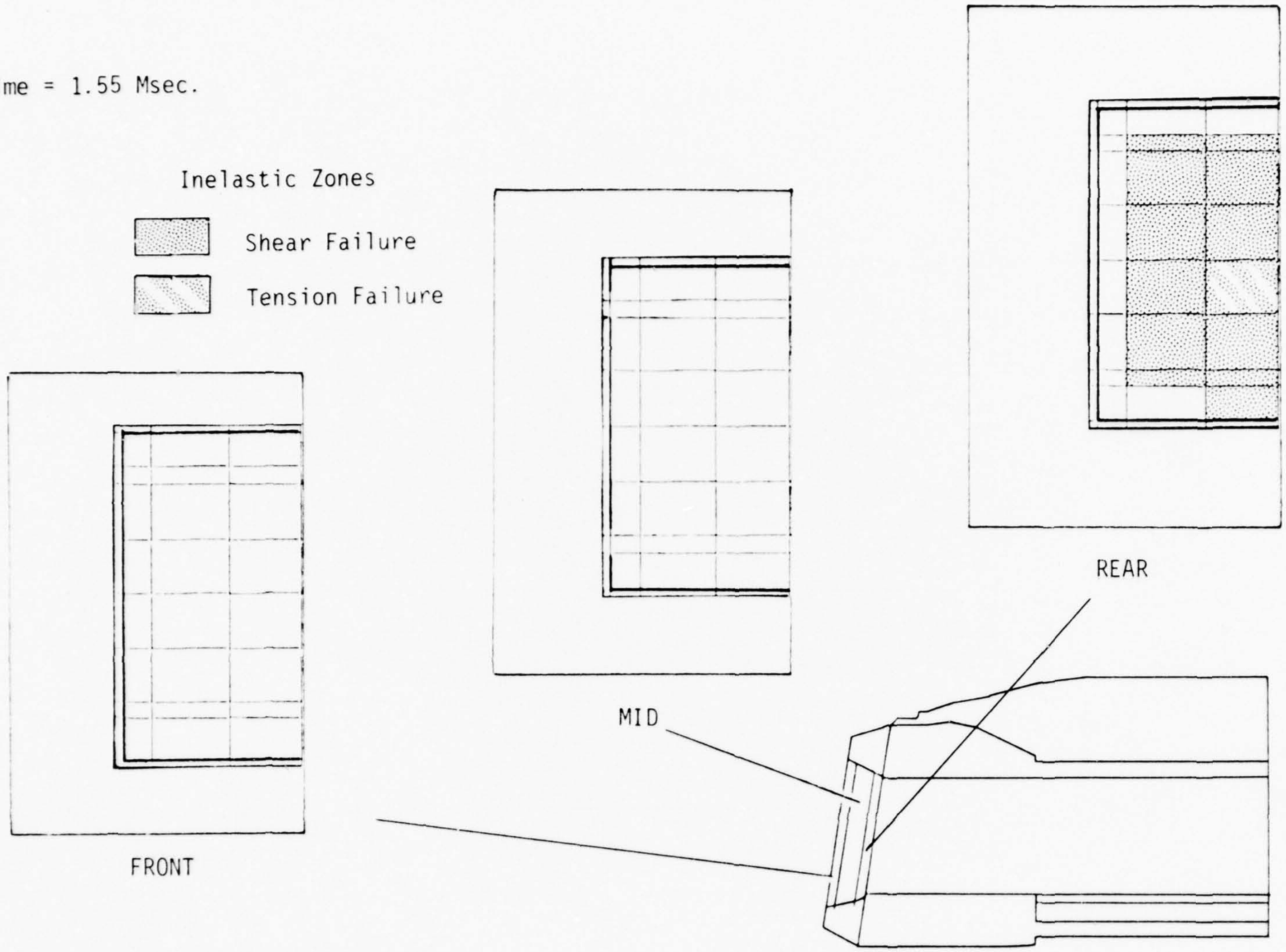

Figure 4-6a. Development of Inelastic Zones in Closure Concrete, Rise Time of Load is 1 Msec.

Test Time = 1.80 Msec.

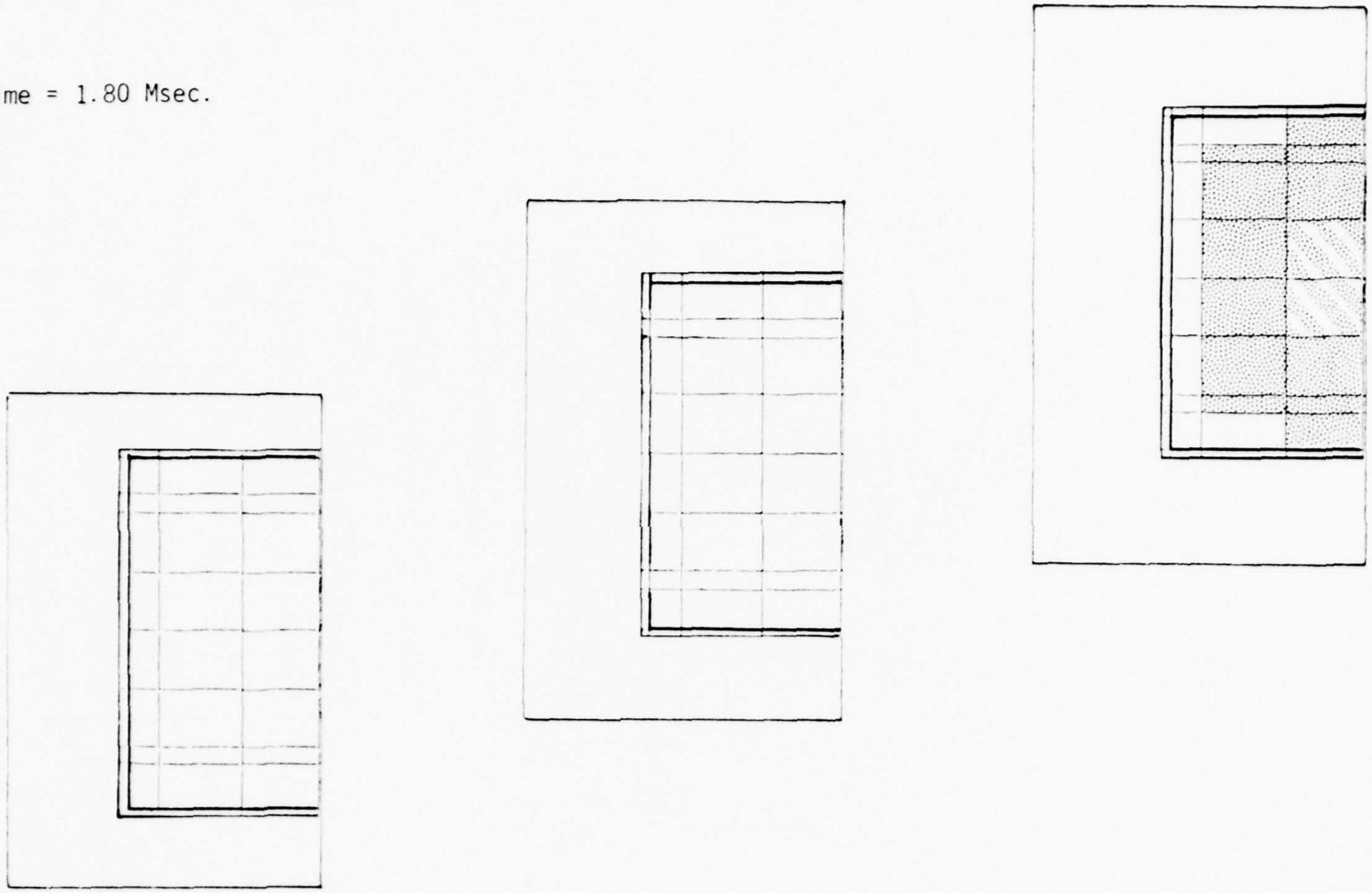

Figure 4-6b.

Development of Inelastic Zones in Closure Concrete, Rise Time of Load is 1 Msec (Continued).

Test Time = 2.30 Msec.

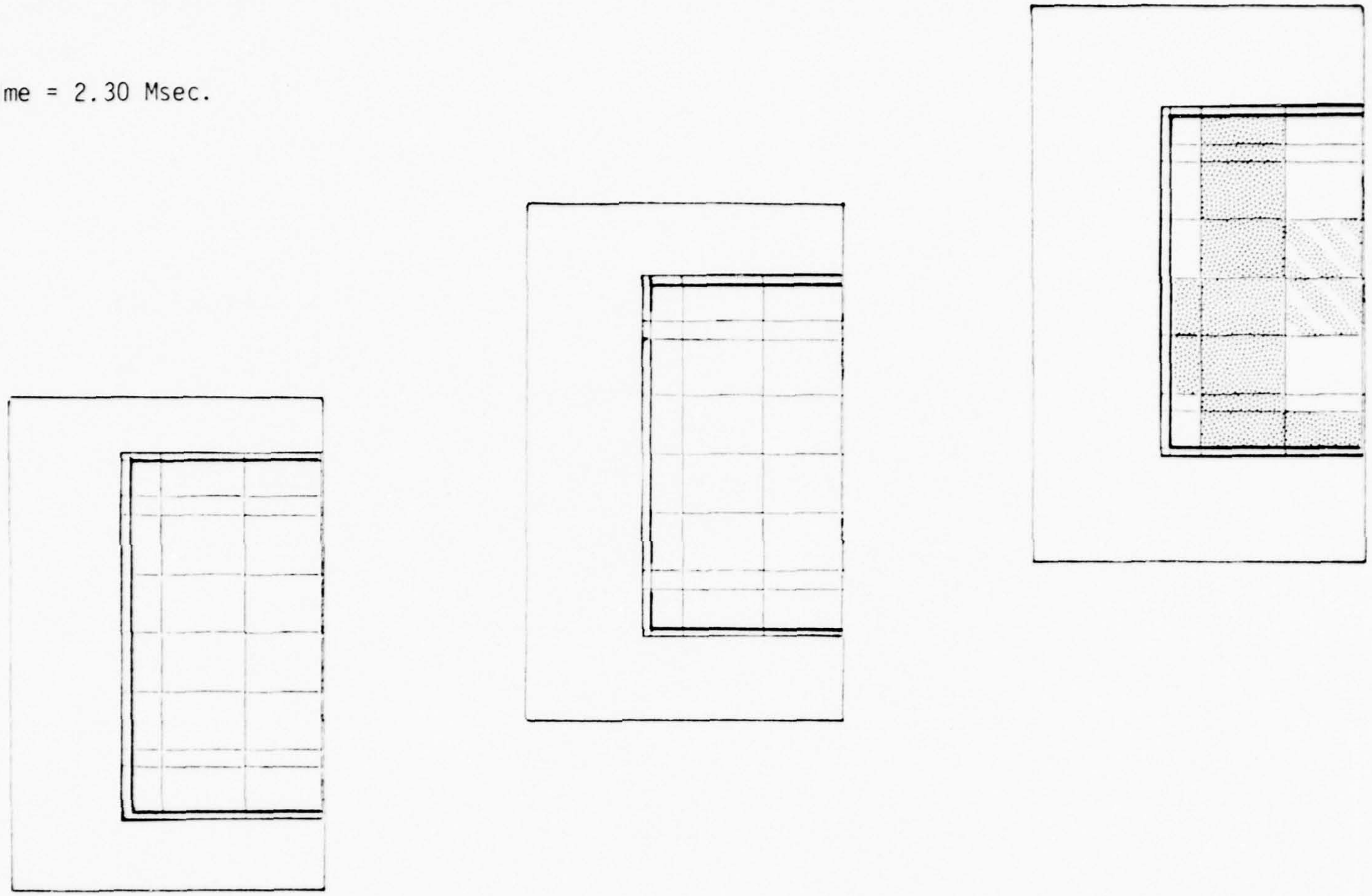

Figure 4-6c.
Development of Inelastic Zones in Closure Concrete, Rise Time of Load is 1 Msec (Continued).

Test Time = 3.30 Msec.

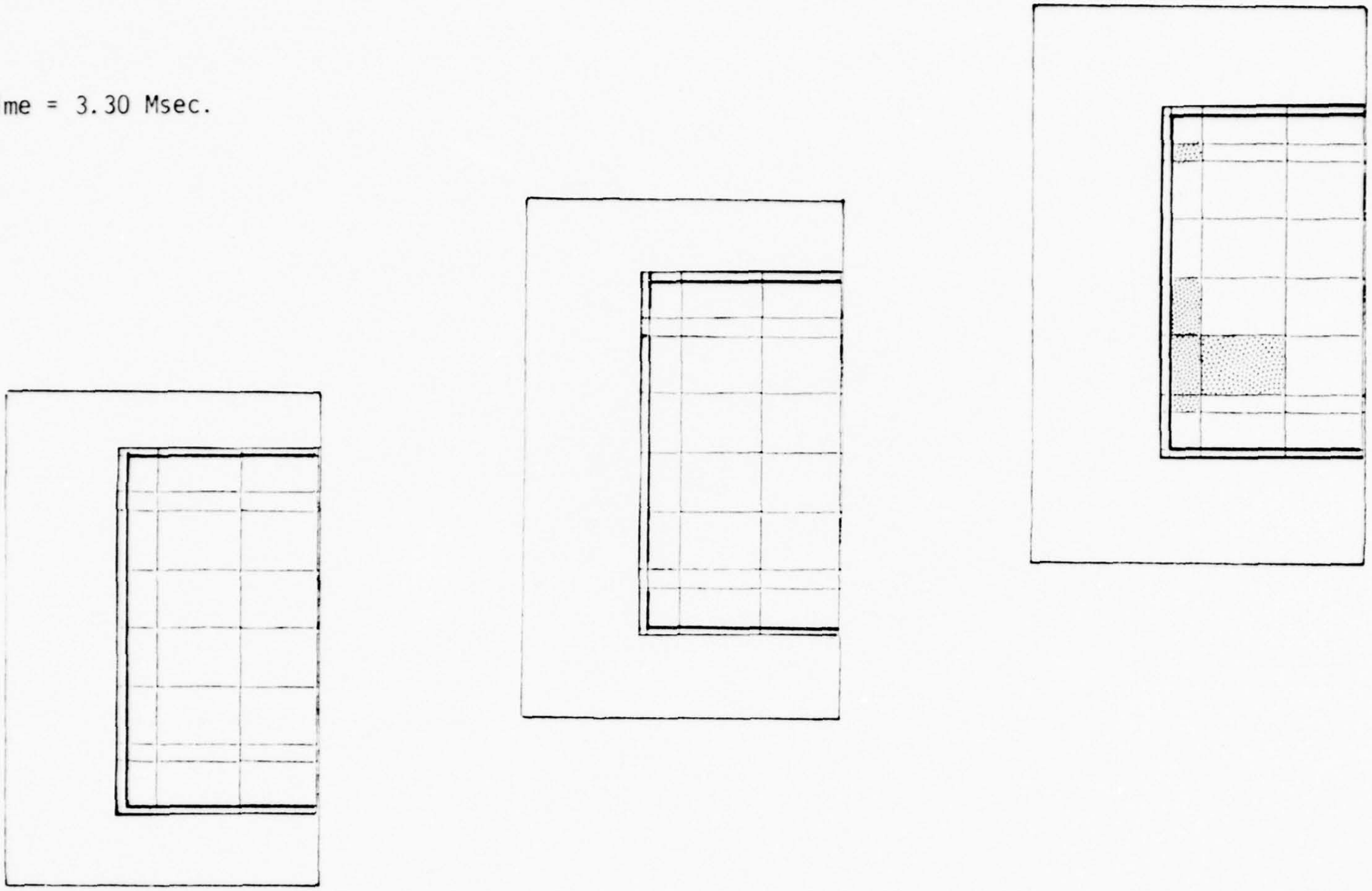

Figure 4-6d.

Development of Inelastic Zones in Closure Concrete, Rise Time of Load is 1 Msec (Continued).

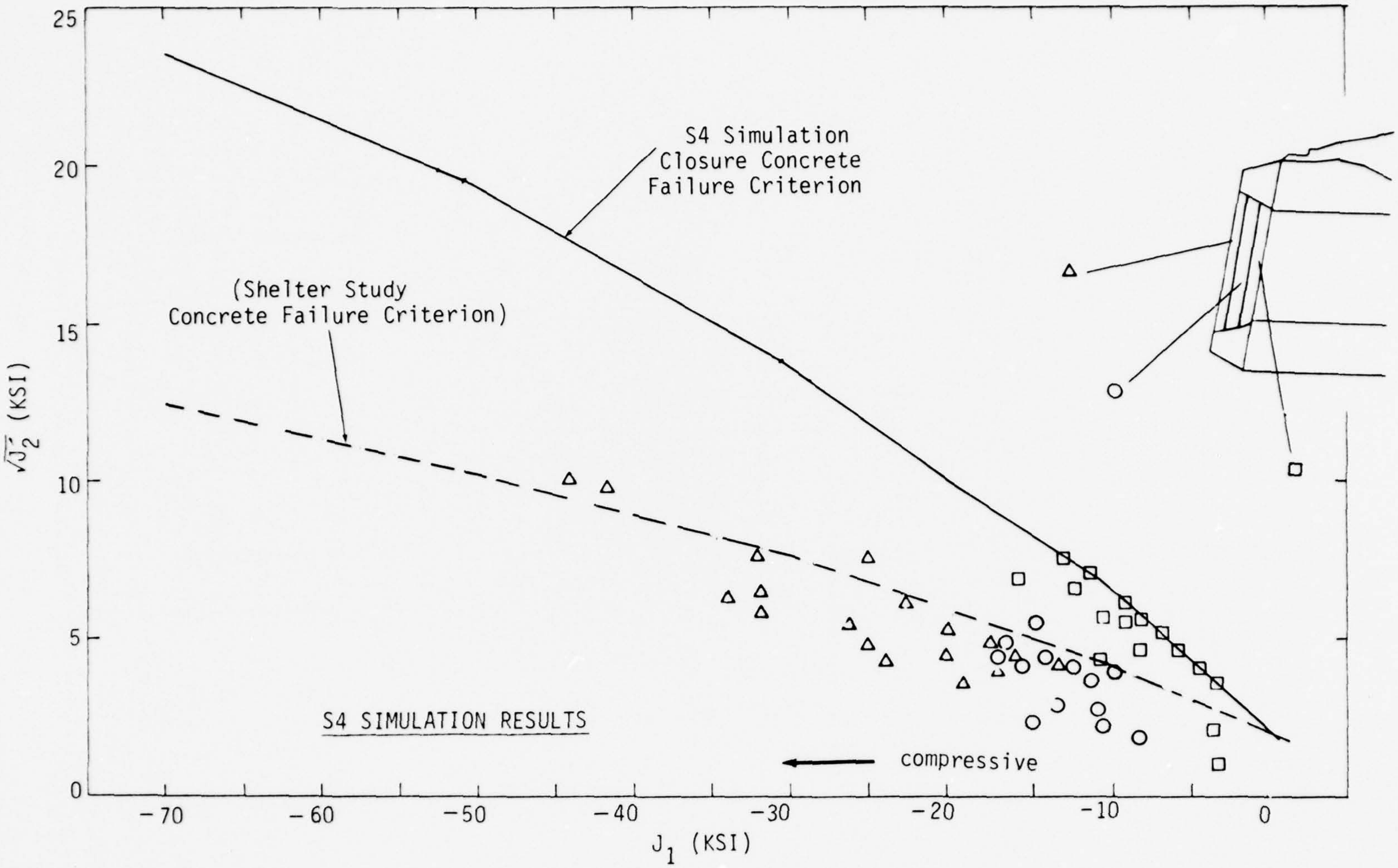

Figure 4-7. Distribution of Peak Closure Concrete Stresses in Stress Invariant Space.

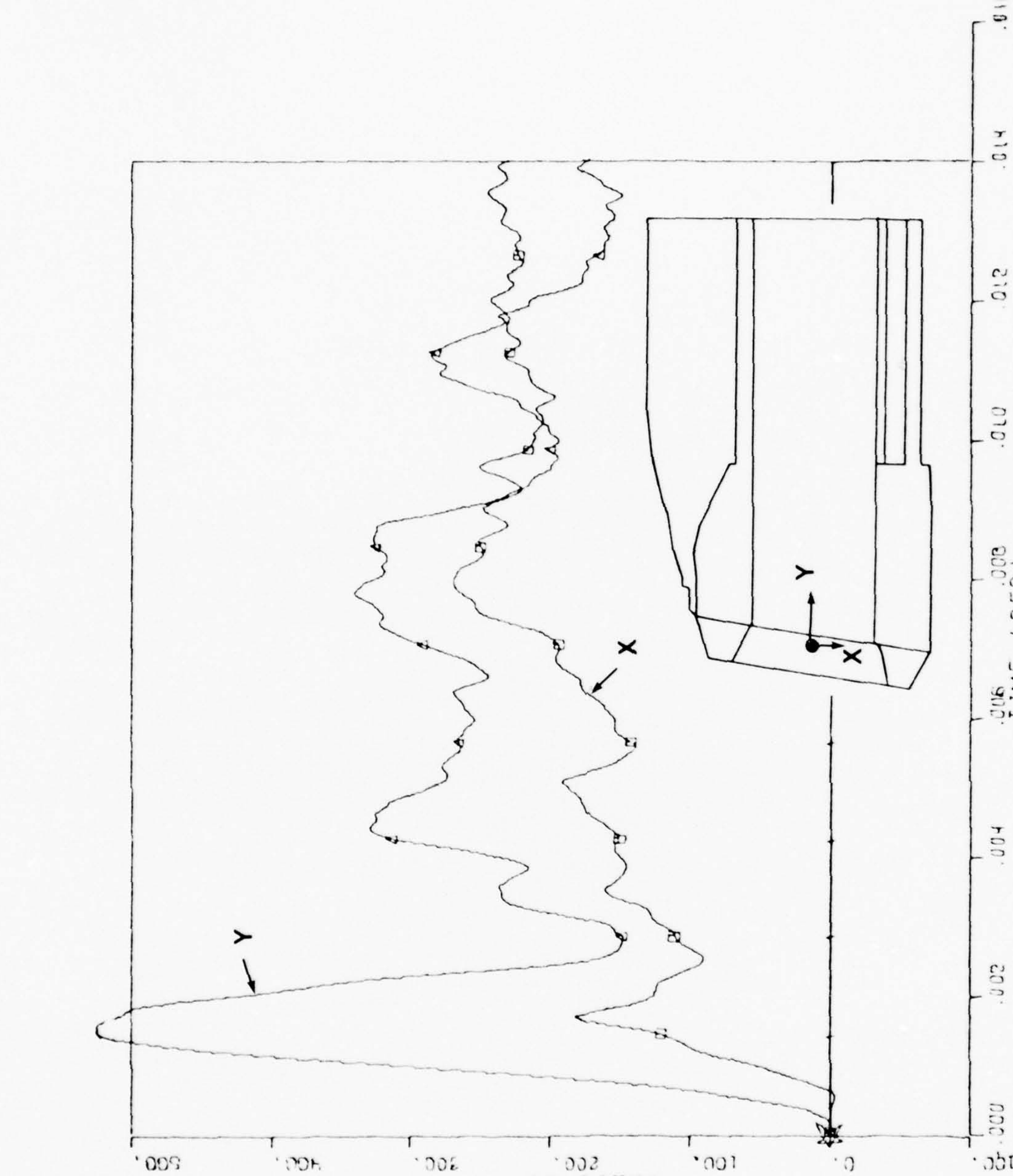

Figure 4-8. Absolute Velocity/Time Histories, Closure Center of Gravity (cg).

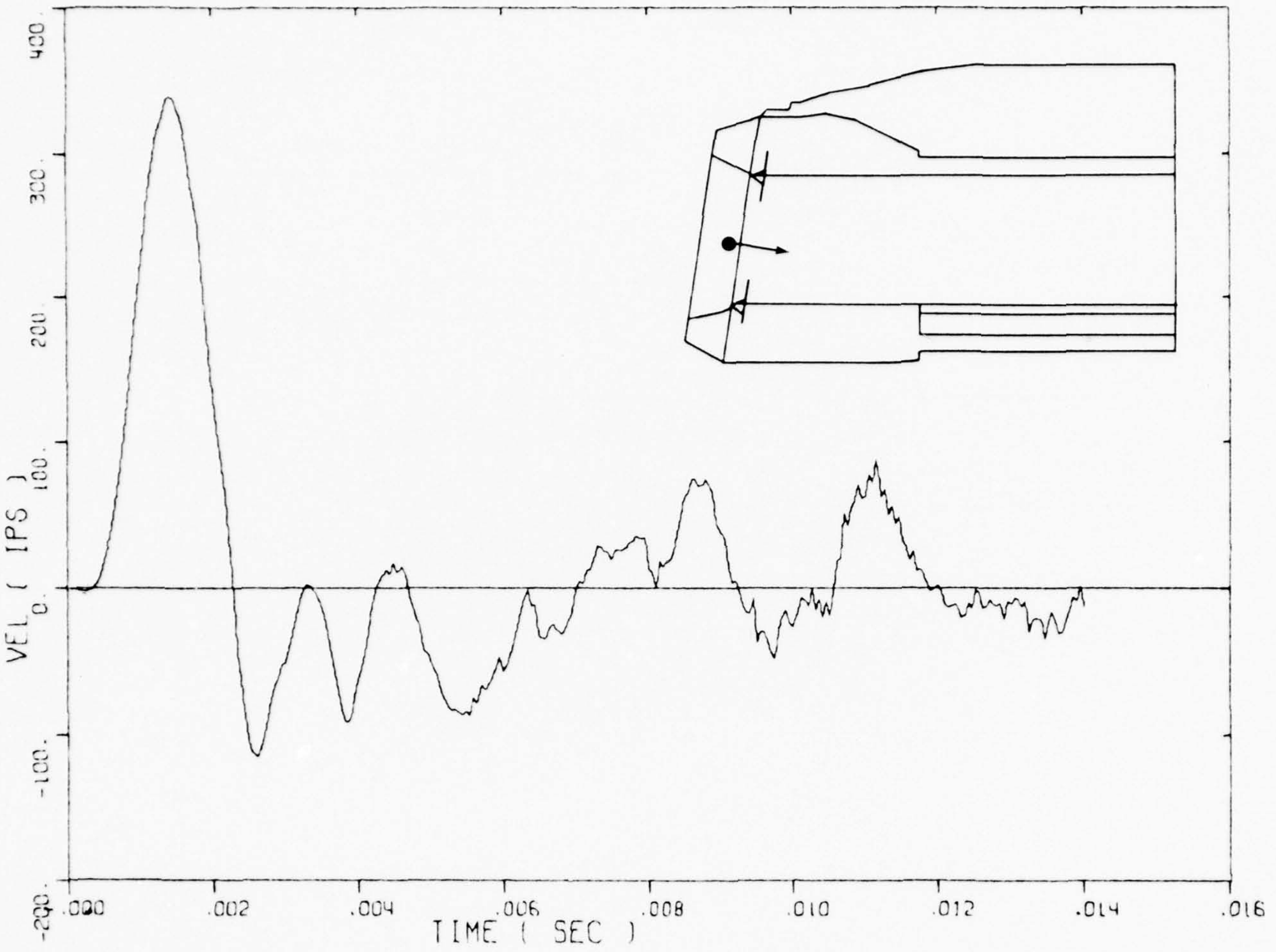

Figure 4-9. Velocity/Time History of Closure cg, Component Perpendicular to Backplate, Relative to Support Motion.

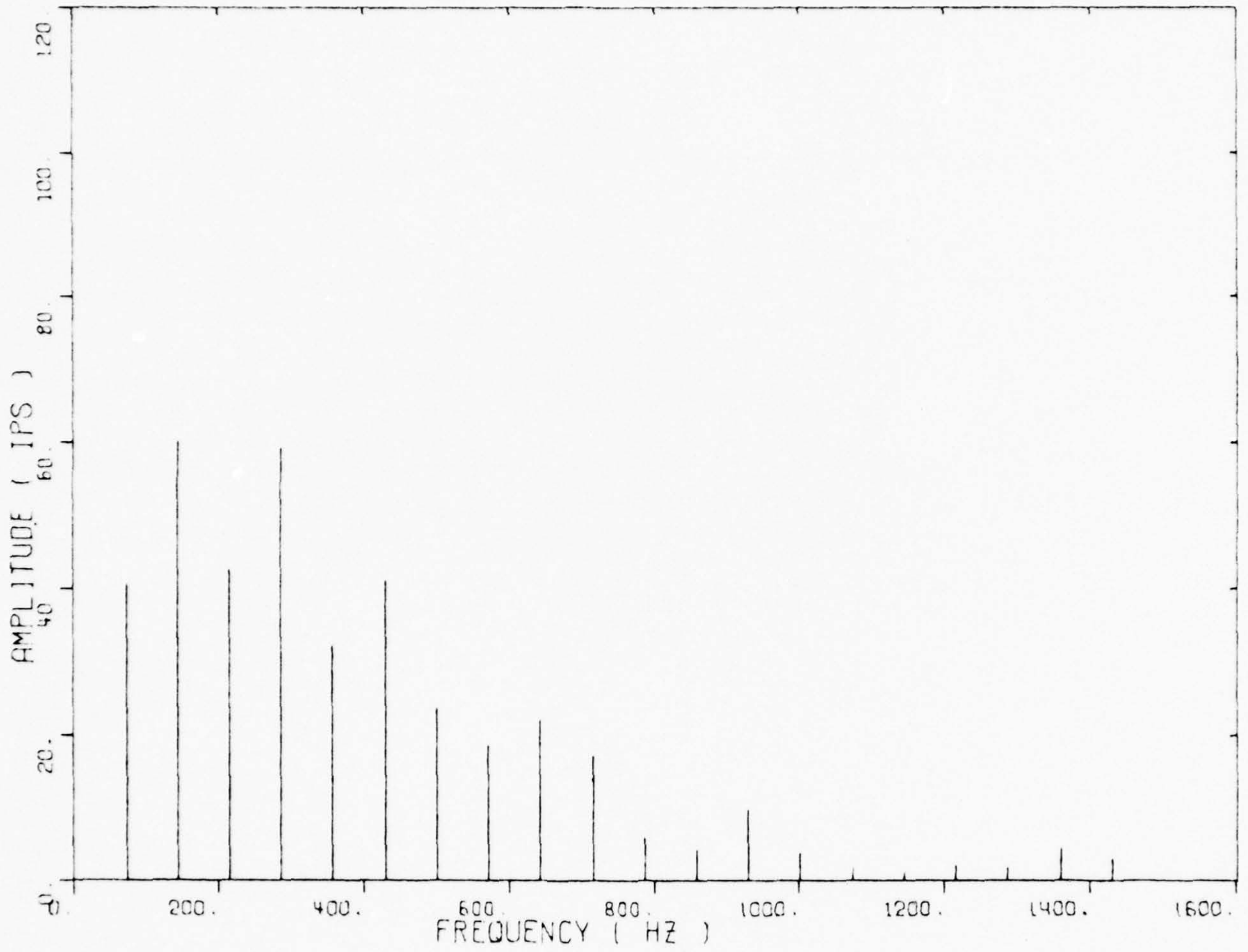

Figure 4-10. Fourier Decomposition of Closure cg Relative Velocity of Figure 4-9.

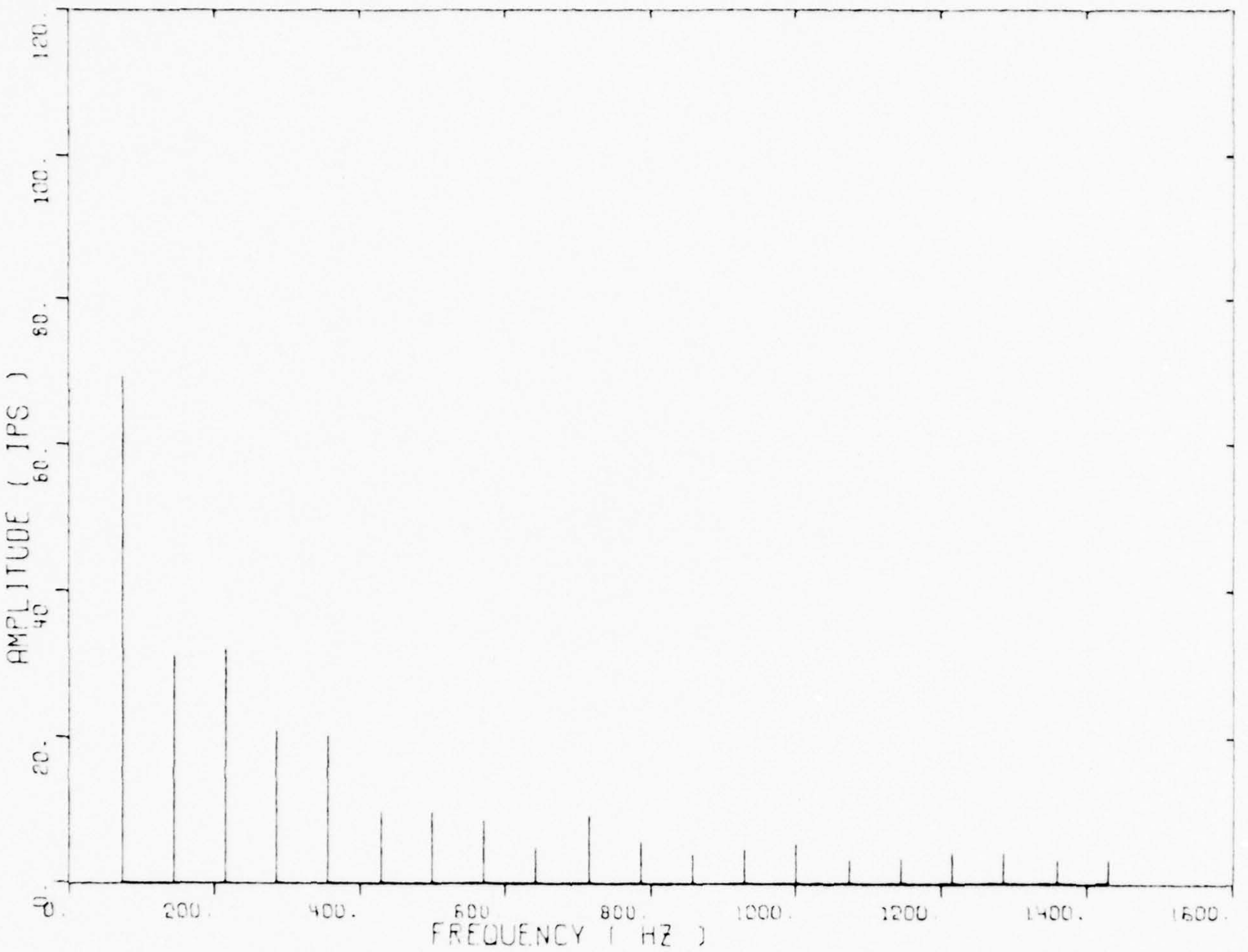

Figure 4-11a. Fourier Decomposition of Average Closure Support Motion, Vertical Component.

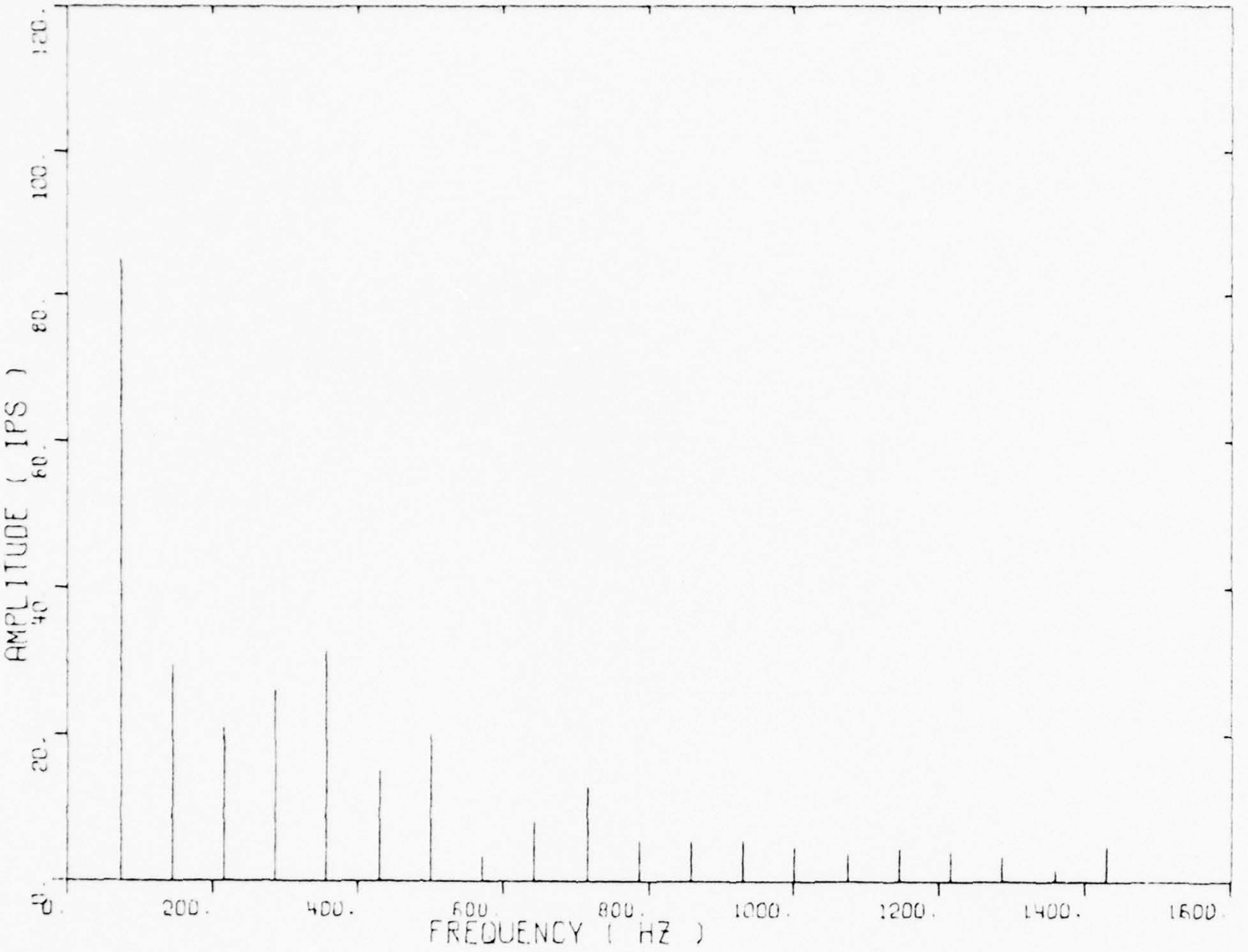

Figure 4-11b. Fourier Decomposition of Average Closure Support Motion, Longitudinal Component.

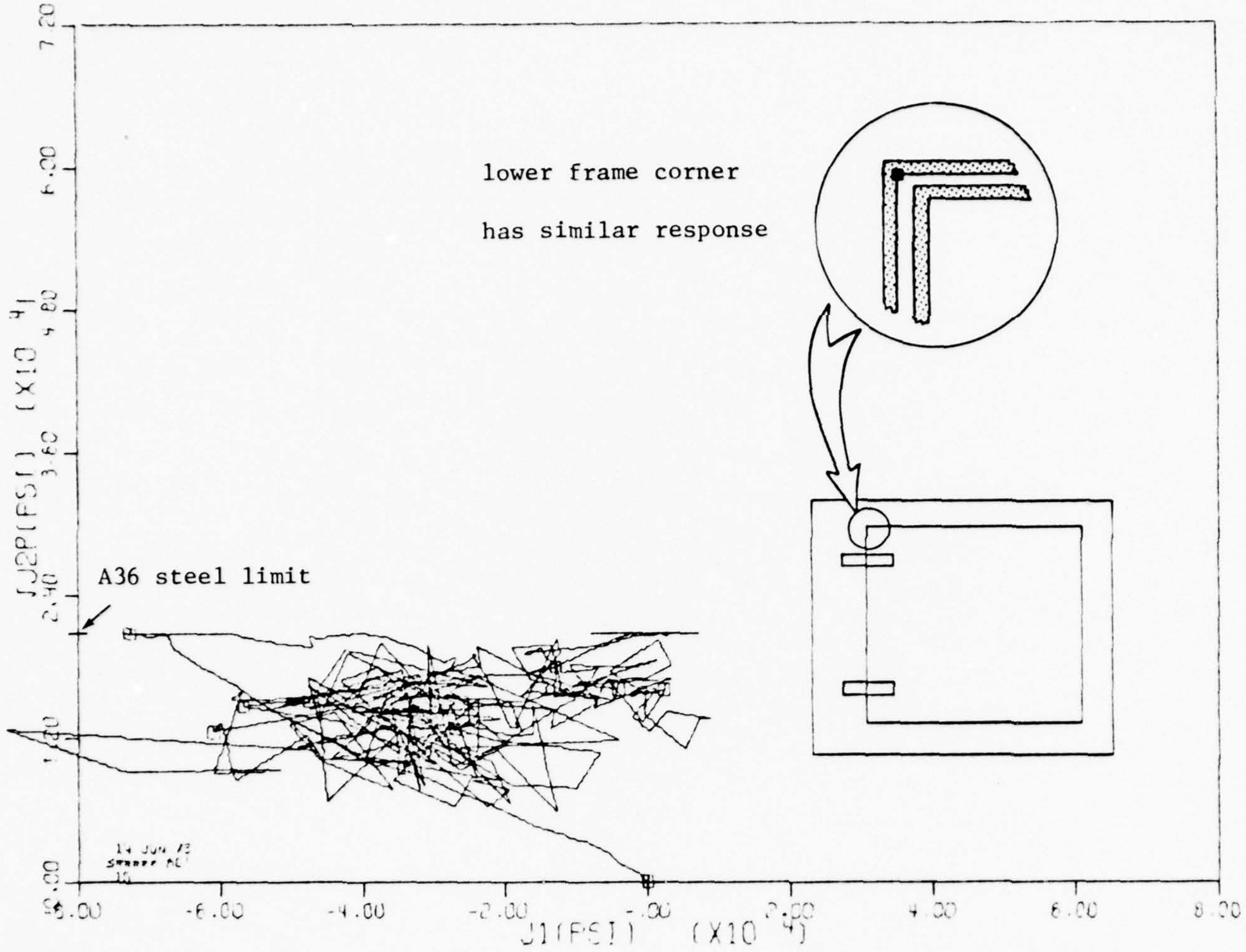

Figure 4-12a. Stress Invariant Plot for Steel in Upper Frame Corner, Inner Lining.

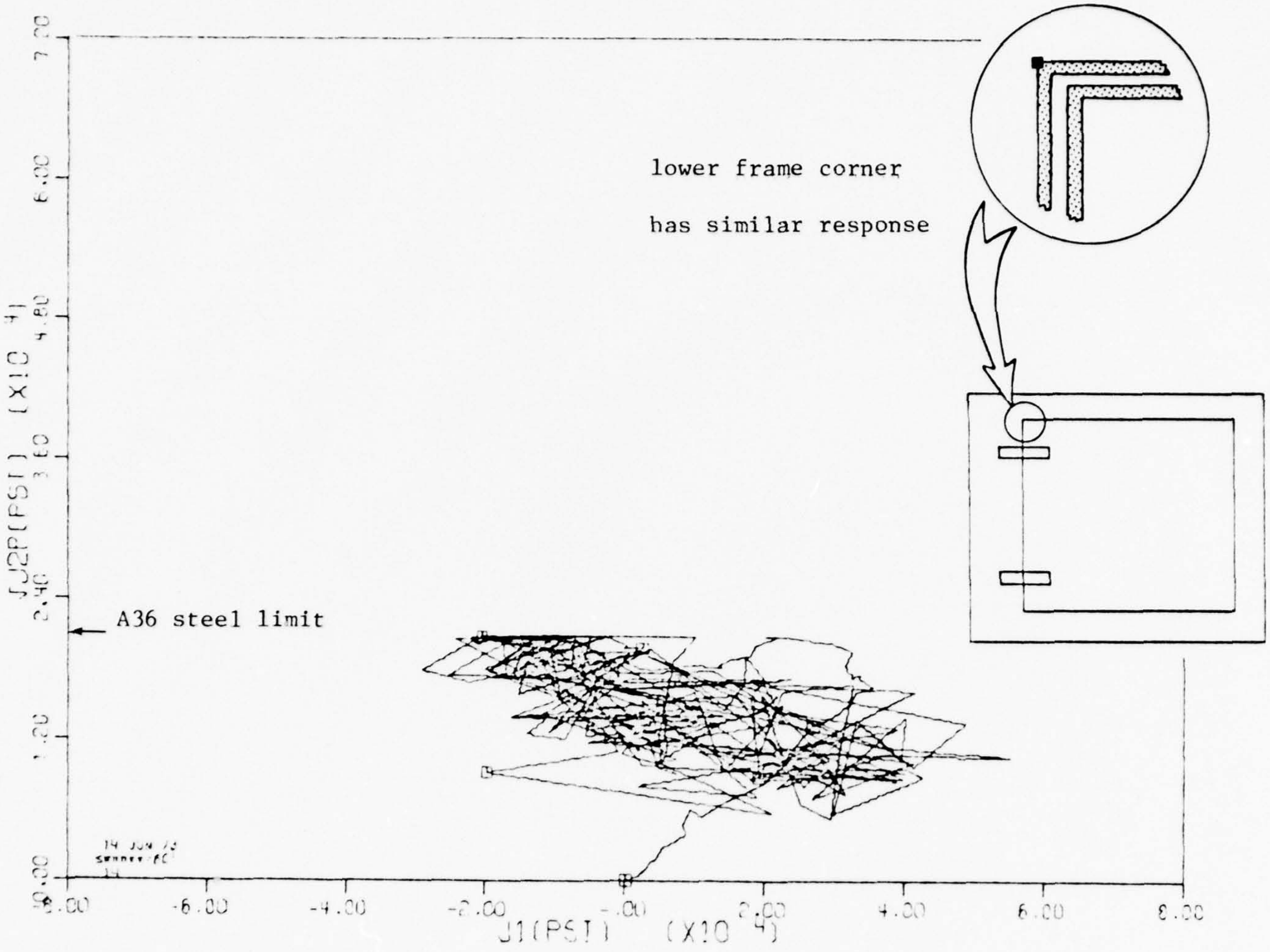

Figure 4-12b. Stress Invariant Plot for Steel in Upper Frame Corner, Outer Lining.

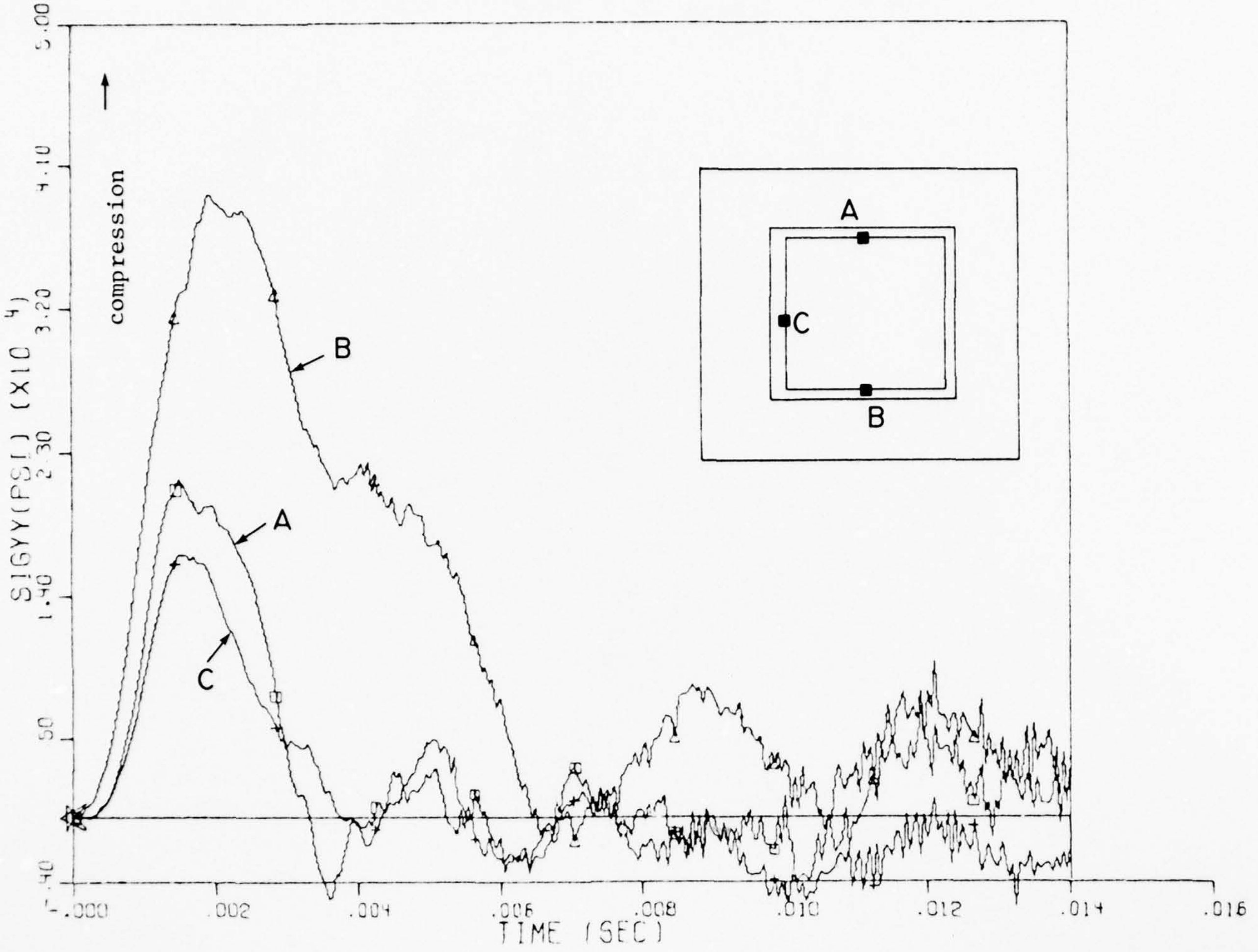

Figure 4-13. Bearing Pressure at Bearing Plate.

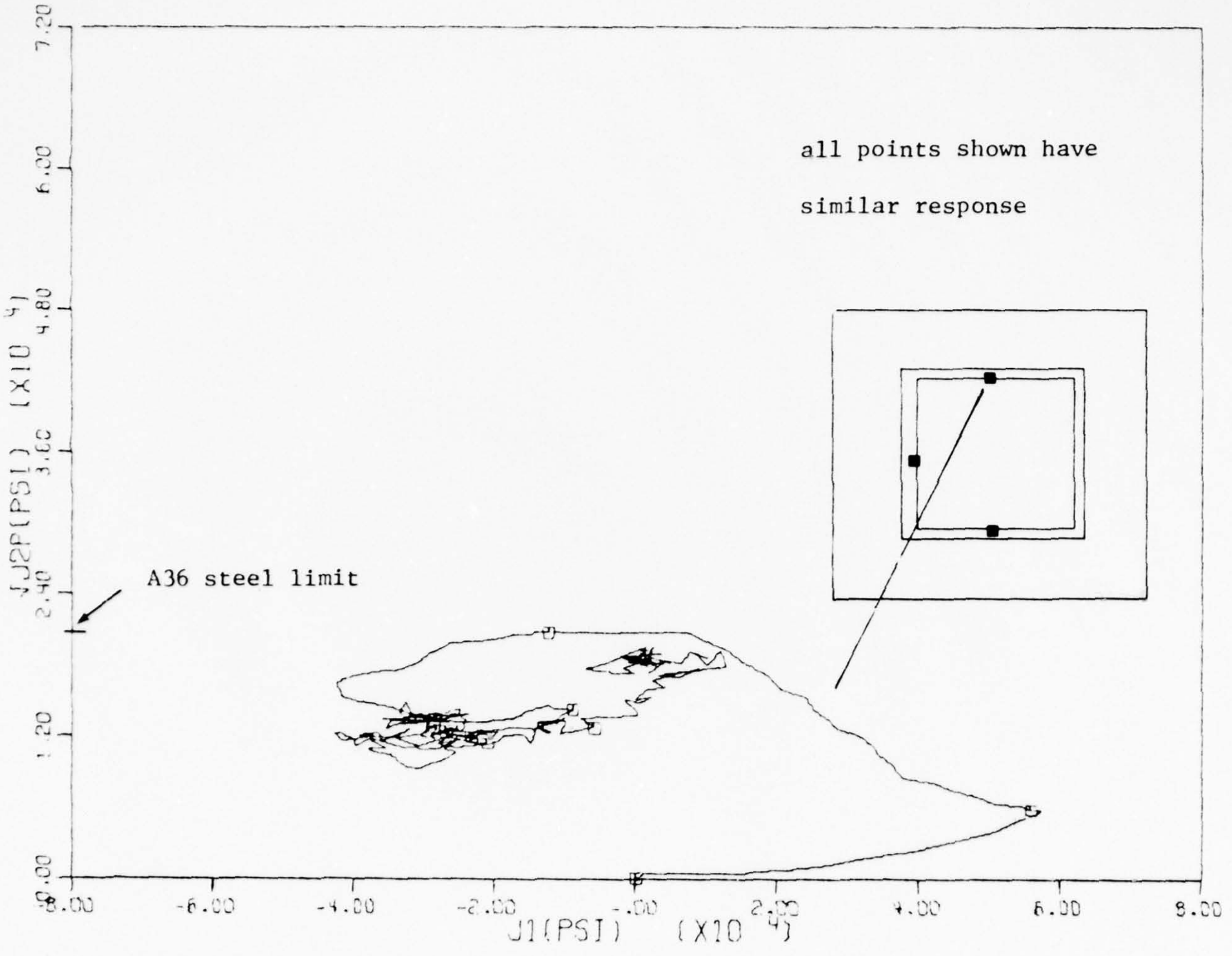

A36 steel limit

all points shown have similar response

Figure 4-14. Typical Stress Invariant Plot for Steel in Bearing Ring.

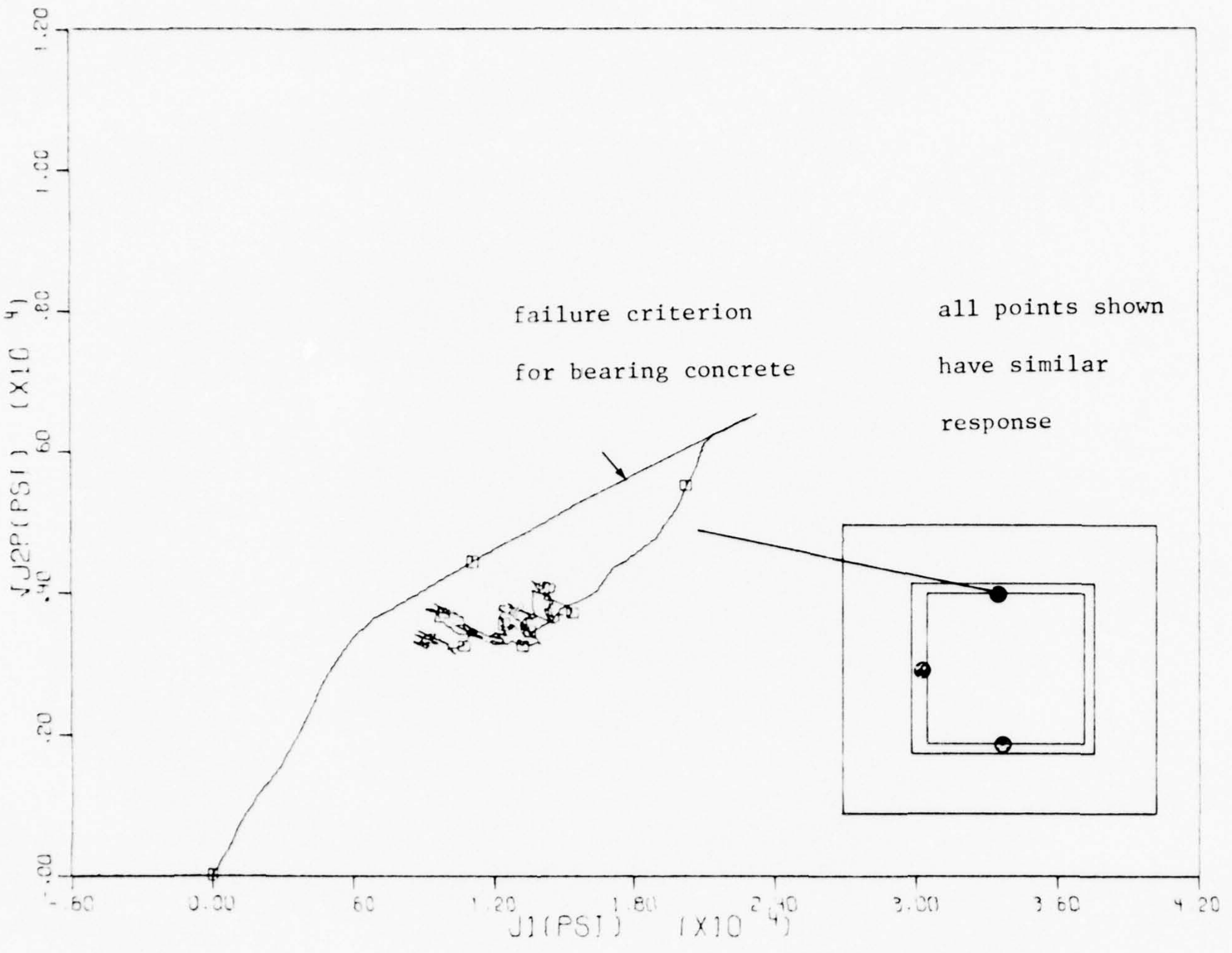

Figure 4-15. Typical Stress Invariant Plot for Concrete Behind Bearing Ring.

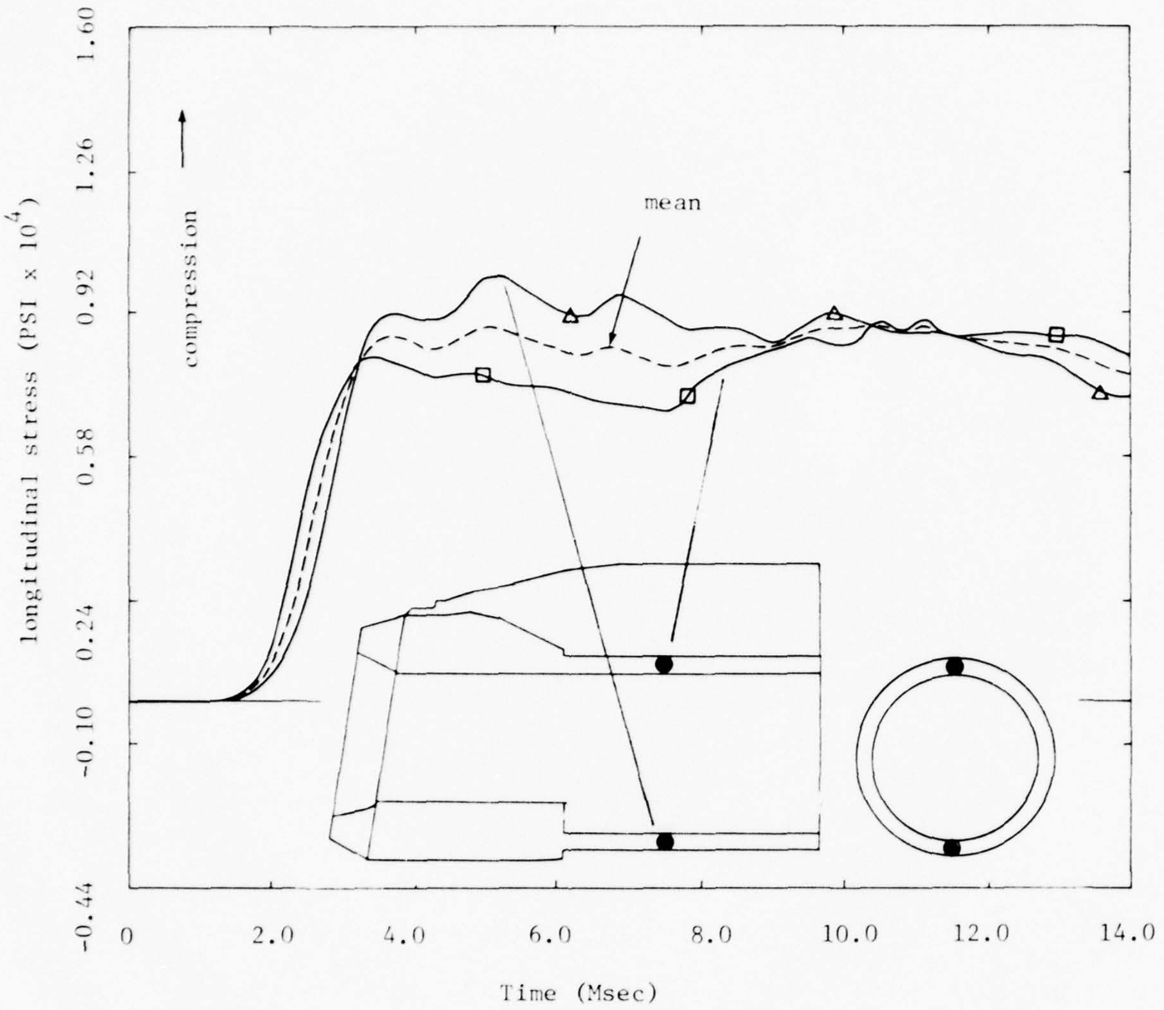

Figure 4-16. Longitudinal Stress/Time Histories for Points at Tube Section Half-Tube Diameter Behind Headworks.

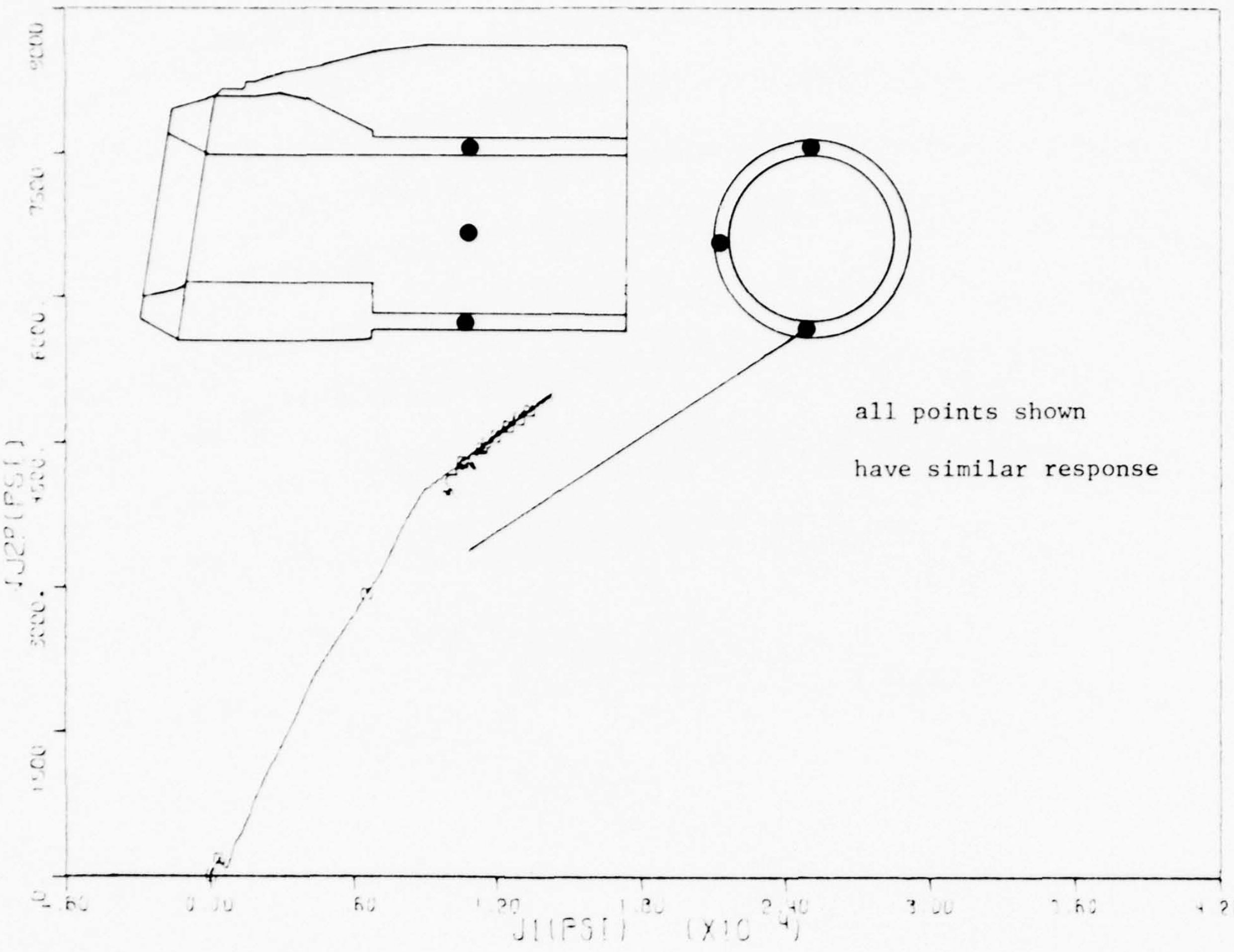

Figure 4-17. Typical Stress Invariant Plot for Concrete in Tube Section Half-Tube Diameter Behind Headworks.

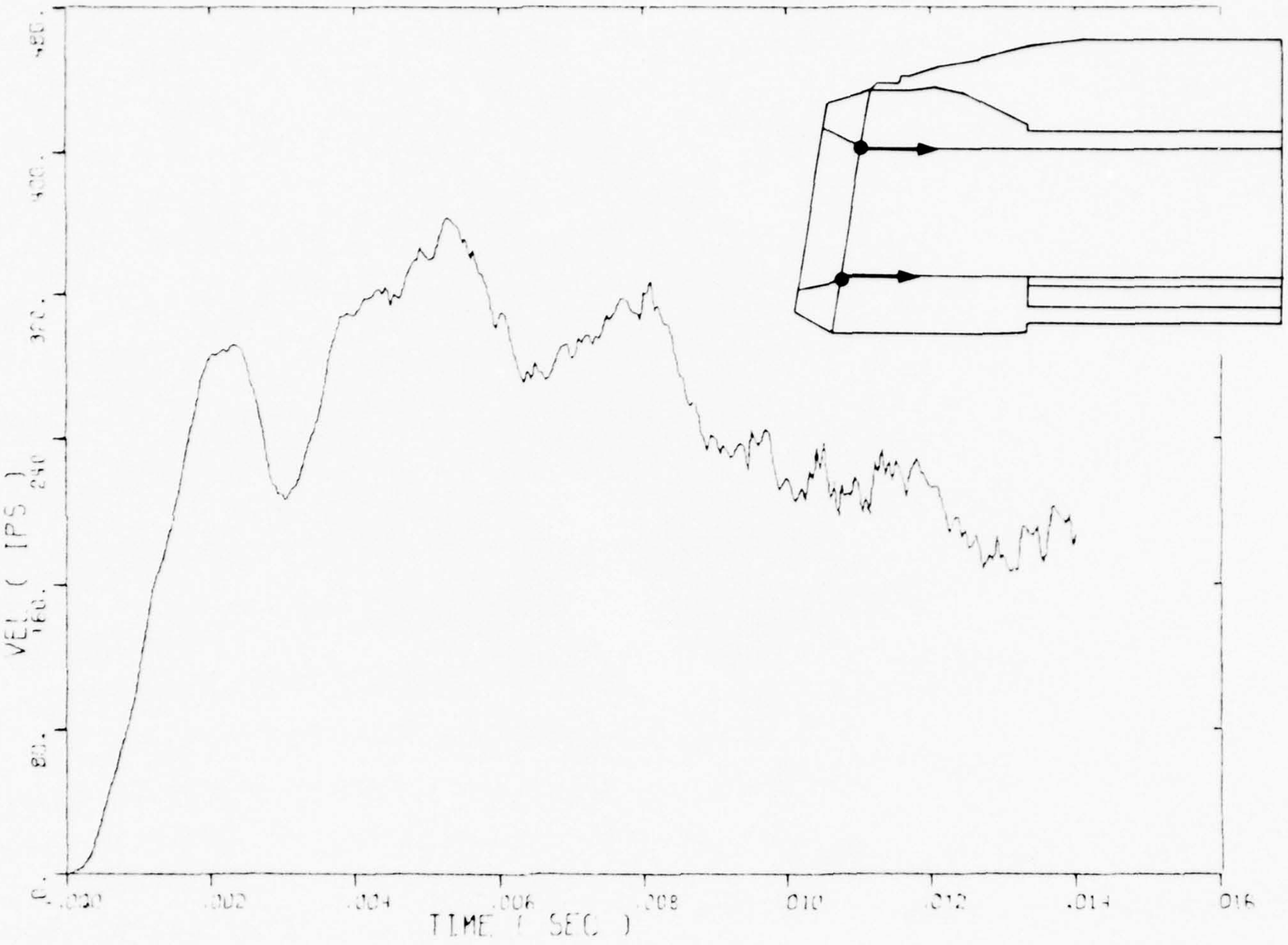

Figure 4-18. Mean Closure Support (or Average Headworks) Velocity/Time History, Longitudinal Component.

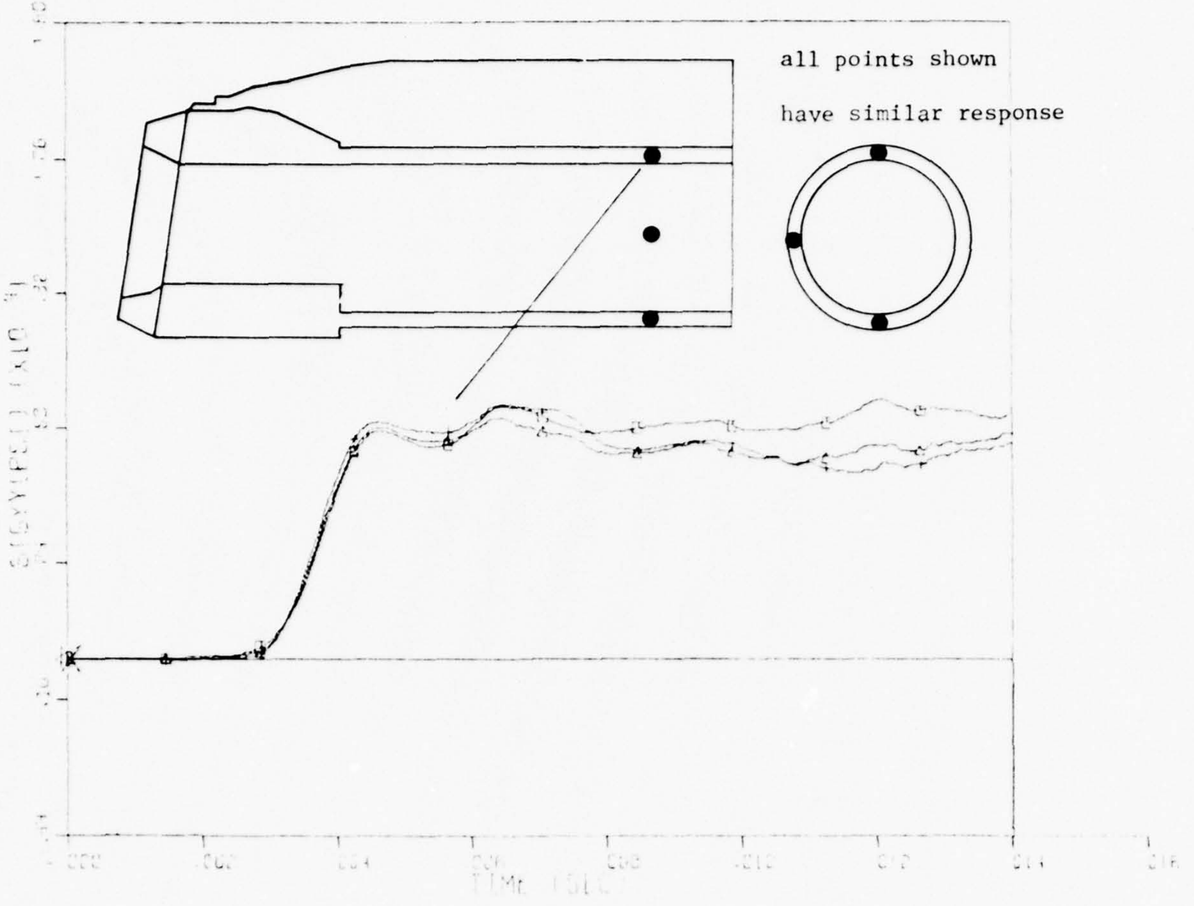

Figure 4-19. Longitudinal Stress/Time Histories for Points of Tube Section Two-Tube Diameters Behind Headworks.

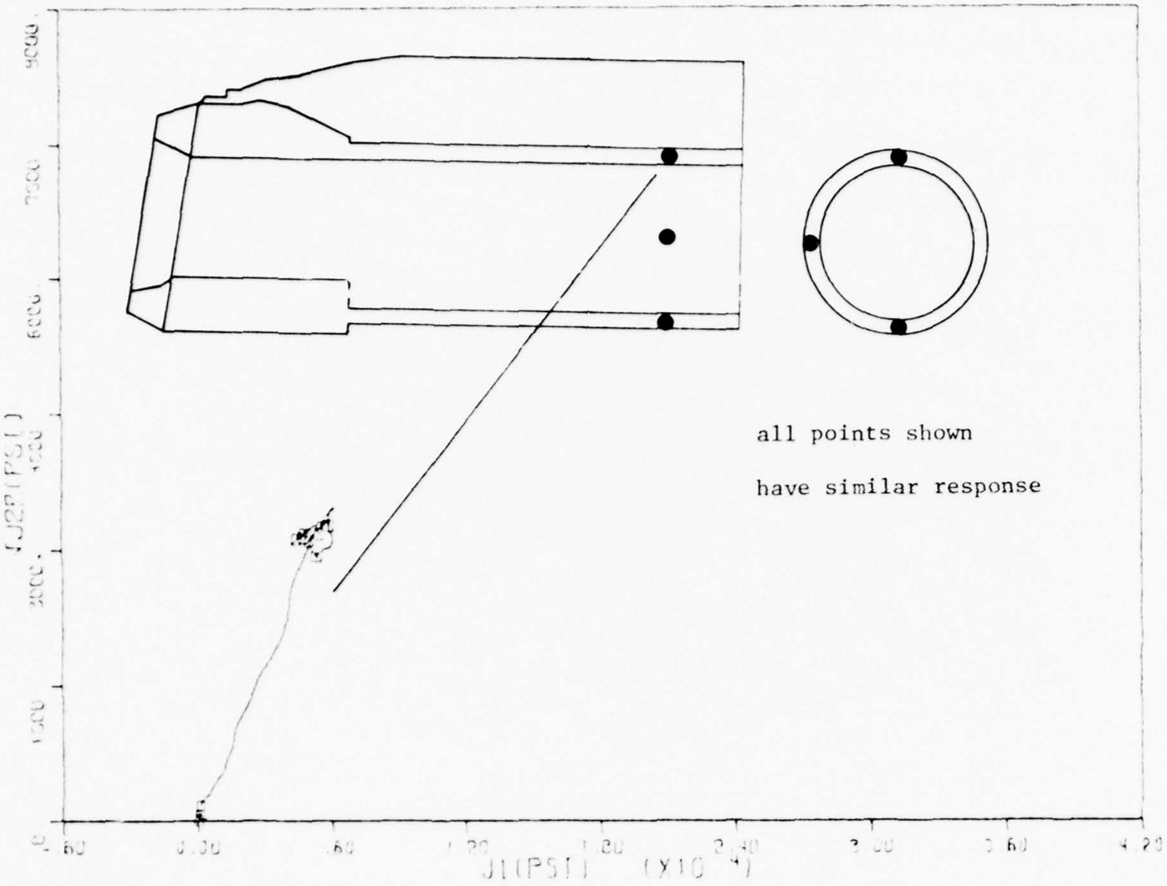

Figure 4-20. Typical Stress Invariant Plot for Concrete in Tube Section Two-Tube Diameters Behind Headworks.

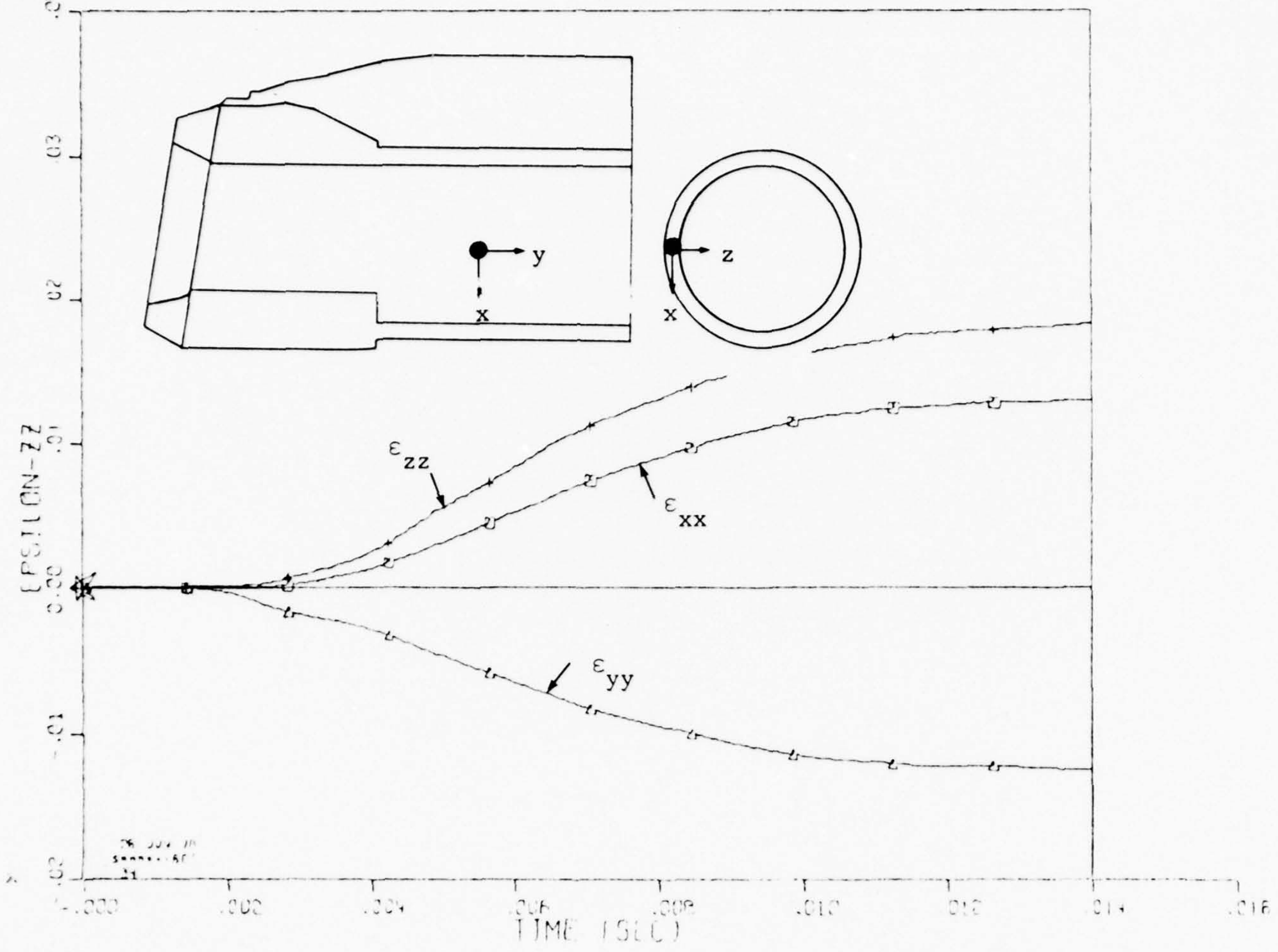

Figure 4-21a. Normal Strain/Time Histories for a Point at Springline of Tube Section Half-Tube Diameter Behind Headworks.

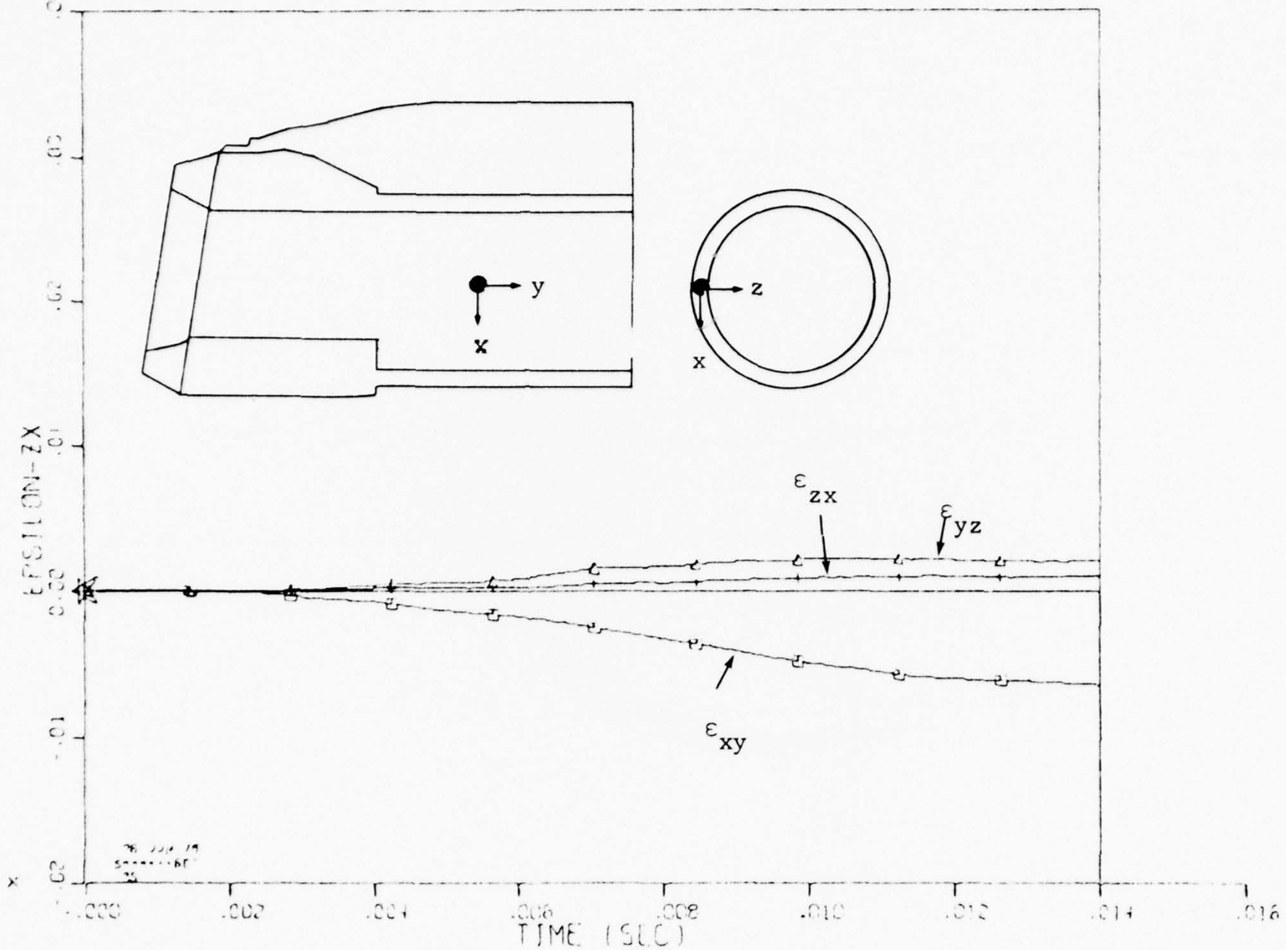

Figure 4-21b. Shear Strain/Time Histories for a Point at Springline of Tube Section Half-Tube Diameter Behind Headworks.

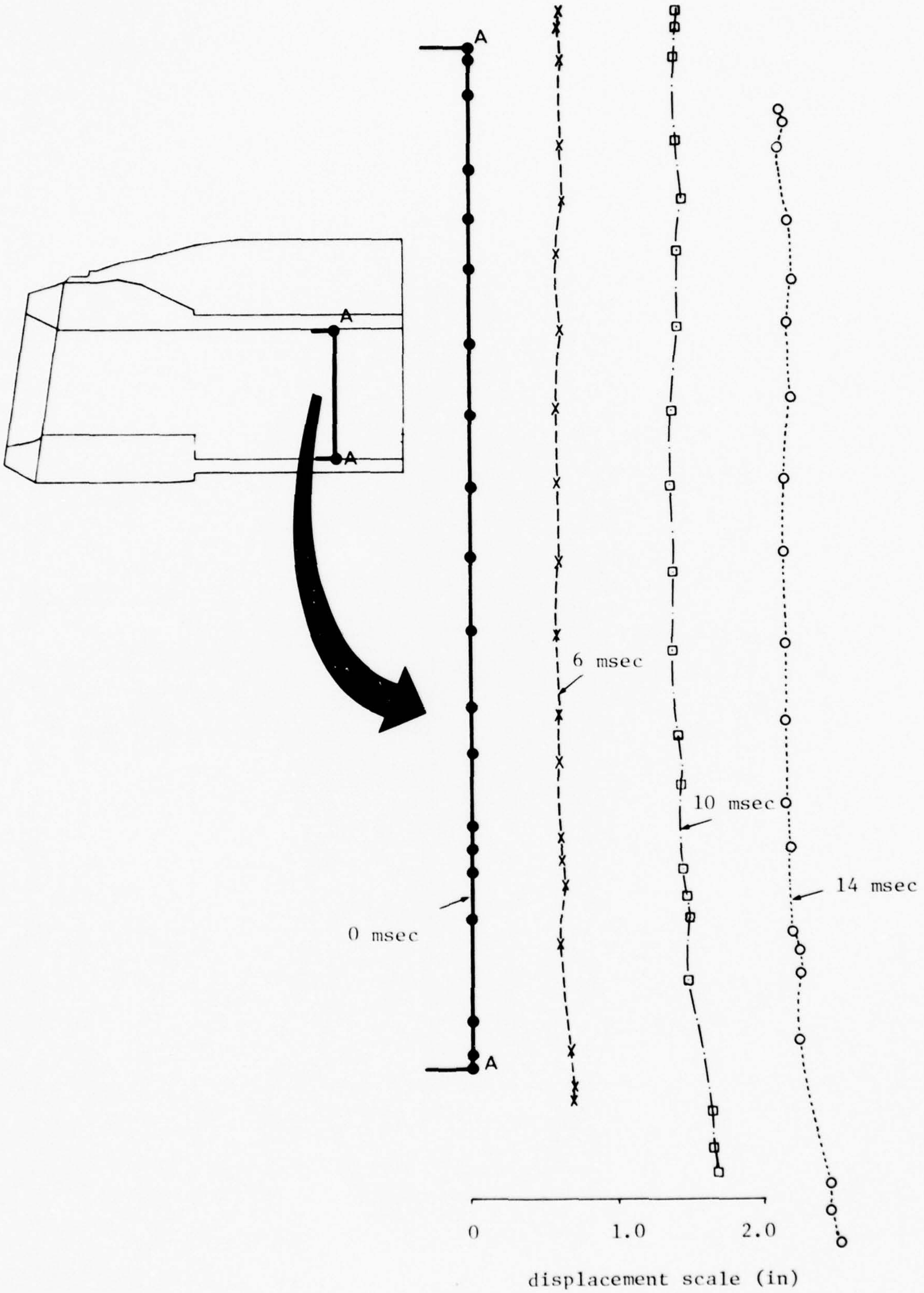

Figure 4-22. Displaced Profiles of Tube Section, One-Tube Diameter Behind Headworks.

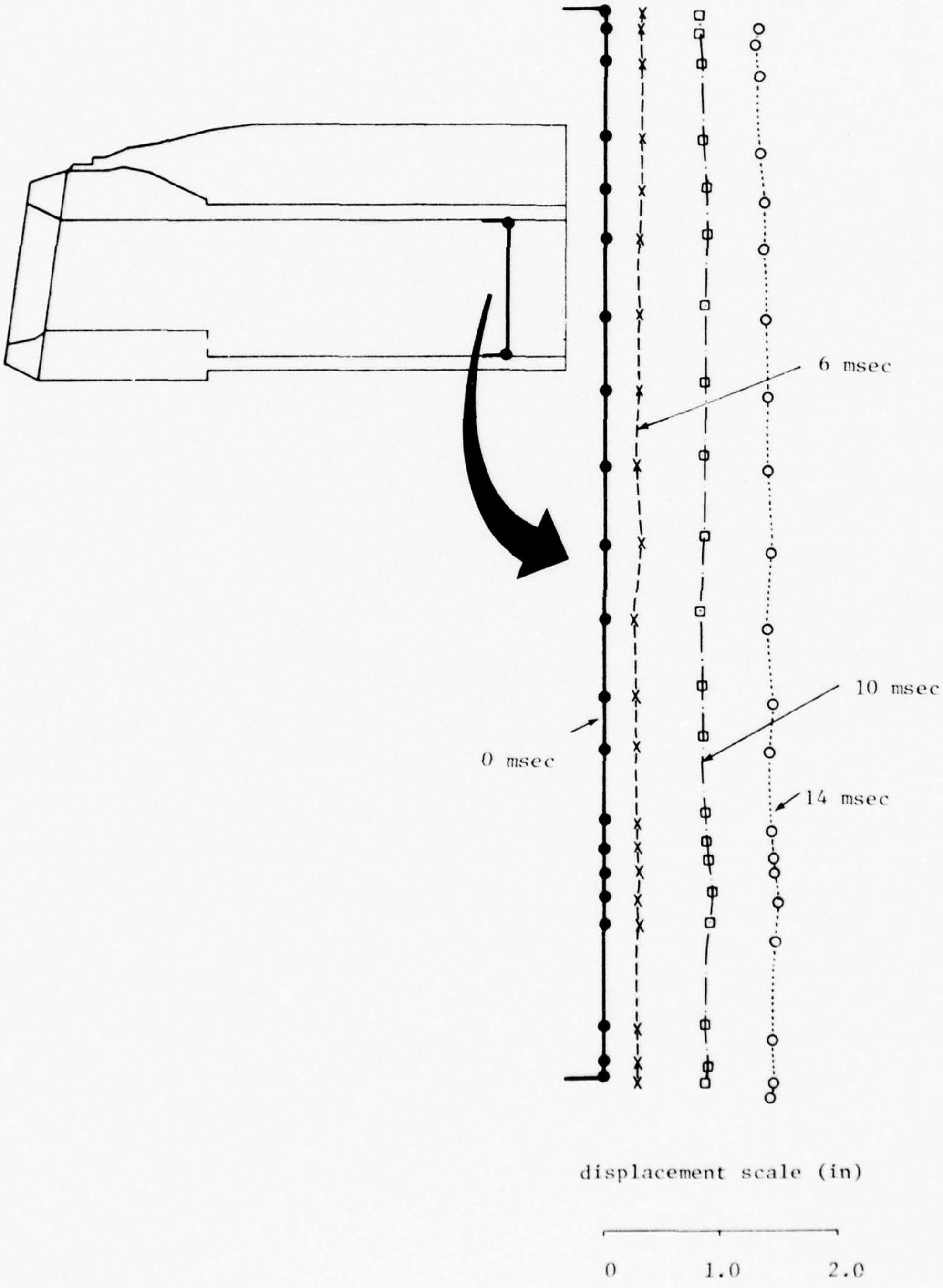

Figure 4-23. Displaced Profiles of Tube Section Two-Tube Diameters Behind Headworks.

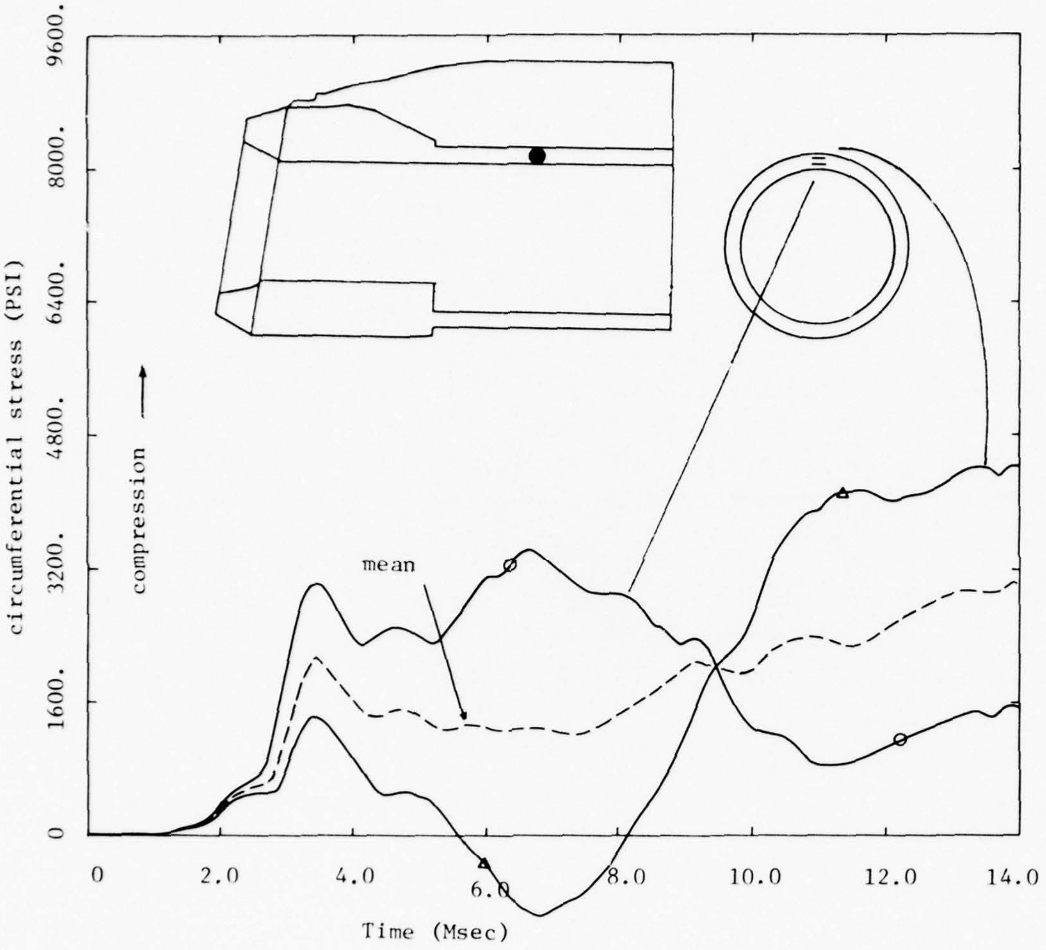

Figure 4-24a. Circumferential Stress/Time Histories for Points at Crown of Tube Section Half-Tube Diameter Behind Headworks.

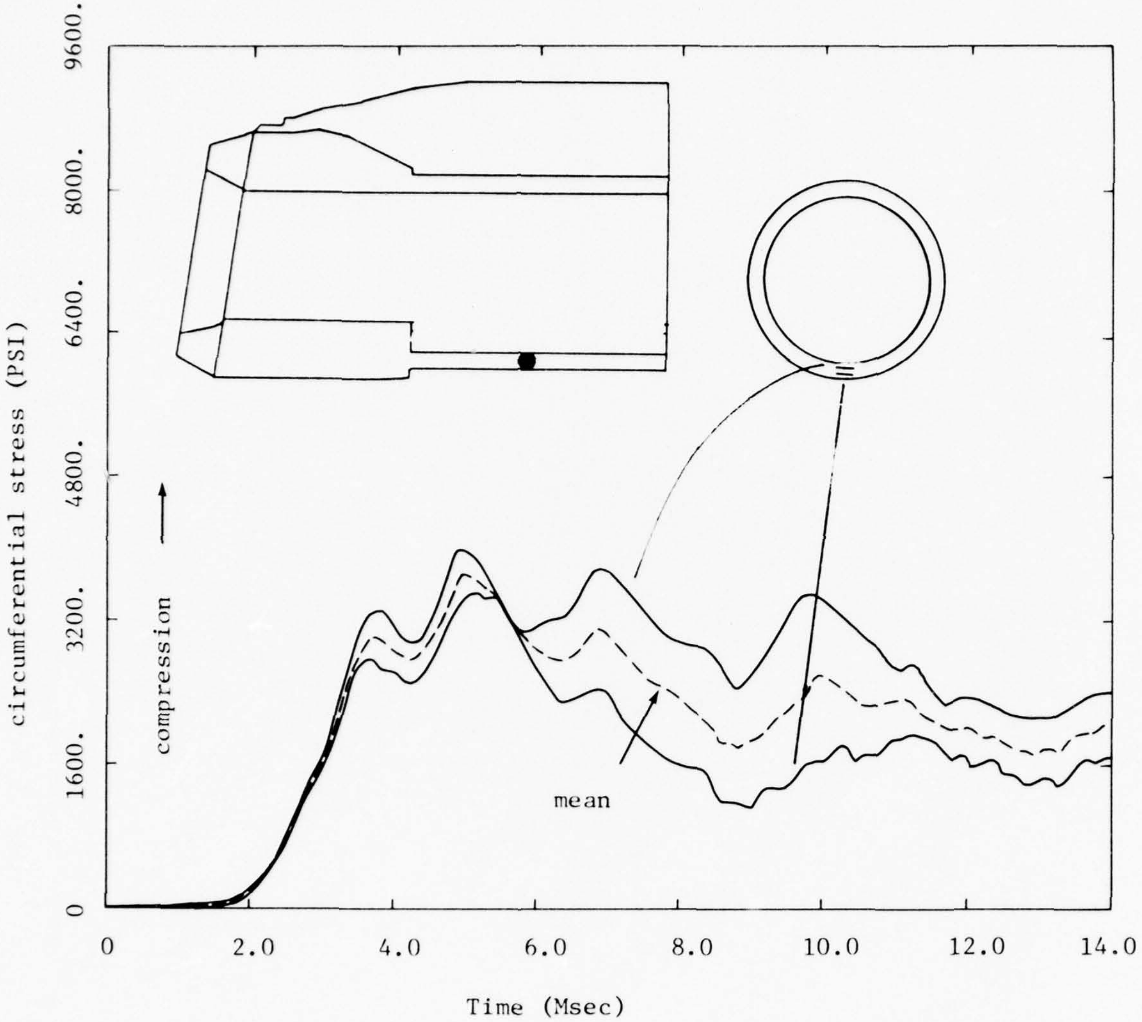

Figure 4-24b. Circumferential Stress/Time Histories for Points at Invert of Tube Section Half-Tube Diameter Behind Headworks.

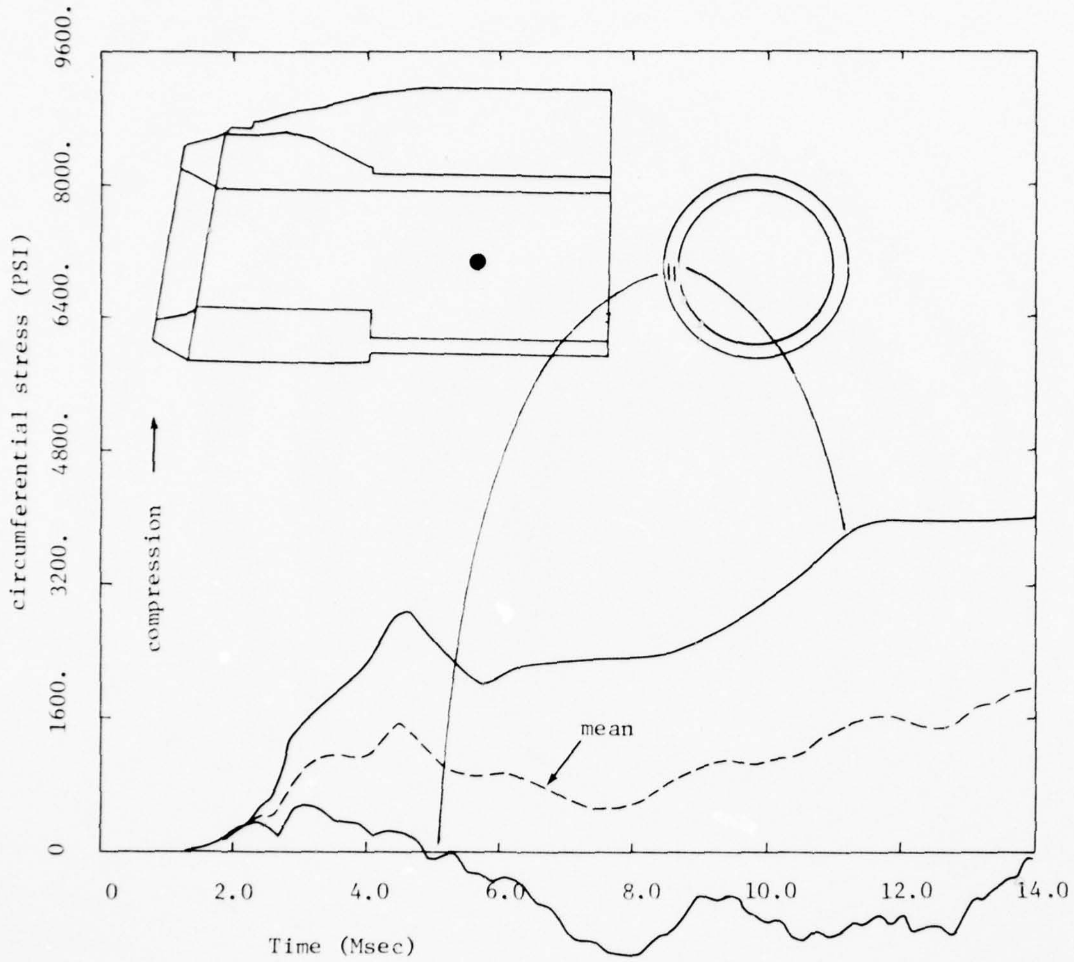

Figure 4-24c. Circumferential Stress/Time Histories for Points at Springline of Tube Section Half-Tube Diameter Behind Headworks.

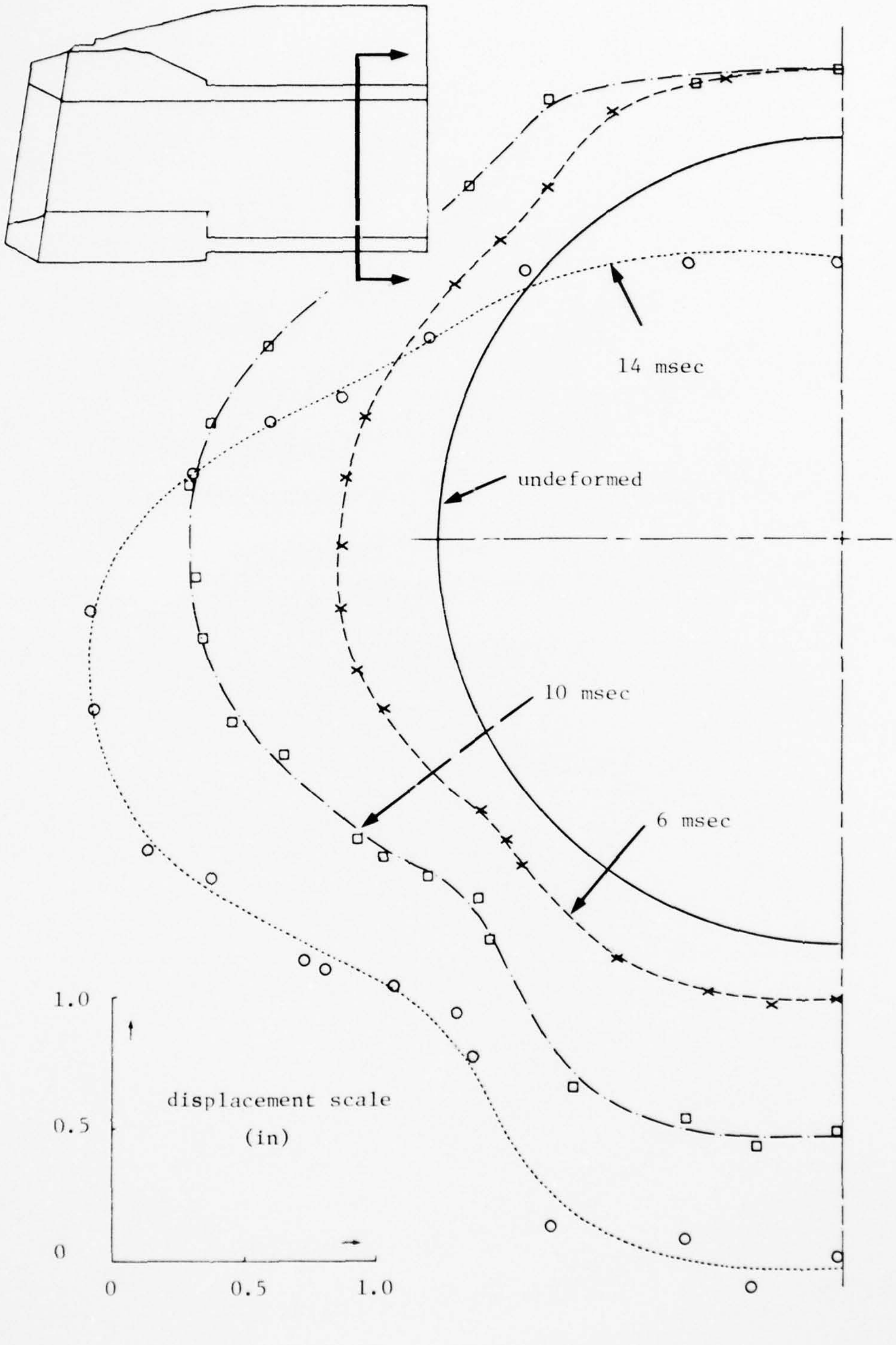

Figure 4-25. Deformed Shapes of Tube Cross-Section One-Tube Diameter Behind Headworks.

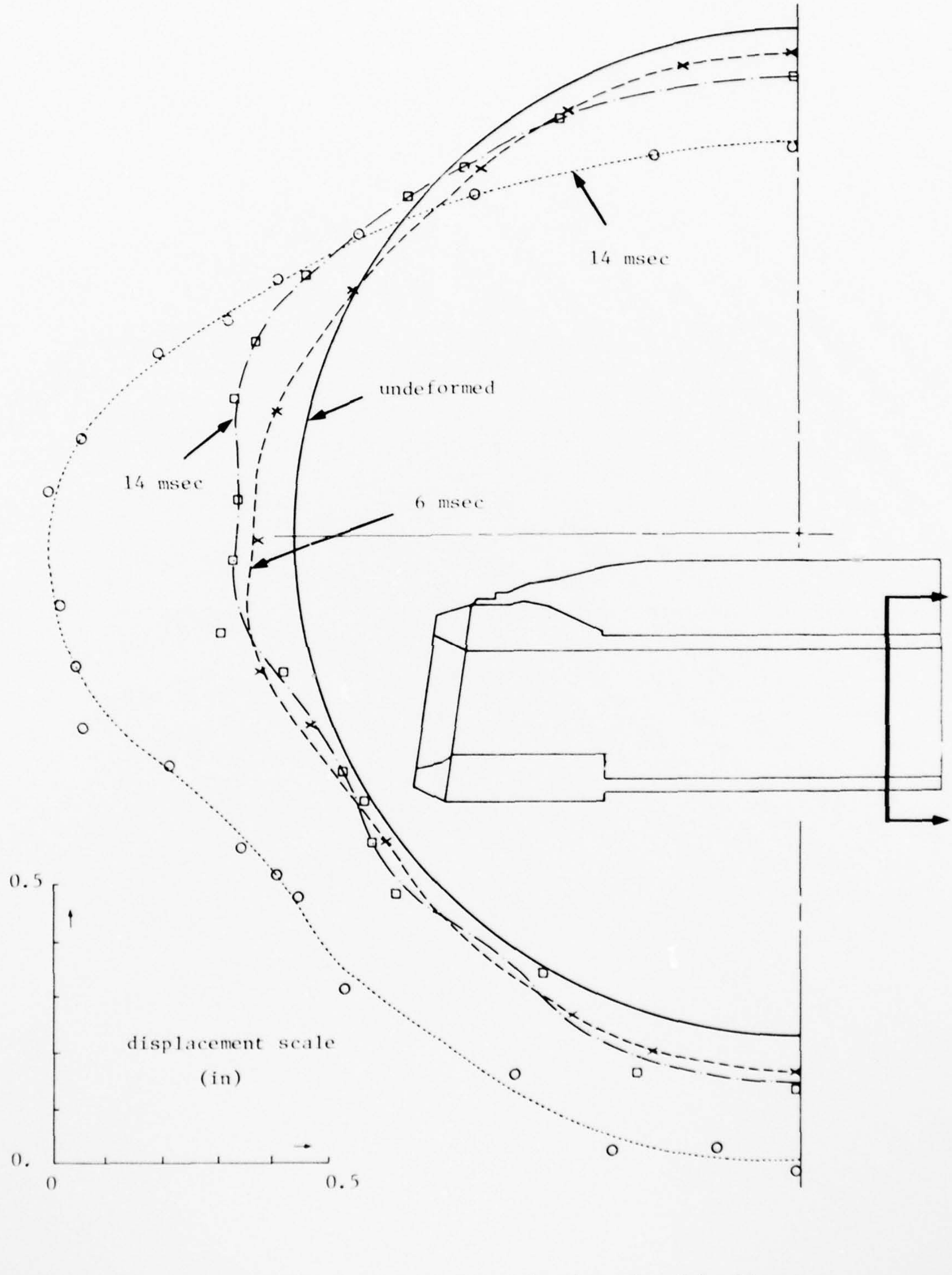

Figure 4-26. Deformed Shapes of Tube Cross-Section Two-Tube Diameters Behind Headworks.

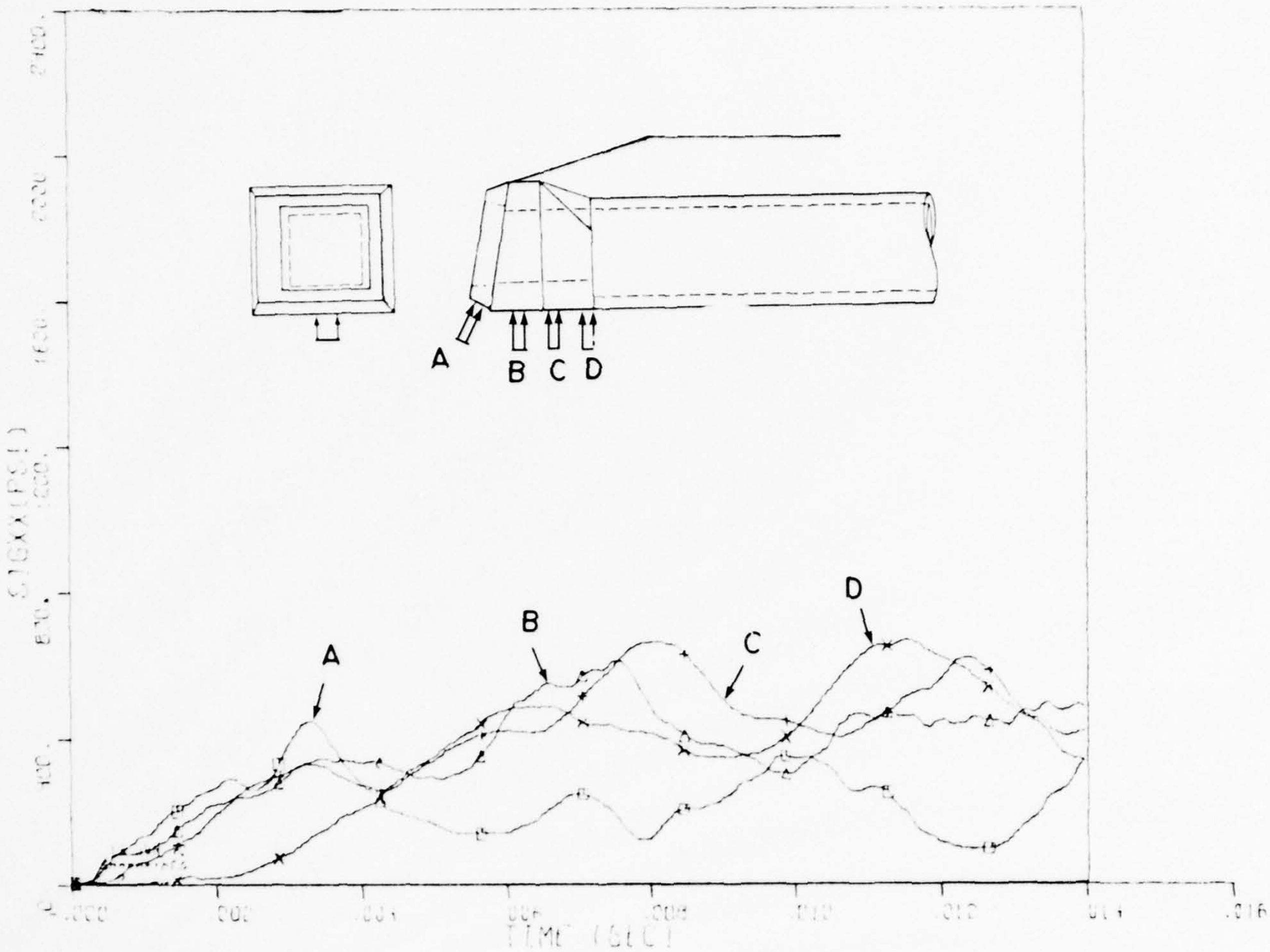

Figure 4-27. Soil/Structure Interface Stress at Points Along Bottom of Headworks.

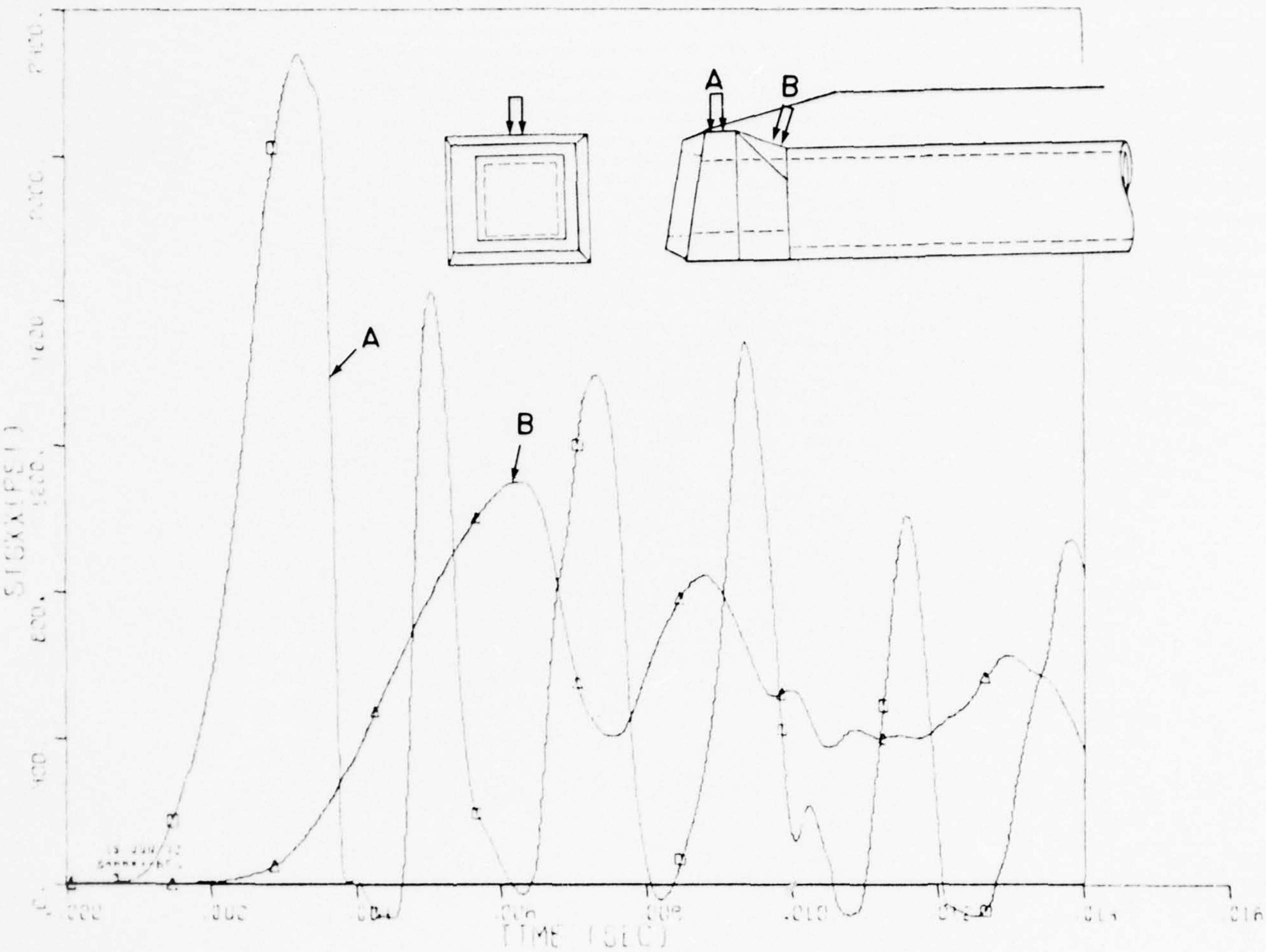

Figure 4-28. Soil/Structure Interface Stress at Points Along Top of Headworks.

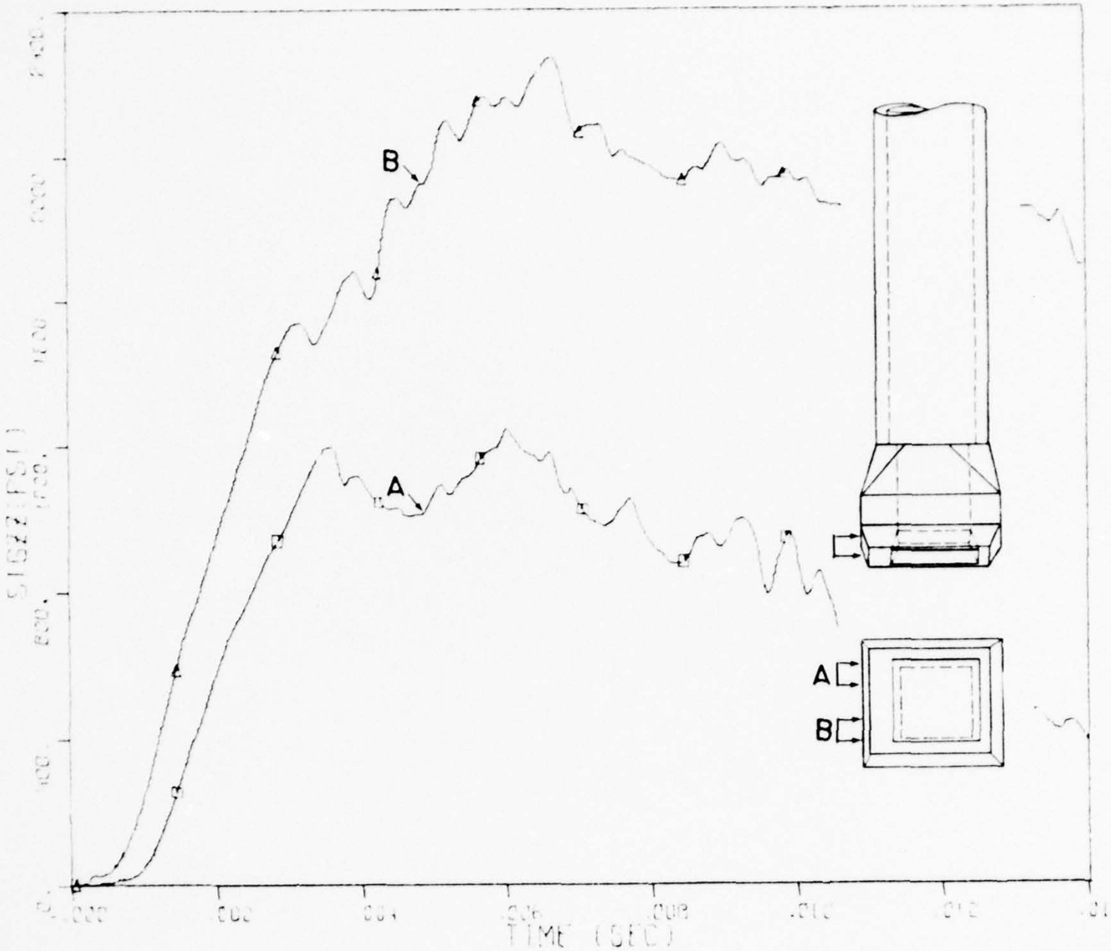

Figure 4-29a. Soil/Structure Interface Stress at Points Along Side of Headworks.

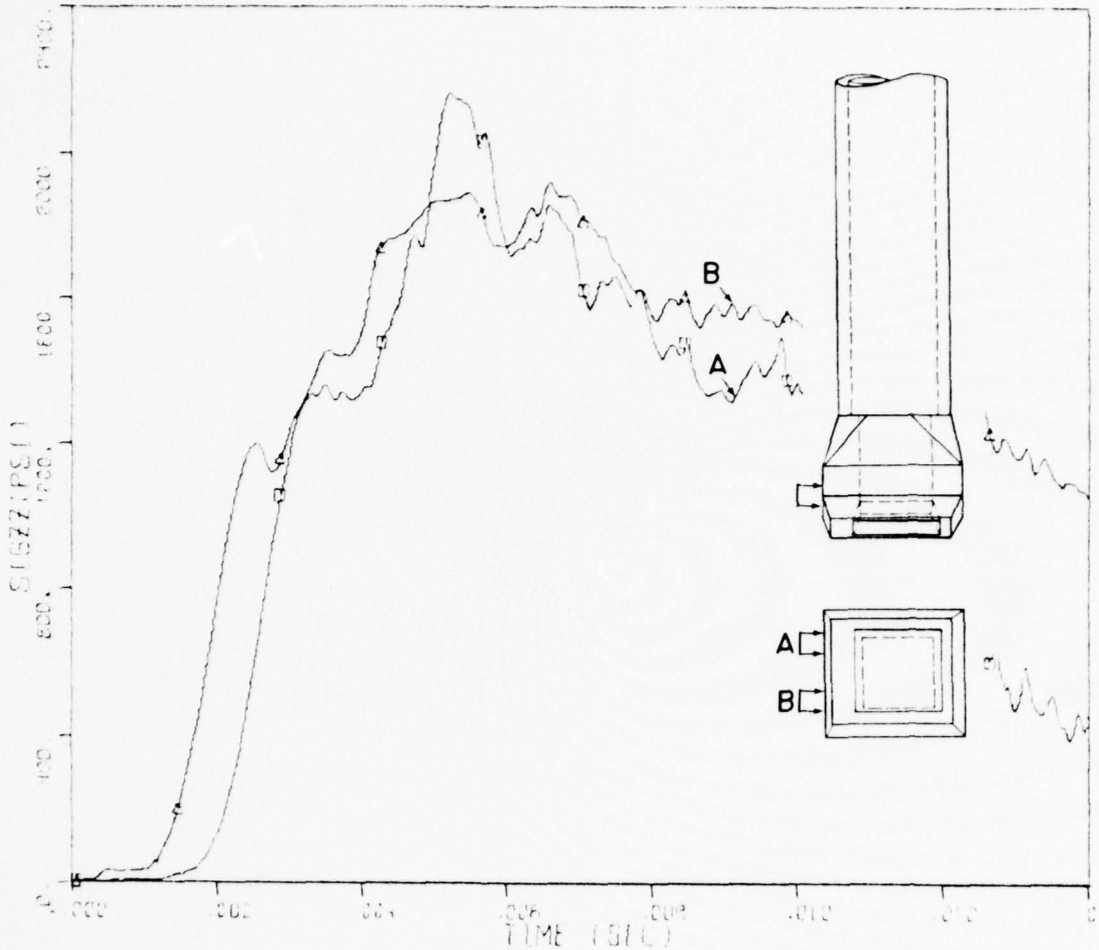

Figure 4-29b. Soil/Structure Interface Stress at Points Along Side of Headworks, Fore Portion.

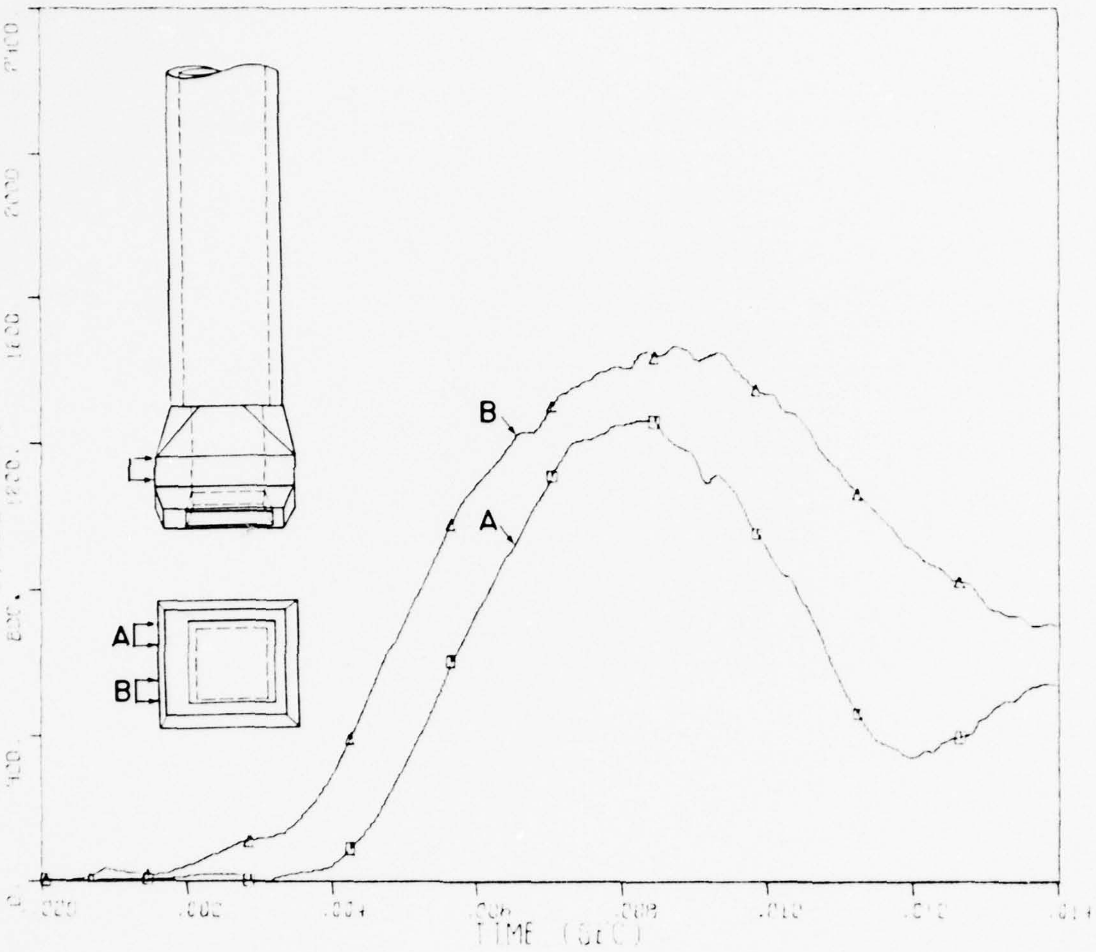

Figure 4-29c. Soil/Structure Interface Stress at Points Along Side of Headworks, Middle Portion.

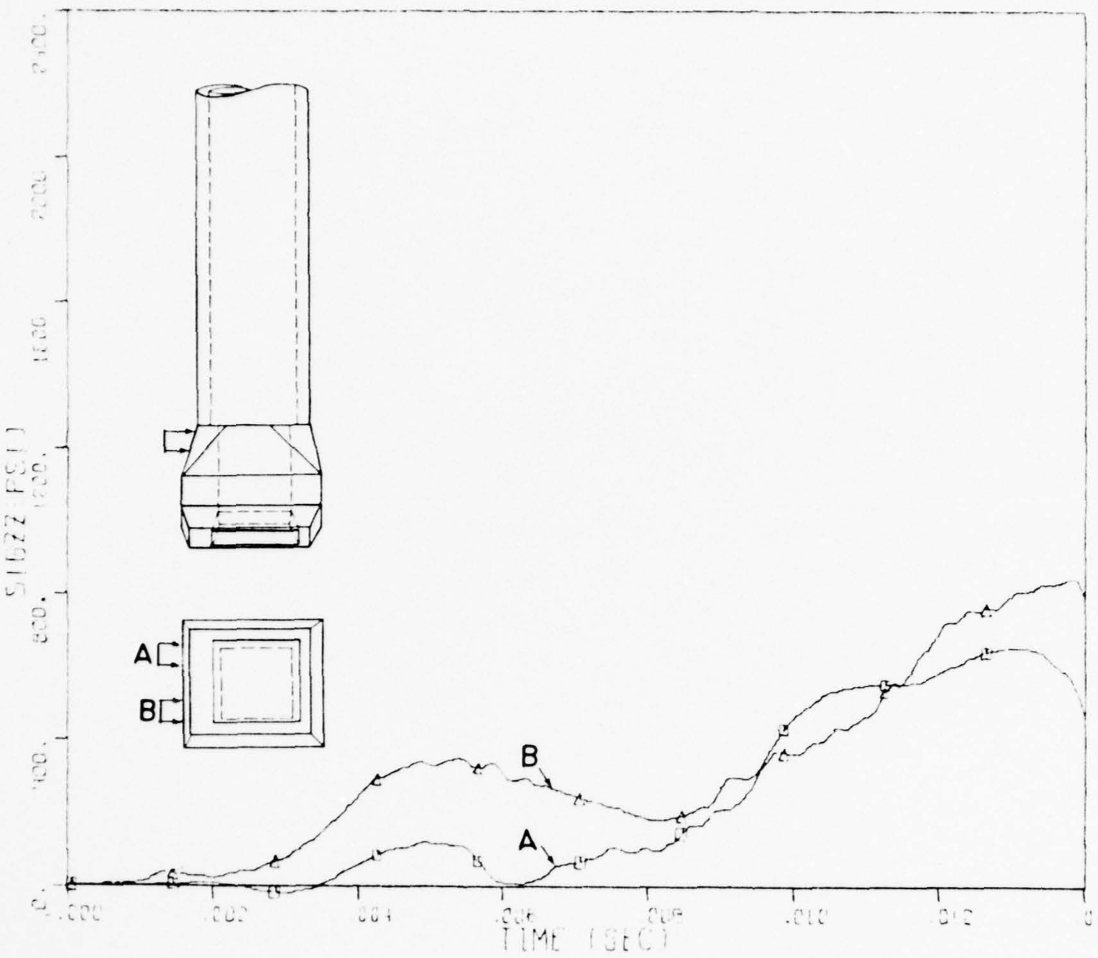

Figure 4-29d. Soil/Structure Interface Stress at Points Along Side of Headworks, Back Portion.

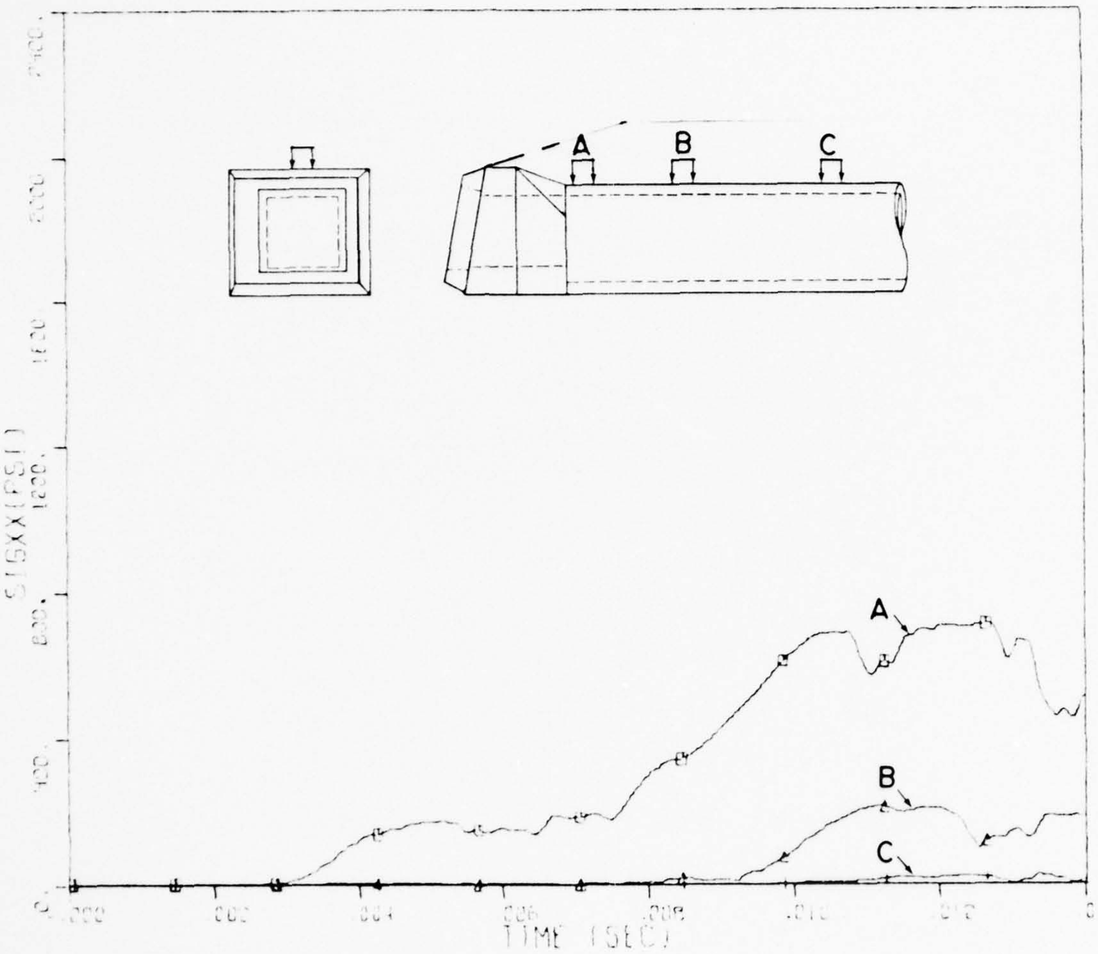

Figure 4-30. Soil/Structure Interface Stress at Points Along Top of Tube.

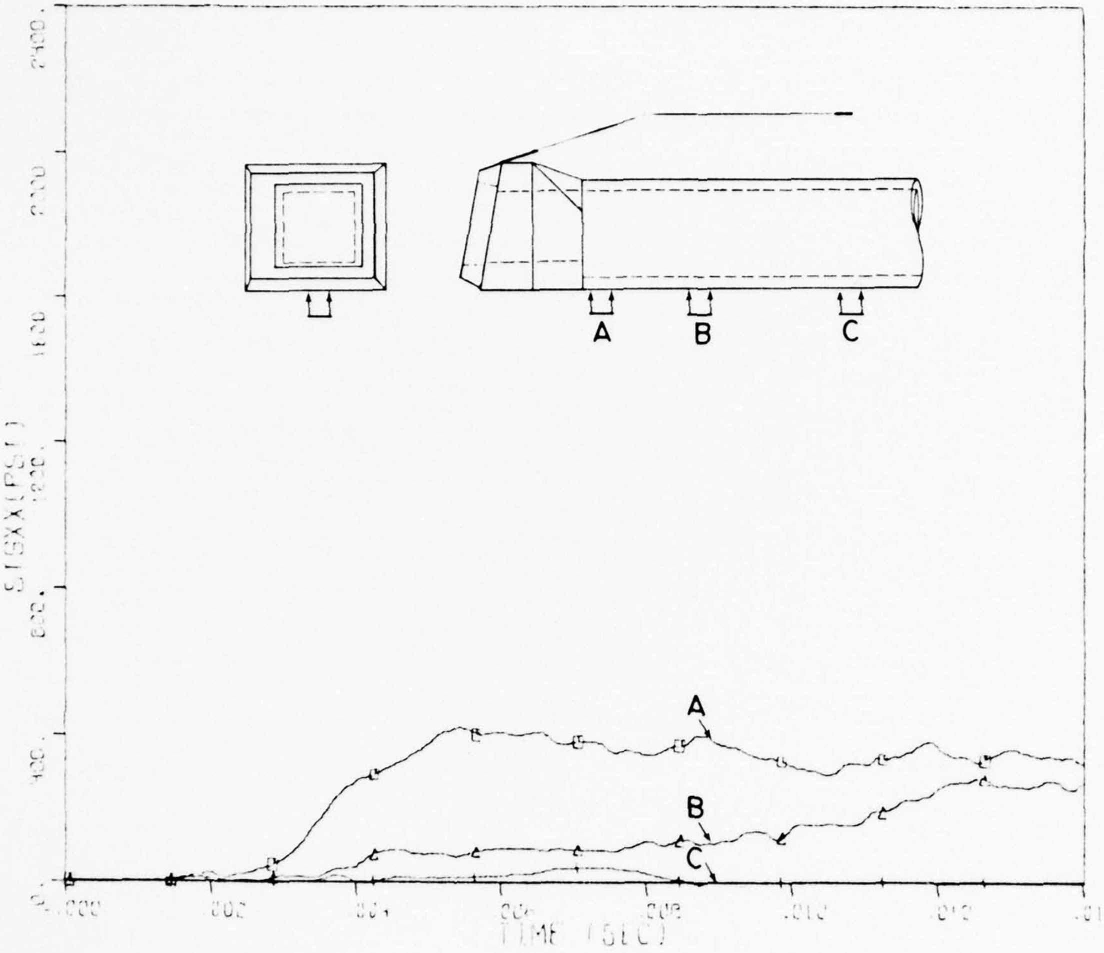

Figure 4-31. Soil/Structure Interface Stress at Points Along Bottom of Tube.

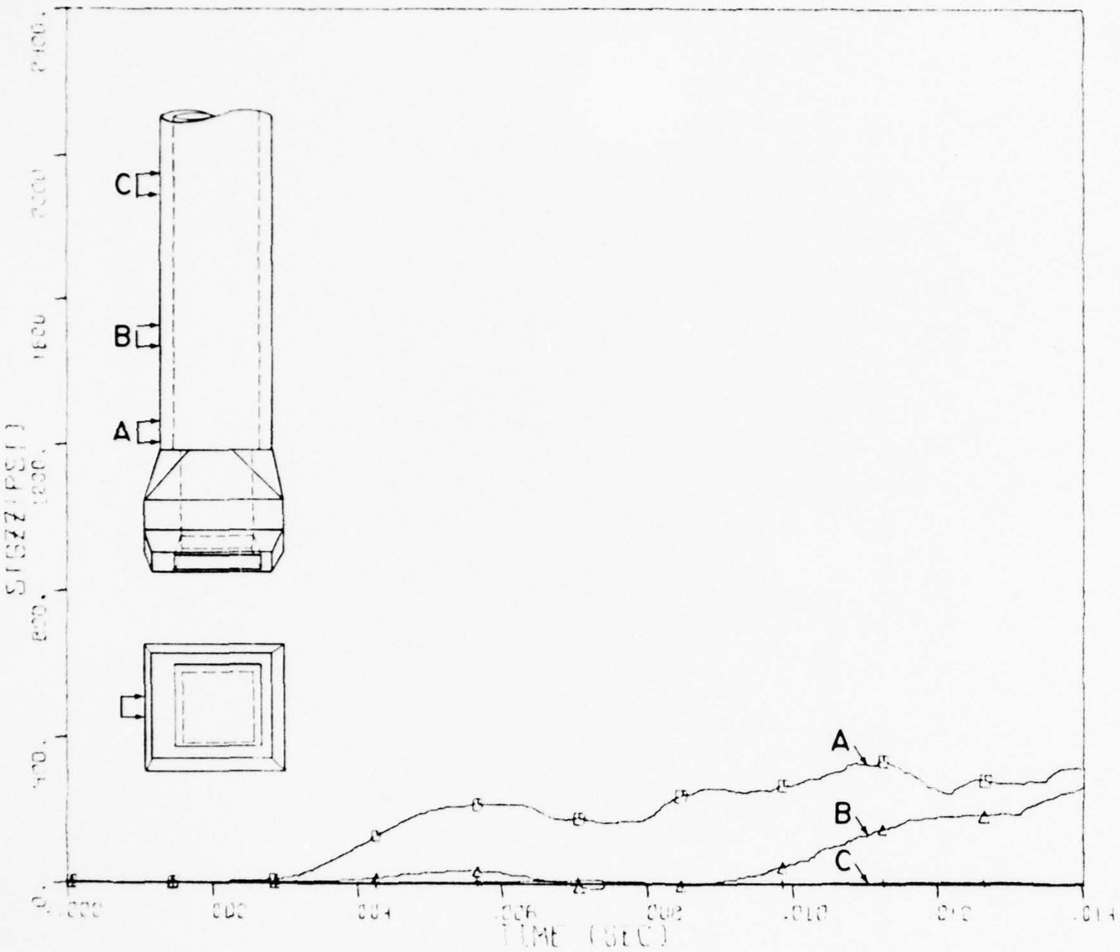

Figure 4-32. Soil/Structure Interface Stress at Points Along Side of Tube.

SECTION V

SUMMARY

The dominant deformation mode of the test structure is longitudinal compression, with some downward movement of the headworks at later times (after 8 msec). Despite high stresses, the bulk of the headworks and closure remains elastic; minor inelastic deformation occurs in the closure backplate and its adjacent concrete in the closure, the center gussets and inside corners of the frame, the bearing ring and the concrete immediately behind it.

Significant inelastic deformation occurs in the tube section; the deformation is more severe for portions of the tube closer behind the headworks. The tube section about one-half tube diameter behind the headworks sustains longitudinal stresses of the order of 10,000 psi and (plastic) strains of the order of 1.5%. The tube section about two tube diameters behind the headworks sustains longitudinal stresses of the order of 6,000 psi and strains of the order of 0.3%.

The S4 HEST load configuration does not provide ground shock loading on the top berm along the length of the tube. This constraint has two important impacts on the test structure response.

- Downward motion of the structure is most prominent at the headworks; the tube portion experiences very little downward motion and only as a reaction to that of the headworks. The downward headworks motion dominates the late time (after 10 msec), in-plane deformation pattern of the tube cross-sections, which is mainly the ovalling mode except in the vicinity of the invert where the stiff in situ soil in contact with the tube cross-section constrains it from following the ovalling pattern. The average downward tube displacement decreases rapidly with distance from the headworks. At 14 msec it is about an inch for a tube section one tube diameter behind the headworks, and about 0.3 inches for a section another tube diameter farther back.

- Portions of the tube farther than one diameter behind the headworks are effectively unconfined, i.e., the active earth pressure is null, and the tube concrete yields at an average longitudinal compression of 6,000 psi, its assumed unconfined strength.

The closure concrete model used in the simulation has a yield strength much higher than that used in Reference 1 (see Figure 3-6). This difference has two major effects.

- The closure in EVENT S4 responds basically as an elastic slab, with nominal mid-span deflections of an inch. This deformation mode is in contrast to the inelastic punching deformation observed in Reference 1 for a closure with low strength concrete. This change in the closure response is, in part, influenced by the lower HEST load simulated in the test (4,500 psi for S4 test versus 5,300 psi used in Reference 1), but the effect of the concrete properties appears to be more significant than that of the peak loading.

- By remaining elastic, the S4 closure is able to transmit most of the front load impulse to the headworks, thereby giving the latter a large momentum. This momentum, when combined with the lack of active earth pressure at the tube portion of the test structure, is responsible for the significant inelastic deformation observed in the tube.

The absence of the floor slab and fill inside the tube of the test structure results in an abrupt change in the load bearing cross-sectional area at the junction of the transition section and the tube, this change being more abrupt at the invert than elsewhere at the tube cross-section. Consequently, the longitudinal stress is amplified as it propagates from the transition section to the tube, more so at the invert than at the crown or springline. This creates a slight but distinct longitudinal bending moment which tends to torque the tube in a sense (convex) which is opposite to the case where the fill and slab are present. This torque, however, diminishes rapidly with distance along the tube and is negligible at a tube section two-tube diameters behind the headworks.

AD-A071 502 WEIDLINGER ASSOCIATES MENLO PARK CALIF F/G 19/4
PRETEST SIMULATION OF EVENT S4 HAVE HOST SERIES.(U)
JUL 78 F S WONG, J ISENBERG DNA001-77-C-0104
UNCLASSIFIED R-7841 DNA-4669T NL

2 OF 2
AD
A071502

END
DATE
FILMED
8-79
DDC

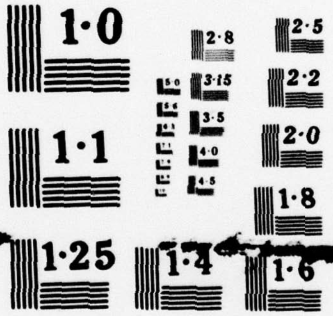
1·0
2·8
2·5
5·0
3·15
2·2
3·5
1·1
4·0
2·0
4·5
1·8
1·25
1·4
1·6

SECTION VI

REFERENCES

1. Wong, F. S., and Isenberg, J., "Dynamic Structural Analysis of MAP Shelters," DNA 4631Z, Weidlinger Associates, Contract No. DNA 001-C-77-0104, June 1978.

2. Malthan, J., "Calculated Data List," Agbabian Associates transmitted to Weidlinger Associates, April 2, 1978.

3. Drawings Code Ident. No. 81205, "MX Shelter, HSEM," Contract No. F04704-77-C-0005, The Boeing Company, September 29, 1977, Revised October 11, 1977.

4. McNickle, P. J., Miscellaneous Transmittals, AFWL to Weidlinger Associates, April 5, 1978.

5. Progress Report No. 3 to Defense Nuclear Agency, Contract No. DNA 001-77-C-0036, Weidlinger Associates, May 1977.

6. Shinn, J. D., "HAVE HOST Backfill Model," AFWL/DES-G Memo, March 4, 1977.

7. Rieben, T. R., "Structural Properties Recommended for HSEM Analysis," Boeing Aerospace Company Memo No. 2-1781-0000-172, March 28, 1978.

8. Endebrock, E. G., and Traina, L. A., "Static Concrete Constitutive Relations Based on Cubical Specimens, Vol. 1, Model Development and Verification," New Mexico State University, Technical Report No. AFWL-TR-72-59, Vol. 1, December 1972.

9. Baylor, J. L., Bienick, M. P., and Wright, J. P., "TRANAL: A 3-D Finite Element Code for Transient Nonlinear Analysis," DNA 3501F, Weidlinger Associates, June 30, 1974.

10. McNickle, P. J., "HAVE HOST S-1 Quick Look," AFWL/DE, May 26, 1977.

11. Wong, F. S., "S4 Pretest Simulation, Supplementary Data," DNA (TBD), Weidlinger Associates, Contract No. DNA 001-C-77-0104, IN PREPARATION.

DISTRIBUTION LIST

DEPARTMENT OF DEFENSE

Assistant to the Secretary of Defense
Atomic Energy
ATTN: Executive Assistant

Defense Advanced Rsch. Proj. Agency
ATTN: TIO
ATTN: NMRO

Defense Documentation Center
12 cy ATTN: DD

Defense Intelligence Agency
ATTN: RDS-3A

Defense Nuclear Agency
ATTN: SPAS
ATTN: SPSS
ATTN: DDST
4 cy ATTN: TITL

Field Command
Defense Nuclear Agency
ATTN: FCPRL

Joint Strat. Tgt. Planning Staff
ATTN: XPFS
ATTN: JLTW-2
ATTN: DOXT
ATTN: NRI-STINFO Library

Under Secy. of Def. for Rsch. & Engrg.
ATTN: Strategic & Space Systems (OS)

Field Command, Defense Nuclear Agency
ATTN: FCTMOF
ATTN: FCTMD
ATTN: FCPR

DEPARTMENT OF THE ARMY

Harry Diamond Laboratories
Department of the Army
ATTN: DELHD-N-P

U.S. Army Engr. Waterways Exper. Station
ATTN: Library

DEPARTMENT OF THE NAVY

Naval Surface Weapons Center
ATTN: Code F31

DEPARTMENT OF THE AIR FORCE

Aeronautical Systems Division, AFSC
ATTN: Technical Library

Air Force Institute of Technology
ATTN: Library

Air Force Systems Command
ATTN: R. Cross
ATTN: DLCAW
ATTN: Technical Library

DEPARTMENT OF THE AIR FORCE (Continued)

Air Force Weapons Laboratory, AFSC
ATTN: DED-A
ATTN: SUL
ATTN: DES-G
ATTN: NT
ATTN: DED-I
ATTN: DED-S
ATTN: DEO
ATTN: DEY

Armament Development & Test Center, AFSC
ATTN: Technical Library
ATTN: ADBRL-2

Deputy Chief of Staff
Research, Development & Acq.
Department of the Air Force
ATTN: AFRD
ATTN: AFRDQRM
ATTN: AFRDPM
ATTN: AFRDPS
ATTN: AFRDQPN

Deputy Chief of Staff
Logistics & Engineering
Department of the Air Force
ATTN: LEEE

Foreign Technology Division, AFSC
ATTN: NIIS Library
ATTN: TDPMG
ATTN: ETET
ATTN: TDFBD

Space & Missile Systems Organization
Air Force Systems Command
ATTN: DEB

Space & Missile Systems Organization
Air Force Systems Command
ATTN: DYS

Space & Missile Systems Organization
Air Force Systems Command
ATTN: MMH
ATTN: MNNH
ATTN: MNNM

Space & Missile Systems Organization
Air Force Systems Command
ATTN: RSS

Space & Missile Systems Organization
Air Force Systems Command
ATTN: XRTB

Strategic Air Command
Department of the Air Force
ATTN: XPFS
ATTN: NRI-STINFO Library

Assistant Chief of Staff, Intelligence
Department of the Air Force
ATTN: IN

DEPARTMENT OF DEFENSE CONTRACTORS

Civil Systems Inc.
ATTN: J. Bratton

General Electric Company-TEMPO
ATTN: DASIAC

University of Illinois
Consulting Services
ATTN: N. Newmark

Karagozian and Case
ATTN: J. Karagozian

Merritt CASES, Inc.
ATTN: J. Merritt

University of New Mexico
Electrical Engineering & Computer Science Dept.
ATTN: G. Lane

Physics International Co.
ATTN: F. Sauer

R & D Associates
ATTN: C. MacDonald
ATTN: J. Lewis

Rand Corp
ATTN: C. Mow

DEPARTMENT OF DEFENSE CONTRACTORS (Continued)

Science Applications, Inc.
ATTN: H. Wilson

Science Applications, Inc.
ATTN: J. Dishon

Science Applications, Inc.
ATTN: D. Maxwell

SRI International
ATTN: G. Abrahamson

Systems, Science & Software, Inc.
ATTN: D. Grine

Systems, Science & Software, Inc.
ATTN: C. Hastings

Tech Reps
ATTN: R. Holmes

TRW Defense & Space Sys. Group
2 cy ATTN: P. Dai

Weidlinger Assoc., Consulting Engineers
ATTN: J. Isenberg
ATTN: F. Wong

Boeing Co.
ATTN: R. Holmes